

INFLUENCE OF CONVERGENT RIBLET IN BLASIUS
BOUNDARY LAYER

THIRUKUMARAN NADESAN

NATIONAL UNIVERSITY OF SINGAPORE

2016

INFLUENCE OF CONVERGENT RIBLET IN BLASIUS
BOUNDARY LAYER

THIRUKUMARAN NADESAN

(M.Sc., NUS)

A THESIS SUBMITTED

FOR THE DEGREE OF DOCTOR OF PHILOSOPHY

DEPARTMENT OF MECHANICAL ENGINEERING

NATIONAL UNIVERSITY OF SINGAPORE

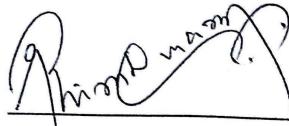
2016

DECLARATION

I hereby declare that the thesis is my original work and it has been written by me in its entirety.

I have duly acknowledged all the sources of information which have been used in the thesis.

This thesis has also not been submitted for any degree in any university previously.

A handwritten signature in black ink, appearing to read 'Thirukumaran Nadesan', written over a horizontal line.

Thirukumaran Nadesan

11 August 2016

Acknowledgements

First and foremost, I would like to thank my parents and sister whose moral support throughout the years gave an impetus to push myself to stay focused.

It gives me immense pleasure to thank Adjunct Professor Thong See Lee for inducting me into the PhD programme.

I would also like to express my sincere appreciation to my advisor, Assoc.Prof. Estruch-Samper, David. His guidance in the arena of experimental fluid dynamics had been indispensable. The instructions of Dr. Hatsari Mitsudharmadi and Dr. Tandiono had nuanced my way of conducting hot-wire experiments throughout the years. I am thankful to them too. I also wish to express my gratitude to Professor Tee Tai Lim for taking the time to discuss certain aspects of vortex dynamics. To all staff members and fellow research students, I am thankful for their valuable assistance, help and advice in carrying out my experimental work.

I dedicate this work to my wife, Mrs. Jaya Divya Thirukumaran, and I thank her for her unyielding support, care, and concern throughout the years. I would never have gone this far without her.

Finally, I would like to express my gratitude to National University of Singapore for the opportunity and the Research Scholarship to pursue the PhD programme in the Department of Mechanical Engineering.

Contents

Declaration	i
Acknowledgements	ii
Table of Contents	iii
Summary	vi
List of Tables	viii
List of Figures	ix
List of Symbols and Acronyms	xiv
1 Introduction	1
1.1 Background	1
1.2 Motivation	3
1.3 Objectives and Scope	5
1.4 Organization of Thesis	5
2 Literature review	6
2.1 Transient growth: Origin and Evolution of the theory	6
2.2 Streak instability	9
3 Experimental Details	12
3.1 Experimental Set-up	12

3.2	Instrumentation	15
3.2.1	Hot Wire Anemometer and Sensors	16
3.2.2	Data Acquisition System	18
3.3	Experimental Procedures	18
3.3.1	Calibrations	18
3.3.1.1	SN-probe calibration	18
3.3.2	Measurement of Mean and Fluctuating Streamwise Velocities	19
3.3.3	Determination of wall position	20
3.4	Uncertainty analysis	21
4	Influence of an Isolated Convergent Riblet	23
4.1	Introduction	23
4.2	Flow kinematics	24
4.2.1	Initial Disturbances	29
4.2.2	Evolution of Disturbances	33
4.2.3	Streak Characteristics	38
4.3	Concluding remarks	52
5	Instability of forced wavelength disturbances	53
5.1	Introduction	53
5.2	Mean Velocity	54
5.3	Shear stress	65
5.4	Fluctuating Velocity	77
5.5	Vortex Growth Rate	83
5.6	Spectral characteristics	84
5.7	Concluding remarks	84
6	Conclusions and Recommendations	87
6.1	Conclusions	87
6.1.1	Isolated Riblet	87
6.1.2	Forced wavelength disturbances	89

CONTENTS

6.2 Recommendations	90
Bibliography	93

Summary

The link between roughness-induced disturbances and hydrodynamic instability theories was unlooked-for till the advent of transient growth. Within the context of transient growth, roughness induced three dimensional disturbances that manifests as streamwise vortices might either undergo a brief growth followed by viscous decay or experience an exponential growth leading to secondary instability. Either of the mentioned scenario is dependent upon the characteristics of the initial disturbance which in turn is dependent upon the roughness geometry.

The main objective of the present work is to experimentally investigate the transient growth characteristics of the boundary layer that is under the influence of a directionally dependent roughness element, namely, convergent riblet. Smoke-wire flow visualization and hot-wire anemometer experiments were carried out to obtain qualitative and quantitative data respectively. First sets of experiments were carried out by employing isolated riblet roughness. Second set of experiments were conducted by arranging the riblets of particular height in-line to force the disturbance wavelength. Velocity measurements were carried out by means of hot-wire anemometry (single probe) which formed the bulk of the study. The growth characteristics of the vortices were studied for 6 different roughness Reynolds number in the case of isolated convergent riblet, while in the case of forced wavelength disturbances, the effect of vortex interactions on instability that effects from a particular roughness Reynolds number was studied.

Results reveal that with the increasing height of the riblet, three different phenomena - transient growth, low speed streak instability and vortex breakdown due to viscous diffusion - was observed in the case of isolated riblet. The instability observed in this case comprised three stages: the development and decay of varicose mode, transition to sinuous mode and growth of sinuous modes. The spectral characteristics showed that the energy that rested in the high frequency spec-

trum in the varicose mode shifted to the low frequency spectrum along the downstream where the sinuous mode dominated. The instability characteristics was found to be different from those that would occur in the presence of hairpin vortices.

In the case of forced wavelength disturbances, the closer proximity of the wavelength paved the way for vortex breakdown via interaction. With the increased spacing of the riblet, the spectral characteristics of the instability modes were found to be similar to that of the isolated riblet case. This contrasts the well known wavelength-dependent instability modes - fundamental and subharmonic sinuous and fundamental and sub-harmonic varicose modes - that arises from the dynamics of hairpin vortices.

List of Tables

4.1	Test cases; δ_k - Blasius boundary layer thickness at the leading edge of riblet (at $x=320$ mm), u_k - Mean velocity at height k of the riblet.	24
4.2	Effect of Roughness Reynolds number. Frequencies measured at station $x=200$ mm in the upwash region of the main vortices at $y/\delta_k=0.25$	48
4.3	Comparison of roughness induced disturbances and its instability.	51

List of Figures

1.1	Transition road map as laid down by Morkovin et al. (1994).	3
3.1	Schematic of smoke-wire flow visualization Set-up.	13
3.2	Schematic of the wind tunnel Set-up for hot-wire measurement.	14
3.3	Blasius boundary layer at several streamwise stations.	15
3.4	Shape factor, H, showcasing Zero pressure gradient boundary layer development. H=2.59 corresponds to Blasius solution.	16
3.5	An isolated convergent riblet.	16
3.6	Block diagram of hot-wire anemometer system.	17
3.7	King’s law curve fit showing uncertainty; — Curve fit, - - - Uncertainty	22
4.1	End on view of the cross-plane visualization of case $k/\delta_k=0.24$. The flow is out of page. Origin at the trailing vertex of the riblet.	25
4.2	End on view of the cross-plane visualization of case $k/\delta_k=0.48$ ($k=3$ mm). The flow is out of page. Origin at the trailing vertex of the riblet.	26
4.3	Schematic of the conjecture of flow kinematics.	27
4.4	Left: Flow kinematics of hemispherical protuberance from Acarlar and Smith (1987). Right: Flow kinematics of cylindrical protuberance from Pattenden et al. (2005)	27
4.5	Characteristics of initial disturbance; a) $k/\delta_k=0.16$, b) $k/\delta_k=0.24$, c) $k/\delta_k=0.48$. Solid lines -Isolines of turbulence intensity; Dashed lines - Isolines of streamwise component of velocity (u/U_∞).	29

4.6	Normal distribution of amplitude of spanwise harmonic modes: a) $k/\delta_k=0.16$, b) $k/\delta_k=0.24$, c) $k/\delta_k=0.48$	31
4.7	Normal distribution of disturbance amplitude. \square - $k/\delta_k=0.16$, Δ - $k/\delta_k=0.24$, \circ - $k/\delta_k=0.48$	32
4.8	Wall-normal distribution of the mean velocity of low speed streak (upwash): - - - Blasius solution, \circ - $k/\delta_k=0.16$, \square - $k/\delta_k=0.24$, Δ - $k/\delta_k=0.48$	33
4.9	Total Disturbance profiles; a) $k/\delta_k=0.16$, b) and C) $k/\delta_k=0.24$, d) and e) $k/\delta_k=0.48$.	34
4.10	Spanwise wavelength power spectral density; a) $k/\delta_k=0.16$: - $x=10$ mm, - - $x=15$ mm, -.- $x=30$ mm, -.- $x=500$ mm; b) $k/\delta_k=0.24$: - $x=10$ mm, - - $x=100$ mm, -.- $x=300$ mm, -.- $x=500$ mm, c) $k/\delta_k=0.48$: - $x=10$ mm, - - $x=90$ mm, -.- $x=180$ mm, -.- $x=240$ mm. Note the variation of the ordinate.	35
4.11	Iso-surface of $\partial u/\partial z$ (Red: $0.1 \times 10^{-3} s^{-1}$, Blue: $-0.1 \times 10^{-3} s^{-1}$; a) $k/\delta_k=0.16$, b) $k/\delta_k=0.24$ and c) $k/\delta_k=0.48$. Iso-surface volume was formed by interpolation of the data measured at 11 stations for $k/\delta_k=0.16$ and 0.48 , 67 stations for $k/\delta_k=0.24$.	36
4.12	Evolution of maximum streak amplitude; \circ - $k/\delta_k=0.16$, \square - $k/\delta_k=0.24$, Δ - $k/\delta_k=0.48$.	38
4.13	Iso- u/U_∞ contour at different cross-stream stations for $k/\delta_k=0.16$; a) $x=10$ mm, b) $x=15$ mm, c) $x=30$ mm, d) $x=100$ mm, e) $x=200$ mm, f) $x=300$ mm, g) $x=400$ mm, h) $x=500$ mm.	39
4.14	Iso- u/U_∞ contours at different cross stations for $k/\delta_k=0.16$; a) $x=10$ mm, b) $x=50$ mm, c) $x=100$ mm, d) $x=150$ mm, e) $x=200$ mm, f) $x=300$ mm, g) $x=400$ mm, h) $x=500$ mm.	41
4.15	Iso- u/U_∞ contour for $k/\delta_k=0.24$ at a) $y/\delta_k=0.25$, b) $y/\delta_k=0.5$, c) $y/\delta_k=0.75$, d) $y/\delta_k=1$. Contours were formed by interpolation of measured data at 67 stations. .	42
4.16	Evolution of Turbulence intensity concentrations for $k/\delta_k=0.24$; a) $x=10$ mm, b) $x=15$ mm, c) $x=20$ mm, d) $x=25$ mm, e) $x=30$ mm, f) $x=35$ mm, g) $x=40$ mm, h) $x=45$ mm, i) $x=50$ mm, j) $x=55$ mm, k) $x=60$ mm, l) $x=65$ mm, m) $x=70$ mm, n) $x=75$ mm, o) $x=100$ mm, p) $x=125$ mm, q) $x=150$ mm, r) $x=175$ mm, s) $x=200$ mm, t) $x=250$ mm, u) $x=300$ mm, v) $x=350$ mm, w) $x=400$ mm, x) $x=450$ mm, y) $x=500$ mm.	45

4.17	The isolines of a) $\partial u/\partial y$ at $x=50$ mm and b) $\partial u/\partial z$ at $x=200$ mm.	45
4.18	Growth of varicose and sinuous modes in terms of maximum turbulence intensity.	46
4.19	Power spectra of streamwise fluctuating velocity component at different stream-wise stations.	46
4.20	Non-dimensionalised premultiplied one-dimensional spectra obtained at the position of maximum Tu. Arrows indicate the peak.	47
4.21	Iso- u/U_∞ contours for $k/\delta_k=0.48$; a) $x=10$ mm, b) $x=30$ mm, c) $x=50$ mm, d) $x=100$ mm, e) $x=150$ mm, f) $x=200$ mm, g) $x=250$ mm.	49
4.22	Iso- u/U_∞ contour for $k/\delta_k=0.48$ at $y/\delta_k=0.25$. Contour formed by interpolation of measured data at 11 stations.	50
4.23	Evolution of Tu concentrations of the secondary streaks for $k/\delta_k=0.48$; a) $x=100$ mm, b) $x=150$ mm, c) $x=200$ mm, d) $x=250$ mm.	50
5.1	Iso- u/U_∞ contour at different cross-stream stations for $\lambda=10$ mm; a) $x=5$ mm, b) $x=10$ mm, c) $x=15$ mm, d) $x=20$ mm, e) $x=50$ mm, f) $x=75$ mm, g) $x=100$ mm h) $x=150$ mm, i) $x=200$ mm, j) $x=250$ mm, k) $x=300$ mm, l) $x=350$ mm, m) $x=400$ mm, n) $x=450$ mm, o) $x=500$ mm.	56
5.2	Iso- u/U_∞ contour at different cross-stream stations for $\lambda=12.5$ mm; a) $x=5$ mm, b) $x=10$ mm, c) $x=15$ mm, d) $x=25$ mm, e) $x=50$ mm, f) $x=75$ mm, g) $x=100$ mm, h) $x=150$ mm i) $x=200$ mm, j) $x=250$ mm, k) $x=300$ mm, l) $x=350$ mm, m) $x=400$ mm, n) $x=450$ mm, o) $x=500$ mm, p) $x=550$ mm.	58
5.3	Iso- u/U_∞ contour at different cross-stream stations for $\lambda=15$ mm; a) $x=5$ mm, b) $x=10$ mm, c) $x=15$ mm, d) $x=25$ mm, e) $x=50$ mm, f) $x=75$ mm, g) $x=100$ mm h) $x=150$ mm, i) $x=200$ mm, j) $x=250$ mm, k) $x=300$ mm, l) $x=350$ mm, m) $x=400$ mm, n) $x=450$ mm, o) $x=500$ mm, p) $x=550$ mm.	60
5.4	Iso- u/U_∞ contours at $x - z$ plane for $\lambda=10$ mm; a) $y/\delta_k=0.25$, b) $y/\delta_k=0.5$, c) $y/\delta_k=0.75$, d) $y/\delta_k=1$	61
5.5	Iso- u/U_∞ contour at $x - z$ plane for $\lambda=12.5$ mm; a) $y/\delta_k=0.25$, b) $y/\delta_k=0.5$, c) $y/\delta_k=0.75$, d) $y/\delta_k=1$	62

5.6 Iso- u/U_∞ contour at $x - z$ plane for $\lambda=15$ mm; a) $y/\delta_k=0.25$, b) $y/\delta_k=0.5$, c) $y/\delta_k=0.75$, d) $y/\delta_k=1$ 63

5.7 Downstream development of upwash streamwise velocity profiles across the boundary layer for a) and b) $\lambda=10$ mm, c) and d) $\lambda=12.5$ mm, e) and f) $\lambda=15$ mm. . . . 64

5.8 Iso-shear($\partial u/\partial y$) contour at different cross-stream stations for $\lambda=10$ mm; a) $x=5$ mm, b) $x=10$ mm, c) $x=15$ mm, d) $x=25$ mm, e) $x=50$ mm, f) $x=100$ mm g) $x=150$ mm, h) $x=200$ mm, i) $x=250$ mm, j) $x=300$ mm, k) $x=350$ mm, l) $x=400$ mm, m) $x=450$ mm, n) $x=500$ mm, o) $x=550$ mm, p) $x=600$ mm. 66

5.9 Iso-shear($\partial u/\partial y$) contour at different cross-stream stations for $\lambda=12.5$ mm; a) $x=5$ mm, b) $x=10$ mm, c) $x=15$ mm, d) $x=25$ mm, e) $x=50$ mm, f) $x=75$ mm, g) $x=100$ mm h) $x=150$ mm, i) $x=200$ mm, j) $x=250$ mm, k) $x=300$ mm, l) $x=350$ mm, m) $x=400$ mm, n) $x=450$ mm, o) $x=500$ mm, p) $x=550$ mm. 68

5.10 Iso-shear($\partial u/\partial y$) contour at different cross-stream stations for $\lambda=15$ mm; a) $x=5$ mm, b) $x=10$ mm, c) $x=15$ mm, d) $x=25$ mm, e) $x=50$ mm, f) $x=75$ mm, g) $x=100$ mm h) $x=150$ mm, i) $x=200$ mm, j) $x=250$ mm, k) $x=300$ mm, l) $x=350$ mm, m) $x=400$ mm, n) $x=450$ mm, o) $x=500$ mm, p) $x=550$ mm. 70

5.11 Iso-shear($\partial u/\partial z$) contour at different cross-stream stations for $\lambda=10$ mm; a) $x=5$ mm, b) $x=10$ mm, c) $x=15$ mm, d) $x=25$ mm, e) $x=50$ mm, f) $x=75$ mm, g) $x=100$ mm h) $x=150$ mm, i) $x=200$ mm, j) $x=250$ mm, k) $x=300$ mm, l) $x=350$ mm, m) $x=400$ mm, n) $x=450$ mm, o) $x=500$ mm, p) $x=550$ mm. 72

5.12 Iso-shear($\partial u/\partial z$) contour at different cross-stream stations for $\lambda=12.5$ mm; a) $x=5$ mm, b) $x=10$ mm, c) $x=15$ mm, d) $x=25$ mm, e) $x=50$ mm, f) $x=75$ mm, g) $x=100$ mm h) $x=150$ mm, i) $x=200$ mm, j) $x=250$ mm, k) $x=300$ mm, l) $x=350$ mm, m) $x=400$ mm, n) $x=450$ mm, o) $x=500$ mm, p) $x=550$ mm. 74

5.13 Iso-shear($\partial u/\partial z$) contour at different cross-stream stations for $\lambda=15$ mm; a) $x=5$ mm, b) $x=10$ mm, c) $x=15$ mm, d) $x=25$ mm, e) $x=50$ mm, f) $x=75$ mm, g) $x=100$ mm h) $x=150$ mm, i) $x=200$ mm, j) $x=250$ mm, k) $x=300$ mm, l) $x=350$ mm, m) $x=400$ mm, n) $x=450$ mm, o) $x=500$ mm, p) $x=550$ mm. 76

5.14 Iso-Tu contour at different cross-stream stations for $\lambda=10$ mm; a) $x=5$ mm, b) $x=10$ mm, c) $x=15$ mm, d) $x=25$ mm, e) $x=50$ mm, f) $x=75$ mm, g) $x=100$ mm h) $x=150$ mm, i) $x=200$ mm, j) $x=250$ mm, k) $x=300$ mm, l) $x=350$ mm, m) $x=400$ mm, n) $x=450$ mm, o) $x=500$ mm, p) $x=550$ mm.	78
5.15 Iso-Tu contour at different cross-stream stations for $\lambda=12.5$ mm; a) $x=5$ mm, b) $x=10$ mm, c) $x=15$ mm, d) $x=25$ mm, e) $x=50$ mm, f) $x=75$ mm, g) $x=100$ mm h) $x=150$ mm, i) $x=200$ mm, j) $x=250$ mm, k) $x=300$ mm, l) $x=350$ mm, m) $x=400$ mm, n) $x=450$ mm, o) $x=500$ mm, p) $x=550$ mm.	80
5.16 Iso-Tu contour at different cross-stream stations for $\lambda=15$ mm; a) $x=5$ mm, b) $x=10$ mm, c) $x=15$ mm, d) $x=25$ mm, e) $x=50$ mm, f) $x=75$ mm, g) $x=100$ mm h) $x=150$ mm, i) $x=200$ mm, j) $x=250$ mm, k) $x=300$ mm, l) $x=350$ mm, m) $x=400$ mm, n) $x=450$ mm, o) $x=500$ mm, p) $x=550$ mm.	82
5.17 Growth of varicose and sinuous modes in terms of maximum Tu corresponding the middle vortex pair: \square - $\lambda=10$ mm, \triangle - $\lambda=12.5$ mm, \diamond = 15 mm.	82
5.18 Evolution of maximum disturbance amplitude(κ_{max}) corresponding to the middle vortex pair: \square - $\lambda=10$ mm, \triangle - $\lambda=12.5$ mm, \diamond = 15 mm.	83
5.19 Power spectra of streamwise fluctuating velocity component of the middle vortex pair, at several streamwise stations: a) and b) $\lambda=10$ mm, c) and d) $\lambda=12.5$ mm, e) and f) $\lambda=15$ mm.	85
6.1 Characteristics of initial disturbances for riblet height $k/\delta_k=0.48$; a) riblet aligned at an angle of 45° to the flow and b) riblet aligned at an angle of 60° to the flow. Solid lines- Isolines of Tu; Dashed lines - Isolines of normalized streamwise component of velocity(u/U_∞).	91
6.2 An isolated Convergent riblet with rectangular cross-section; k - height, b - base width	92
6.3 Power spectra of the streamwise fluctuating velocity with respect to different riblet heights.	92

List of Symbols and Acronyms

2D two-dimensional

3D three-dimensional

rms root mean square

α Dimensional wavelength parameter = $(2\pi/\lambda_m)$

δ Blasius boundary layer thickness in mm

δ_k Blasius boundary layer thickness at the leading edge of the convergent riblet, in mm

η Non-dimensional similarity variable = $(y\sqrt{\frac{U_\infty}{\nu x}})$

κ Non-dimensionalized disturbance amplitude

λ Spacing between convergent riblets, in mm

λ_m Distance of the spanwise inflection in the mean velocity contour

ν kinematic viscosity of air - $15.68 \times 10^{-6} \text{ m}^2/\text{s}$

ν_{sc} viscous diffusion rate in Schmidt number

ω Mean vorticity vector

ϕ_{uu} Power spectral density of the streamwise fluctuating velocity

A, B hot-wire calibration constants

a_n Fourier coefficient corresponding to amplitude disturbance modes

A', B' temperature compensated hot-wire calibration constants

A_s Streak amplitude

A_w Windward enclosed area of the convergent riblet

b Base width of the riblet

D_{sc} mass diffusion rate in Schmidt number

E Voltage output of the CTA system in milliVolts

E^* temperature compensated voltage output of the CTA system in milliVolts

f frequency, in Hz

k Roughness height in mm

k_x Streamwise wavenumber, in m

Re_d Reynolds number with respect to diameter (d) of the smoke wire ($U_\infty d/\nu$)

Re_k Reynolds number with respect to height (k) of the convergent riblet ($U_\infty k/\nu$)

S Sharp edge of the arms of the riblet

T Leading edge of the convergent riblet

T_a ambient temperature

T_w hot-wire temperature

Tu Turbulence intensity

U_∞ free stream velocity in m/s

U' Total disturbance of time-averaged streamwise component of velocity

u_d Mean streamwise component of velocity at downwash

u' Fluctuating streamwise velocity in m/s

\hat{u} instantaneous streamwise velocity in m/s

u_k Streamwise velocity at height k) of the riblet, in m/s

u Time averaged streamwise velocity in m/s

u_u Mean streamwise component of velocity at upwash

V Convergent riblet's trailing vertex

x Streamwise co-ordinate measured from trailing vertex of the convergent riblet

x' Streamwise co-ordinate measured from virtual leading edge

x_{vle} Streamwise distance of Virtual Leading edge from the geometrical leading edge

y Wall-normal co-ordinate

z Spanwise co-ordinate

Chapter 1

Introduction

1.1 Background

The well-known viewpoint on the anatomy of transitional boundary layers is that they include streamwise or longitudinal vortices. Streamwise vortices, which are the predominant flow structures in the end stages of transition result from the nature and evolution of the initial disturbances that are infiltrated into the boundary layer, a phenomenon known as receptivity. The various paths by which receptivity can lead to transition are well depicted by the transition road-map, as shown in figure 1.1, laid down by Morkovin et al. (1994). In a zero pressure gradient Blasius boundary layer, which is of primary concern here, the infiltration of the disturbances is dependent upon the level of free-stream turbulence intensity and surface roughness. For very small disturbances, this relates to path A in the transition road-map, the streamwise vortices results from the initiation, development, and growth of the 2D Heisenberg-Tollmien-Schlichting(TS) waves. In analytical perspective, this scenario is concurrent with the linear stability theory that involves the exponential growth of eigenfunctions. In the realm of physical realizations, observation of initiation and growth of these disturbances demands controlled experiments. For instance, the classical ribbon experiments of Klebanoff et al. (1961) show that the linear stability theory disciplines the nature of initial disturbances in the wind tunnel. In their experiments, the initiation of TS waves was exercised by controlled oscillation of the ribbon in the boundary layer alongside maintaining the free stream turbulence intensity level less than 0.02%.

A more practical scenario is where the influence of random isolated surface roughness in the

boundary layers and that of free stream turbulence could not be eliminated. In this case, the nature of the initial disturbances, that are predominantly 3D, depends on the geometry of the surface roughness and its height influenced by the boundary layer. Early attempts to relate the various TS wave mechanisms to the roughness induced disturbances ended in vain. Also, the concern for instability was directed towards 2D disturbances in accordance to Squire's theorem which states that, for a 3D disturbance growing at a particular Reynolds number there exists a growing 2D disturbance at lower Reynolds number. Thus the link between the 3D roughness induced disturbances and transition was unlooked-for. This weak link that existed between the initiation and evolution of the roughness induced disturbances was later bridged by the phenomenon referred to as transient growth. By the rudiments of transient growth as put forth by Ellingsen and Palm (1975), it has that, in shear flows, the 3D disturbances can grow algebraically in time. The mathematical idea is that the wall-normal velocity/vorticity disturbance equations are not self-adjoint, thereby resulting in non-orthogonal modes which is in contrary to the well known TS wave mechanisms whose eigenmodes are orthogonal (Schmid and Henningson, 2001). The more important point at issue is that, in a Blasius boundary layer, where the eigenmodes are discrete and finite, as proved by Miklavcic and Williams (1982), the representation of an arbitrary disturbance should come about by continuous spectrum. It is this superposition of continuous spectrum that leads to the brief algebraic growth of the disturbance.

Treating the same temporal problem with the inclusion of viscosity, Hultgren and Gustavsson (1981) found that the growth of 3D disturbances is followed by viscous decay. Alongside the physical explanation of this problem, as put forth by Landahl (1980), the definition of transient growth lies in the very sense of the quasi-streamwise vortices. The upliftment of the low momentum fluid between a pair of streamwise counter-rotating vortices, referred to as upwash, flanked by the high momentum fluid, referred to as downwash, manifests as alternating low and high speed longitudinal streaks respectively. These streaks might either grow in time and experience a viscous decay or reach the maximum amplification and further incur a time dependent secondary instability that can drift the boundary layer to turbulence. The importance of transient growth can be well ascertained by taking a cursory glance, again, at the transition road-map where it can be seen that this route to transition is well linked by the transient growth phenomenon. Further,

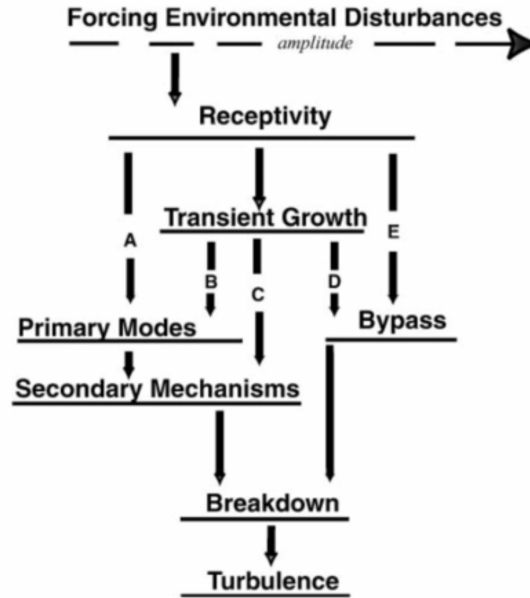


Figure 1.1: Transition road map as laid down by Morkovin et al. (1994).

within the context of fundamental research, the transient growth phenomenon could be an answer as to how the manifested disturbances could drift the flow to turbulence. Consequently, the advantages that emerge out is that the theory could act as a tool to determine the most unstable mode that could initiate the primary and secondary instability, the most common path to turbulence as shown in the review by Herbert (1988). In regards to engineering applications, like any instability mechanism, the applicability of transient growth to flow control cannot be neglected.

1.2 Motivation

In the event of pushing the boundaries of transient growth theory in relevance to boundary layers, the studies of Andersson et al. (1999), Luchini (2000) and Tumin and Reshotko (2001) were centred on the particular initial disturbance that offers maximum spatial growth hence referred to as optimal disturbances. It was found that for a Blasius boundary layer, the optimal disturbances were streamwise counter-rotating vortices with non-dimensional spanwise wavenumber of 0.45.

Wind-tunnel experiments of Westin et al. (1994) and Matsubara and Alfredsson (2001) con-

ducted in the light of transient growth showed that the evolution of the disturbance energy initiated by free stream turbulence was in excellent agreement to those predicted by the optimal perturbation theories. It should be mentioned, however, that the initial disturbance were far from optimal compared to that considered in the theories. In what follows, any 3D disturbance that is initiated in the boundary layer tends to manifest as streamwise counter-rotating vortex pair.

In contrast to the disturbances initiated by free-stream turbulence, first experiments involving surface roughness, conducted by White and co-workers (White and Reshotko 2002, White 2002 and White and Ergin 2003a) showed anomalies with respect to the streamwise location of the maximum energy growth. In their experiments, disturbances were initiated by array of cylindrical roughness elements. It is well known that these roughness elements, with increasing roughness Reynolds number based on height (Re_k) induce horseshoe vortices, one of the coherent structures in a turbulent boundary layer. These horseshoe vortices upon near wall interaction spews out low momentum fluid that later breaks down to hairpin vortices. Following the discrepancy, almost all numerical and physical experiments conducted to study the continuous spectrum of the initial disturbances due to surface roughness inadvertently results in flow kinematics subjected to hairpin vortices - works of White et al. (2005), Rice (2004), Fischer and Choudhari (2004), Fransson et al. (2004), all of whom used cylindrical roughness elements, and more lately that of Cherubini et al. (2013) who used a smooth bump as a disturbance source are a few to mention. The evolution of the disturbances in all these cases were found to be unique. In this perspective, however, putting all known possible roughness elements (Lin, 2002) to test is not feasible. It is in this context that the relevance of the present work nests in.

Having pointed out the dependence of the disturbance growth on the roughness geometry, which forms the main impetus of the present work, a directionally-dependent surface roughness, namely, convergent riblet has been put to test within the context of transient growth and instability of longitudinal streaks. The flow structure induced by the convergent riblet, as will be discussed in Chapter 4, is a pair of counter-rotating vortex tubes convected along the downstream either by the free stream or by the mean shear in the boundary layer and is devoid of horseshoe and hairpin vortices. Few other surface roughness like wishbone vortex generators and forwards wedge is suspected to offer kinematically similar flow.

1.3 Objectives and Scope

The main objective of the present work is to experimentally investigate, within the context of transient growth and instability of longitudinal streaks, the evolution of the disturbances initiated by convergent riblet in Blasius boundary layer by means of hot-wire anemometry. More specifically, the two main objectives are

i) To study the initiation and evolution of the disturbances induced by an isolated convergent riblet. The development of the disturbances for varied riblet height to boundary layer thickness ratio will be presented in terms of mean and fluctuating velocity distributions and amplification parameters of the vortex growth.

ii) To study the evolution of instability modes induced by forced wavelength disturbances and compare it with that of the isolated convergent riblet. The analysis will be presented for in-line arrangement of riblets for three different wavelengths- $\lambda = 10\text{mm}$, 12.5mm and 15mm .

1.4 Organization of Thesis

The experimental results and the analysis of the study as mentioned earlier are presented in 6 chapters as briefly outlined in the following.

The background, motivation, objectives and scope of the present study is presented in Chapter 1, followed by Chapter 2 that comprises an extensive literature review on the theory of transient growth, the streak instability and the applicability of transient growth to roughness induced disturbances. The experimental set-up, instrumentation and experimental procedures are described in Chapter 3.

The results and discussions are presented in the next two chapters. Chapter 4 discusses the disturbance growth due to an isolated convergent riblet. In-depth analysis was done for three different cases that corresponds to three different riblet height to boundary layer thickness ratio. Chapter 5 comprises the results of the forced wavelength disturbances mainly focussing on the frequency characteristics of the instability modes and its variation with isolated riblet case.

Finally, the main conclusions and recommendations for future work that could be undertaken from the present results are given in Chapter 6.

Chapter 2

Literature review

2.1 Transient growth: Origin and Evolution of the theory

Amidst the development of 2D linear instability theories, the first principles of transient growth was put forth by Ellingsen and Palm (1975). Considering the infinitesimal 3D initial disturbances, they solved the linearized stream function/velocity equations and found the streamwise velocity disturbances grew linearly with time. Independent of the initial disturbance, they found the solution of the equations to be a closed set of steady, streamlines that correspond to streamwise counter-rotating vortices. Physical explanation of the problem was given by Landahl (1980) who referred to the generation of low momentum streaks between a pair of counter-rotating vortices as 'lift-up' mechanism. However, these analysis were carried out by considering the inviscid problem. Hultgren and Gustavsson (1981) studied the evolution of 3D disturbances, taking viscosity into consideration, finding the brief growth of the disturbances to be followed by a viscous decay.

The mathematical idea is that the disturbance equations are not self-adjoint and that the eigenmodes are non-normal (Schmid and Henningson, 2001). Basically, in hydrodynamic instability theory, the instability is driven by the most amplified discrete eigenmodes of the Orr-Sommerfeld disturbance equations. However, in the case of transient growth, the instability is driven by the superposition of continuous eigenmodes. Despite the decay of eigenmodes in the subcritical region, a brief growth of disturbances occurs prior to the exponential decay due to the superposition of continuous eigenmodes.

Butler and Farrell (1992) further studied the growth of the non-orthogonal eigenmodes of a particular 3D initial disturbance whose energy growth were maximum. Such initial disturbances were referred to as optimal perturbations. They also pointed out that an arbitrary initial condition comprised of many non-orthogonal eigenmodes whose interactions brought about a complicated three dimensional growth. Subsequently, Farrell and Ioannou (1993) documented that the two types of motion that caused the maximum growth were: i) Streamwise vortices growing by advection of mean streamwise velocity to form streamwise streaks and ii) upstream tilting waves growing by the down gradient Reynolds stress mechanism of two-dimensional shear instability. Henningson et al. (1993) studied the transient growth phenomenon, using direct numerical simulations, in the case of bypass transition by considering various initial disturbances in the Blasius boundary layer. They concluded that for a particular strong initial disturbance, the brief growth of the disturbances resulted in longitudinal streaks that roll up to form vortices before breakdown to turbulence spots. Reddy and Henningson (1993) went on to study the optimal perturbations in Poiseuille and Couette flows and pointed out that there exists a critical surface function below which there is no growth and above which the growth is maximum. These studies were thus rather concentrated on the temporal evolution of the disturbances with parallel flow approximations, the rudiments of spatially evolving optimal perturbations, in conjunction with non-parallel effects, as further brought about by Andersson et al. (1999) and Luchini (2000) based on the solution of the linearised, perturbed wall-normal velocity/vorticity system of equations. The non-zero forcing term in the normal vorticity equation allowed the coupling of Squire and Orr-Sommerfeld modes thus leading to algebraic growth of the disturbances. Such studies were therefore set around prediction of optimal disturbances associated to a non-dimensional spanwise wavenumber 0.45 for Blasius boundary layer. It must be mentioned that the disturbances they considered were initiated at the leading edge outside the boundary layer and at the location of maximum growth, the disturbances being manifested inside the boundary layer.

Further studies aimed at experimentally verifying transient growth were those by Westin et al. (1994) and Matsubara and Alfredsson (2001) who studied the evolution of 3D disturbances induced by free stream turbulence, in the zero pressure-gradient Blasius boundary layer. They found their results concurrent with those of Andersson et al. (2001) and Luchini (2000). Westin

et al. (1994) specifically concluded that the transient disturbances developed into longitudinal structures with a spanwise spacing comparable to boundary layer thickness, finding the spanwise spacing to be dependent on forcing conditions. Matsubara and Alfredsson (2001) arrived at same conclusions from their experiments.

The link between transient growth and the roughness-induced disturbances was particularly highlighted in the experiments of Kendall (1981) on stationary horseshoe vortices induced by isolated 3D cylindrical roughness elements. Between the vortex pair, along the centerline of the cylindrical roughness element, the flow was directed towards the wall and along the sides, the vortex pair upon interaction with the wall lifted up the low momentum fluid what was pictured as 'lift-up' mechanism as thoroughly discussed in Landahl (1980).

Following this, further studies have looked at the influence of roughness induced disturbance growth in flat plate boundary layer. For instance, the influence of stationary streamwise vortices in the flat plate boundary layer was studied by Bakchinov et al. (1995). He used square ribs in his experiments to induce streamwise vortices and found that the instability arose due to the wave riding over these vortices and not the vortices as such. Almost a decade later, White (2002) further attempted to address the key predictions of transient growth disturbances. The roughness elements (adhesive dots) were arranged in-line with specific spacing. The initial disturbances were a pair of counter-rotating streamwise stationary vortex. With respect to the initial disturbances, he found discrepancies in streamwise location of the maximum kinetic energy growth as predicted by the theories and concluded that the disturbances in his experiments were sub-optimal. Fransson et al. (2004) performed similar experiments and explained that the discrepancies arose as the disturbances were initiated inside the boundary layer in contrast to the optimal disturbances considered by Andersson et al. (1999) and Luchini (2000) wherein the initial disturbances were outside the boundary layer. In order to understand the contribution of continuous spectrum of the Orr-Sommerfeld and Squire modes, within the scope of receptivity, Tumin (2003) solved the Cauchy problem of a finite growth rate of disturbances, the solution of which was a bi-orthogonal eigenfunction system. Similar bi-orthogonal decomposition of perturbations was carried out by Denissen and White (2009) in order to study the complex perturbations induced by roughness elements. Their main conclusion was that the occurrence of the sub-optimal disturbance, whose

amplitude lies in the higher end of the streamwise wavenumber space, in the lower part of the boundary layer is the reason as to why the disturbances decayed upstream than the optimal perturbations.

This discrepancy later triggered a series of experiments conducted in the light of behaviour of roughness induced transient disturbances subjected to varying initial disturbances. For instance, Ergin and White (2006) studied unsteady initial disturbances induced by a cylindrical roughness element. They suspected that with the increasing height, the inflection points in the wall-normal and spanwise directions were due to Kelvin-Helmholtz-type instability mechanism that is associated with hairpin vortices. White and Ergin (2003b) also documented the errors in the observed initial disturbances in the near downstream of the roughness elements when the position of the wall normal was estimated by least square fits of the data obtained from hot-wire measurements. In another paper, White and Ergin (2003a) performed spectral analysis and subsequently studied the downstream evolution of the energy components. They also reported that the disturbance energy scaled with k^4 (where k is the roughness height). This was subsequently verified by White et al. (2005) and Rice (2004). Ergin and White (2005) and White et al. (2005) suggested a model function for the growth of disturbance kinetic energy contained in wavelengths that scaled as one-third and one-fourth the roughness spacing with the aim of investigating the effect of varying geometry on the disturbance energy as well as the effect of roughness diameter on the disturbance energy. With decreasing roughness diameter, the disturbances were found to undergo transient growth to pure decay. DownsIII et al. (2008) also investigated experimentally the evolution of steady and unsteady boundary-layer disturbances that were generated by quasi-random distributed roughness. He found that the spanwise disturbance mode corresponding to one-fourth the roughness spacing underwent the maximum growth. Fischer and Choudhari (2004) carried out numerical simulations on circular disks similar to that used by White (2002). His work complimented the findings of White and Ergin (2003a).

2.2 Streak instability

The streamwise aligned vortices, by the lift-up mechanism, induces elongated streamwise streaks with significant spanwise modulation. Due to the non-linear evolution, the streaks incur either of the four instability modes - fundamental sinuous, sub-harmonic sinuous, fundamental varicose

and sub-harmonic varicose modes.

A plethora of numerical experiments were carried out by Brandt and co-workers (Andersson et al. 2001, Brandt and Henningson 2002, Brandt et al. 2003, Zuccher et al. 2006, Brandt 2007, Schlatter et al. 2008) to study the breakdown of longitudinal streaks, streak interactions and the difference in the manifestation of secondary instability in the presence and absence of Tollmien-Schlichting waves. They tested the behaviour of the longitudinal streaks with respect to varying initial disturbances. In addition, Cossu and Brandt (2002) carried out numerical simulations to conclude that the large amplitude streamwise streaks stabilized the Tollmien-Schlichting waves. It should be mentioned that the streak instability discussed in these studies was associated with hairpin vortices.

Very few studies were carried out in order to relate the instabilities of the naturally occurring transition structures to roughness induced instability. For instance, Boiko et al. (2012) experimentally investigated the instability of backward-facing step flow. He mounted cylindrical roughness elements on the separation line to initiate longitudinal streaks. The most important finding was that the laminar flow destabilization accompanied the transient behaviour of the stationary disturbance in the separation region thus implying the substantial contribution of the non-modal growth. Lately, Denissen and White (2013) performed calculation to show how the sub-optimal disturbances destabilize the laminar boundary layer leading to secondary instability. Their main finding was that, increasing the modal content led to decreased stability. Experiments of Asai et al. (2002) who used wire-gauze to initiate a single low speed streak found that the varicose mode was prone to Kelvin-Helmholtz instability that successively manifested as hairpin vortices. He also documented that the varicose modes were more sensitive to the streak width and died out rapidly. However, the sinuous modes, that exhibited wake-like instability, was insensitive to the streak width and continued its exponential growth. Subsequently, the experiments of Konishi and Asai (2004) by forced wavelength disturbances showed that the occurrence of harmonic and sub-harmonic instability were sensitive to the wavelength of the disturbances. More recently, Cherubini et al. (2013) conducted numerical simulations in the light of global optimization. They used smooth bumps as roughness elements and they found that, for low roughness height, the disturbances experienced transient growth while for larger roughness height the varicose modes set

in to induce hairpin vortices similar to the experiments of Asai et al. (2002)

Chapter 3

Experimental Details

3.1 Experimental Set-up

Qualitative and quantitative experiments were conducted in two different facilities whose free-stream conditions were exercised to be the same. Smoke-wire flow visualization experiment, from which qualitative data was obtained, was performed in a straight plexiglass square duct that was connected to a low speed, blow down type wind tunnel as shown in figure 3.1. The flow from the centrifugal fan passed through honeycomb and series of fine meshes of decreasing size in the settling chamber. Following the settling chamber was a three dimensional contraction that reduces the cross sectional area to 160 mm x 160 mm thus achieving a contraction ratio of 9:1. The contraction section was 300 mm long and was followed by the test section with cross-sectional area 160 mm x 160 mm and length 1500 mm. The free stream turbulence intensity at velocities 1-5 m/s was less than 0.25%. A container holding paraffin oil was mounted on the top of the section and a nickel-chromium alloy resistance heating wire, with diameter of 0.193 mm, originating from the container was held taut across the wind tunnel. The oil container with the wire was fixed on a simple two-axis manual traversing mechanism to allow fine adjustment of the smoke wire. As the wire was coated with paraffin oil from the container, a constant DC power supply heated up the wire to produce a white smoke. A laser sheet of 532 nm wavelength was used to illuminate the flow field. The right angle illuminations and the positions of the camera for visualization of streamwise planes and cross planes are shown in figure 3.1. Due to the difference in the densities of the smoke traces and air, the buoyancy caused the streaklines to shift

sideways. The choice of flow velocity was also restricted by the Reynolds number Re_d (based on the diameter of the wire) so as to avoid the initiation of Von Karman vortex street. In this respect experiment was carried out for flow velocity whose corresponding Re_d was about 36 and hence the roughness Reynolds number Re_k was matched with respect to hot-wire measurements by changing the riblet height. Thus the presence of smoke wire did not perturb the flow and the flow physics observed was solely due to the riblet.

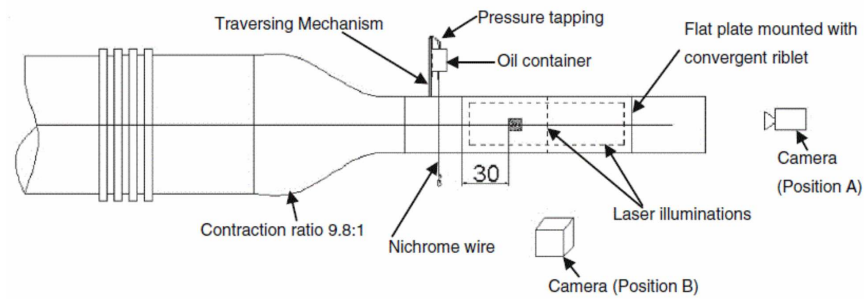


Figure 3.1: Schematic of smoke-wire flow visualization Set-up.

The hot-wire experiments, which comprise the bulk of the study, were conducted in a straight plexiglass test section connected to a blow down type wind tunnel as shown in figure 3.2. The tunnel was earlier used by Mitsudharmadi et al. (2004) and Tandiono et al. (2013) to study Gortler instability problem. The test section had a rectangular cross-section of 150 mm x 500 mm and a honeycomb and five fine-mesh screens with decreasing mesh-sizes were installed in the settling chamber prior to the contraction. The screens had the specification of ASTM E161 No. 35, 40, 50, 60 and 80 with the mesh-size of 500, 425, 300, 250 and $180\mu\text{m}$ respectively from the blower to the entrance of the contraction section. The contraction consisted of a 300 mm straight channel of 600 mm x 600 mm cross-section followed by a two dimensional contraction of 4:1 which reduces the cross-section to 150 mm x 600 mm.

A perspex plate, as a test surface, was mounted inside the straight plexiglass duct by means of slots at the duct side walls at a distance of 50 mm from its bottom surface. The distance between the test surface and its top cover was 100 mm. By this arrangement, the aspect ratio of the test section was achieved to be 6. The wind tunnel in conjunction with the straight duct were connected by a straight channel of 150 mm length. The test surface had a sharp leading edge

with an angle of 15° which was CNC machined. The free stream turbulence levels in the test section were less than 0.3% for a free stream velocity (U_∞) range of 1.0 to 5.0 m/s. Evidently, from figure 3.3 and 3.4, it can be seen that the set-up yielded a zero-pressure gradient Blasius boundary layer. The flow is later shown to be non-accelerating till 600 mm downstream of the riblet's trailing vertex (V in figure 3.5). Measurements were thus carried out within this region to assess the pertinent flow physics.

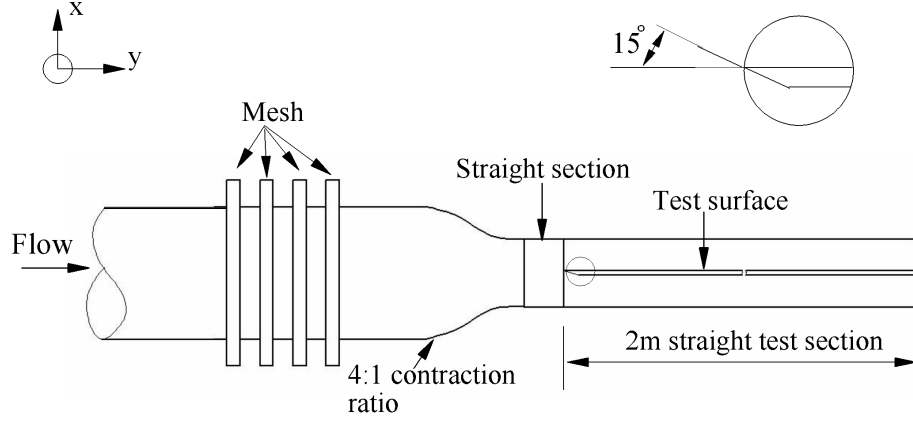


Figure 3.2: Schematic of the wind tunnel Set-up for hot-wire measurement.

A convergent riblet as shown in figure 3.5, manufactured using rapid prototyping with ceramic as the green material, was mounted at 320 mm from the leading edge of the test surfaces of both the set-ups. At this streamwise distance, the local Blasius boundary layer thickness was 6.4 mm. The maximum random error in height of the riblet due to the shrinkage of the green material was found to be less than 0.1%. Two systems of laboratory co-ordinates with different origins had been specified. Co-ordinates (x, y, z) had its origin at the trailing vertex of the riblet (V in figure 3.5), while (x', y, z) has its origin at the center of the virtual leading edge (x_{vle}) of the test surface plate. The virtual leading edge was obtained by determining the least squares fit of the momentum thickness and displacement thickness as suggested by White (2002). With respect to momentum thickness, the leading edge was found to occur at 7 ± 1 mm and with respect to displacement thickness, the leading edge was found to occur at 15 ± 1 mm. An average of these values $x_{vle} = 4$ mm was later subtracted from the geometrical leading edge to give the appropriate streamwise distance, x' . The similarity variable $\eta = (y \sqrt{\frac{U_\infty}{\nu x'}})$ and the local Blasius boundary layer thickness $\delta (= 5 \sqrt{\frac{\nu x'}{U_\infty}})$, where ν is kinematic viscosity of air) were calculated with respect to x' .

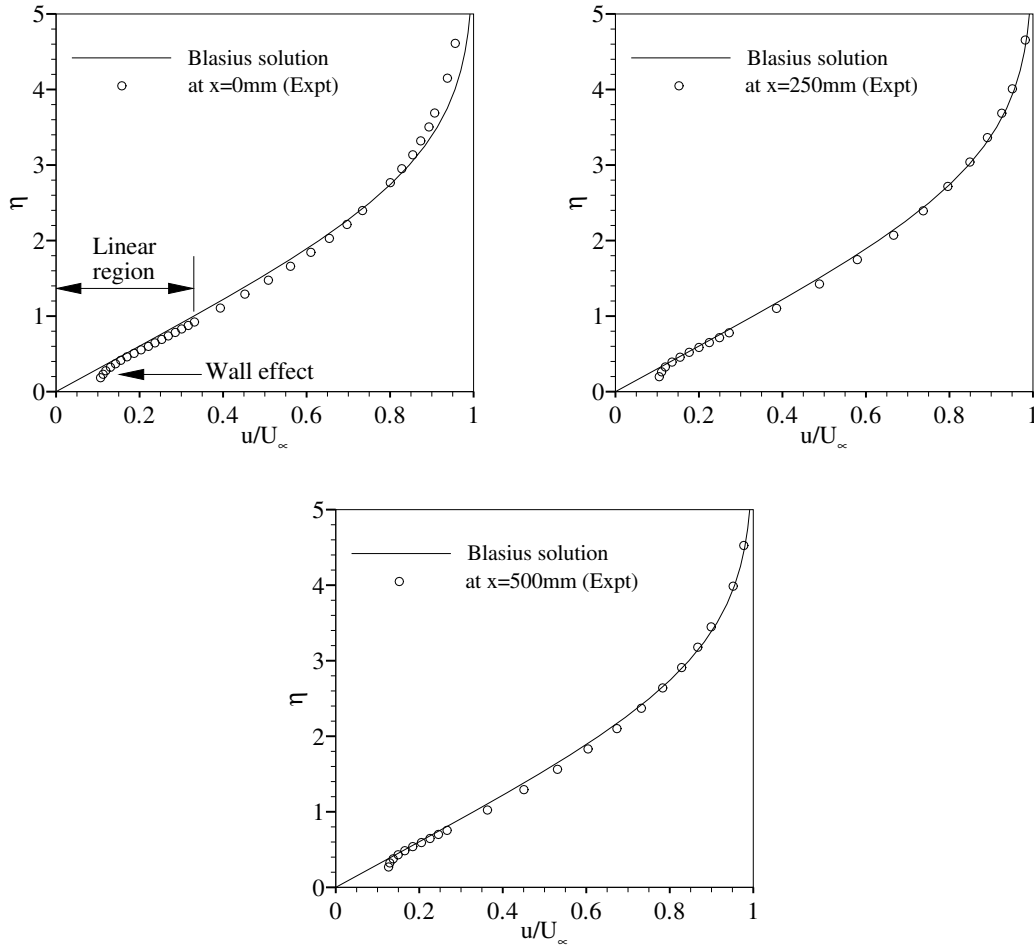


Figure 3.3: Blasius boundary layer at several streamwise stations.

The riblet cross-section was chosen to be an isosceles triangle in order to avoid a large two dimensional separation bubble that would arise behind the riblet due to adverse pressure gradient. The near Gaussian-like profile of the riblet would hinder the formation of a huge separation bubble. An angle of 30° inclination of the riblet to the flow was chosen in this study.

3.2 Instrumentation

The measurement process was carried out using computer controlled program. The block diagram of the hot-wire anemometer system is shown in figure 3.6.

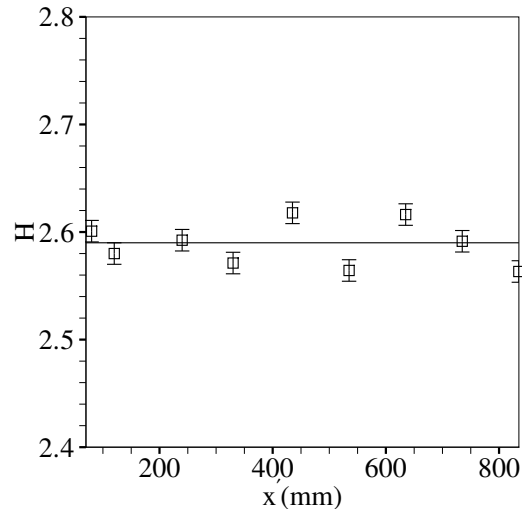


Figure 3.4: Shape factor, H , showcasing Zero pressure gradient boundary layer development. $H=2.59$ corresponds to Blasius solution.

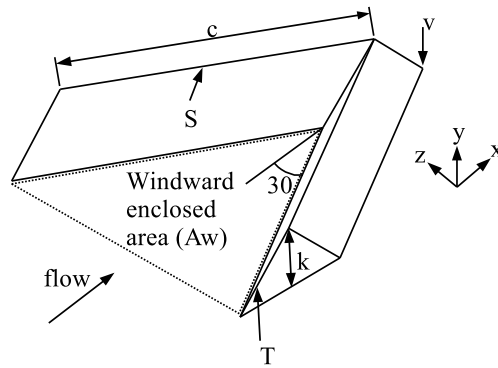


Figure 3.5: An isolated convergent riblet.

3.2.1 Hot Wire Anemometer and Sensors

A single-normal (SN) hot-wire probe (Danter 55P15) with a platinum-plated tungsten wire sensor of diameter $5 \mu\text{m}$ and length 1.25 mm was used to obtain mean and fluctuating streamwise velocity data. The probe was operated in a Constant Temperature Anemometer (CTA) mode by connecting it to a CTA 90C01 Dantec module. Overheat ratio was maintained at 1.8 throughout the experiment. The raw analog signals from the 90C10 module was passed through an individual low pass analog filter unit before being digitized using analog to digital (A/D) data converter system.

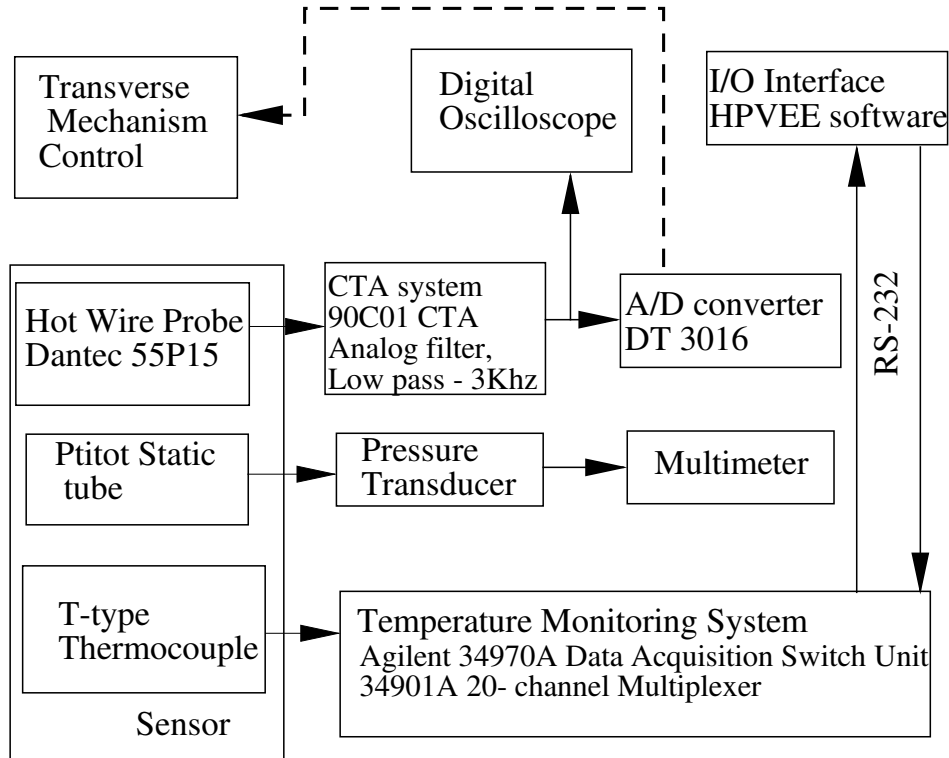


Figure 3.6: Block diagram of hot-wire anemometer system.

The hot wire probe in conjunction with a Pitot-static tube, connected to a pressure transducer (Setra 235, 0-0.1 psid), was held in the traversing system and moved in the free-stream region to calibrate the hot-wire and to monitor the free-stream velocity as well.

The free-stream temperature was measured using a T-type thermocouple that was held in the traversing system alongside Pitot-static tube and hot-wire system. The thermocouple was connected to an Agilent 34970A Data Acquisition/Switch Unit equipped with 34901A 20-Channel Multiplexer. The temperature data was retrieved from the data acquisition module to the computer using a RS-232 cable. The measured temperature was later used to compensate the hot-wire voltage readings due to the change in ambient temperature during the hot-wire calibration and measurements.

A two-axis traverse mechanism system was used to move the sensors in the wall-normal (y) and spanwise (z) directions. Automation was exercised by two-stepper motors. The stepper motors were coupled to the screw rods that were arranged perpendicularly to each other.

3.2.2 Data Acquisition System

An analog to digital (A/D) data converter system was used to digitize the analog signals from CTA system and pressure transducer. A high-speed multifunction DT3016 board and a DT740 formed the constituent components of the A/D converter system. The board had an analog I/O resolution of 16 bits with a maximum sampling frequency of 250 kHz for a single channel. In addition, the ability to send digital signal with a maximum D/A throughput of 100 kHz made it possible to control the movement of stepper motors from the computer.

Agilent VEE Pro software was used for data collection and for control of stepper motors. The raw data and time averaged data obtained from the computer were later post-processed using commercial softwares like TECPLOT and MATLAB.

3.3 Experimental Procedures

Prior to calibration and subsequent boundary layer measurements, the CTA system was put to square-wave response test at the maximum velocity expected in the experiments. It was found that the response was greater than the sampling rate of the hot-wire signal which was 6000 Hz. The detail of the experimental procedures is given below.

3.3.1 Calibrations

Prior to velocity measurements, in-situ calibration of the hot-wire sensor was carried out. The sensor was calibrated against a pressure transducer which was connected to a Pitot-static tube. The pressure transducer was calibrated against a micro-manometer. The calibration was based on King's law with temperature compensation. It was accomplished in free-stream flow over the range of velocities encountered within the boundary layer.

3.3.1.1 SN-probe calibration

The pitot-static tube in conjunction with the sensor was held in the free-stream prior to calibration. The analog signals from both pressure transducer and CTA system were sampled simultaneously. The pressure transducer signal was sampled at 500 Hz for 10 seconds as against hot-wire signal which was sampled at 6000 Hz for 21 seconds. Before being digitized, the raw signal from the CTA system was low-pass filtered at 3000 Hz. The voltage output of pressure

transducer was converted into free-stream velocity data.

The voltage output of the CTA system E and the free-stream velocity U_∞ was assumed to be related by King's law,

$$E^2 = AU_\infty^{0.45} + B \quad (3.1)$$

where A, B are calibration constants. By taking into account the temperature compensation, Eqn. 3.1 can be modified as,

$$E^* = \frac{E^2}{T_w - T_a} = A'U_\infty^{0.45} + B' \quad (3.2)$$

where T_w is the hot-wire temperature, T_a is the ambient temperature and A', B' are the temperature compensated calibration constants. The hot-wire temperature was determined based on the overheat ratio used in the measurement. Later, E^* was plotted against U_∞ , and linear regression was performed to obtain the calibration constant A' and B' . In the midst of boundary layer measurements, calibration check was carried out for the operating free-stream velocity. Experiments were resumed if the calibration error was within $\pm 1\%$, else the whole data was discarded and the experiment was repeated.

3.3.2 Measurement of Mean and Fluctuating Streamwise Velocities

The mean and fluctuating velocities were measured by means of SN-probe. In the measurement process, the hot-wire signal was low-pass filtered at 3000 Hz and sampled at 6000 Hz for 21 seconds. The output voltage of CTA system was subsequently converted to velocity data by interpolation of the calibration points.

The instantaneous velocity \hat{u} obtained from the hot wire measurement can be decomposed as:

$$\hat{u} = u + u' \quad (3.3)$$

where u is the mean velocity and u' is the fluctuating velocity component. The mean velocity is obtained by time-averaging the sampled data, which is calculated as:

$$u = \frac{1}{n} \sum_{i=1}^n \hat{u}_i, i = 1, 2, \dots, n \quad (3.4)$$

where n is the total number of samples of velocity data within the sampling duration at a given

point. By this calculation, the maximum random error in the free stream velocity was found to be under 0.2%.

The fluctuating velocity component is expressed in the turbulence intensity Tu , which is obtained from:

$$Tu = \frac{1}{u} \sqrt{\frac{\sum_{i=1}^n (\hat{u}_i - u)^2}{n}}, i = 1, 2, \dots, n \quad (3.5)$$

The maximum random error in Tu was found to be 0.4%. The above procedures were repeated at every point of the measurement domains.

The measurement of streamwise velocity component were carried out at streamwise (x) locations. In the case of boundary layer measurement by employing an isolated riblet, the measurement was carried out in steps of 0.5 mm along the spanwise (z) direction for about 30 mm and along the wall-normal (y) direction, in steps of 0.1 mm near the wall and in steps of 0.5 mm near the boundary layer edge. In the case of forced wavelength disturbances, 3 vortex pairs were captured with the spanwise (z) and wall-normal (y) resolution same as that of the isolated riblet case. A total of 28 y -locations were measured inside the boundary layer in the wall-normal direction.

3.3.3 Determination of wall position

In order to determine the position of the wall, 10 points in the linear region of the Blasius boundary layer were measured and least squares linear fit was performed to determine the wall-normal position. This method is similar to that adopted by White (2002), and Tandiono et al. (2009) in an attempt to measure wall shear stress induced by Gortler vortices. Basically, near-wall velocity measurement is identical with the streamwise velocity measurement (Section 3.3.2). In order to estimate the wall position, The measurement was carried out by SN-probe to capture the region where the velocity profile was linear. The hot-wire was initially positioned very near to the test surface (perspex plate). The streamwise velocity measurement was subsequently performed with the step size of 50 μm across the boundary layer so that at least 10 points fall in the linear region. As shown in figure 3.3, the points in the linear region were used for the extrapolation. Also in figure 3.3, the anomalies in the streamwise velocity due to the wall effect can be well observed. The wall effect arose due to the heat transfer between the probe and the perspex plate. The ex-

trapolation was performed leaving those points which were affected by the wall region. In the case of forced wavelength disturbances, the hot wire was moved to spanwise position where the flow was Blasius and similar steps were repeated to determine the wall position.

3.4 Uncertainty analysis

The measurand is the instantaneous streamwise component of velocity (u m/s). The dependence of streamwise component of velocity measurement to the half bridge voltage makes it a multi-variate system. This calls for Calibration uncertainty analysis. Strictly speaking, the uncertainty in the voltage signal as it passes from bridge to the low pass filter would add up to a net uncertainty in the resultant voltage. However, the uncertainties here are considered negligible. The only source that would add up to uncertainty is the stray emf. Care was taken that to common ground the instruments to get rid off emf. Given that, a simple rearrangement of equation 3.1 results in

$$U_{\infty} = \sqrt[n]{\frac{E^2 - A}{B}}, n = 0.45 \quad (3.6)$$

Following Coleman and Steele (1998), the propagation of uncertainty in the king's law calibration is determined by taking the standard deviation of the calibration points and is given by

$$u_x^2 = u_{ref}^2 + \sum_{i=1}^m \left(\partial U / \partial U_i \sigma \right)^2 \quad (3.7)$$

where u_x is the uncertainty in velocity, U_i is the velocity at i -th calibration point, m is the number of calibration points, u_{ref} is the reference velocity and σ is standard deviation which is

$$\sigma = \sqrt{\frac{1}{m-3} \sum_{i=1}^m [U_i - U(E_i)]^2} \quad (3.8)$$

where $m-3$ is the number of degrees of freedom.

The partial derivative is estimated by simple finite difference

$$\partial U / \partial U_i \approx \frac{U(U_i + \epsilon) - U(U_i)}{\epsilon} \quad (3.9)$$

where ϵ is the small increment to the calibration point velocity.

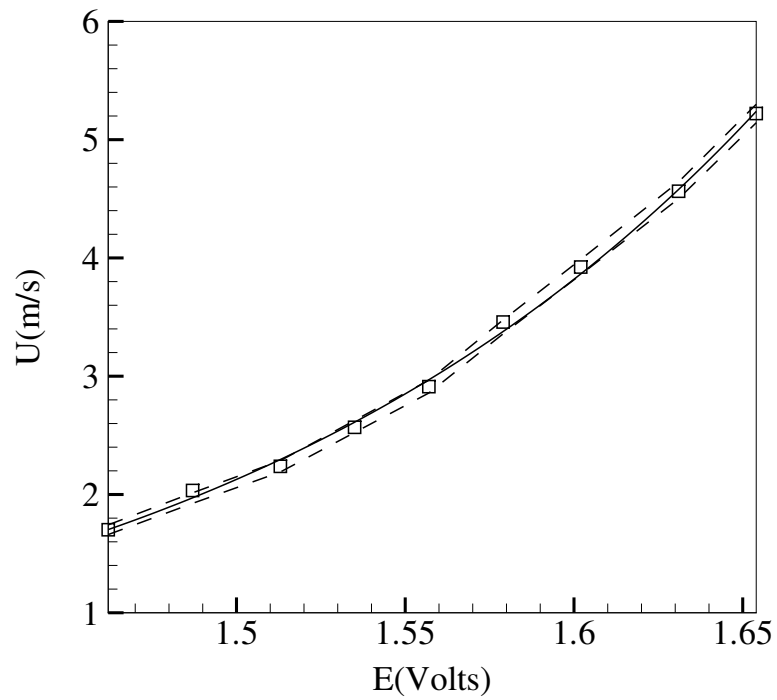


Figure 3.7: King's law curve fit showing uncertainty; — Curve fit, - - - Uncertainty

Figure 3.7 plots curve fit along with its uncertainty. Apart from the uncertainty in the velocity measurements, the systematic error in the traversing mechanism is due to the stepper motor. This might result in uncertainties in wall normal variable estimates namely boundary layer thickness and momentum thickness. However, this was found to negligible as evident from the Blasius boundary layer profile in figure 3.3

Chapter 4

Influence of an Isolated Convergent Riblet

4.1 Introduction

Physical realizations concerning isolated surface roughness were mainly focussed on hemispherical and cylindrical protuberances, both of which induces hairpin vortices - the most dominant coherent structure that occurs in a naturally occurring transitional boundary layers. In the case of hemispherical protuberance, hairpin vortices are induced by the balance between the centrifugal and normal pressure gradient forces (Acarlar and Smith, 1987). In the case of the cylindrical roughness surface, the horseshoe vortices upon interaction with the wall lifts up the spires of low momentum fluid which in turn on interaction with the outer high momentum fluid might result in a symmetric or single-legged hairpin vortex (Doligalski et al., 1994). The interaction of the vortex system with its peninsula which is the Blasius boundary layer vortex lines leads to varying vorticity dynamics and hence varying growth of the disturbances.

In the light of aberrations in flow kinematics, subjected to varying geometry of the surface roughness, that in turn leads to varying perturbation energy growth, this chapter discusses the initiation and evolution of the disturbances initiated by an isolated convergent riblet of different heights. The flow structure is a pair of streamwise counter-rotating vortex, as will be discussed in the forthcoming section. As mentioned earlier in chapter 1, geometry of convergent riblet being similar to that of a wishbone vortex generator and vane vortex generators inclined at an angle to

the flow, the study should generalize the nature of initial disturbances and its evolution of this particular class of roughness elements that are directionally dependent. More specifically, this chapter addresses:

- i) The conjecture of formation of the quasi-streamwise vortices with the aid of smoke-wire flow visualization technique
- ii) The characteristics of initial disturbance from the measured hot wire anemometer data.
- iii) The evolution of the initial disturbances and
- iv) The streak characteristics.

Subsequently, the arguments concerning the differences between the flow kinematics subjected to convergent riblet and that due to the hairpin vortices are put forth.

4.2 Flow kinematics

Six sets of experiment, as shown in Table 4.1, concerning different heights (k) of the riblet were performed.

Table 4.1: Test cases; δ_k - Blasius boundary layer thickness at the leading edge of riblet (at $x=320$ mm), u_k - Mean velocity at height k of the riblet.

$k(\text{mm})$	k/δ_k	c/k	$u_k(\text{m/s})$	$Re_k(u_k k/\nu)$
1	0.16	6	0.7	47
1.3	0.2	4.6	1	83
1.5	0.24	4	1	96
1.8	0.28	3.3	1.3	150
2	0.32	3	1.4	184
3	0.48	2	2	380

In order to bring out the possible flow kinematics that could arise from the roughness receptivity, the smoke flow visualization for $k/\delta_k=0.24$, corresponding to height $k=1.5$ mm and $k/\delta_k=0.48$, corresponding to height $k=3$ mm are presented here.

The smoke traces dispersed in the fluid are that of paraffin oil. The Schmidt number (ν_{sc}/D_{sc}), where ν is the viscous diffusion rate due to the fluid and D is the mass diffusion rate due to smoke traces, is about order of magnitude 5 (Cimbala et al. 1988, Smits and Lim 2000). Hence the probable flow physics is discussed to the extent where the species (the smoke particles) are distorted by the fluid. Given so, investigation was carried out for both the case $k/\delta_k=0.24$ and $k/\delta_k=0.48$ till a downstream distance of 210 mm measured from the trailing vertex of the riblet.

From the smoke visualization results, the initial disturbance, at the station $x=10$ mm, as can

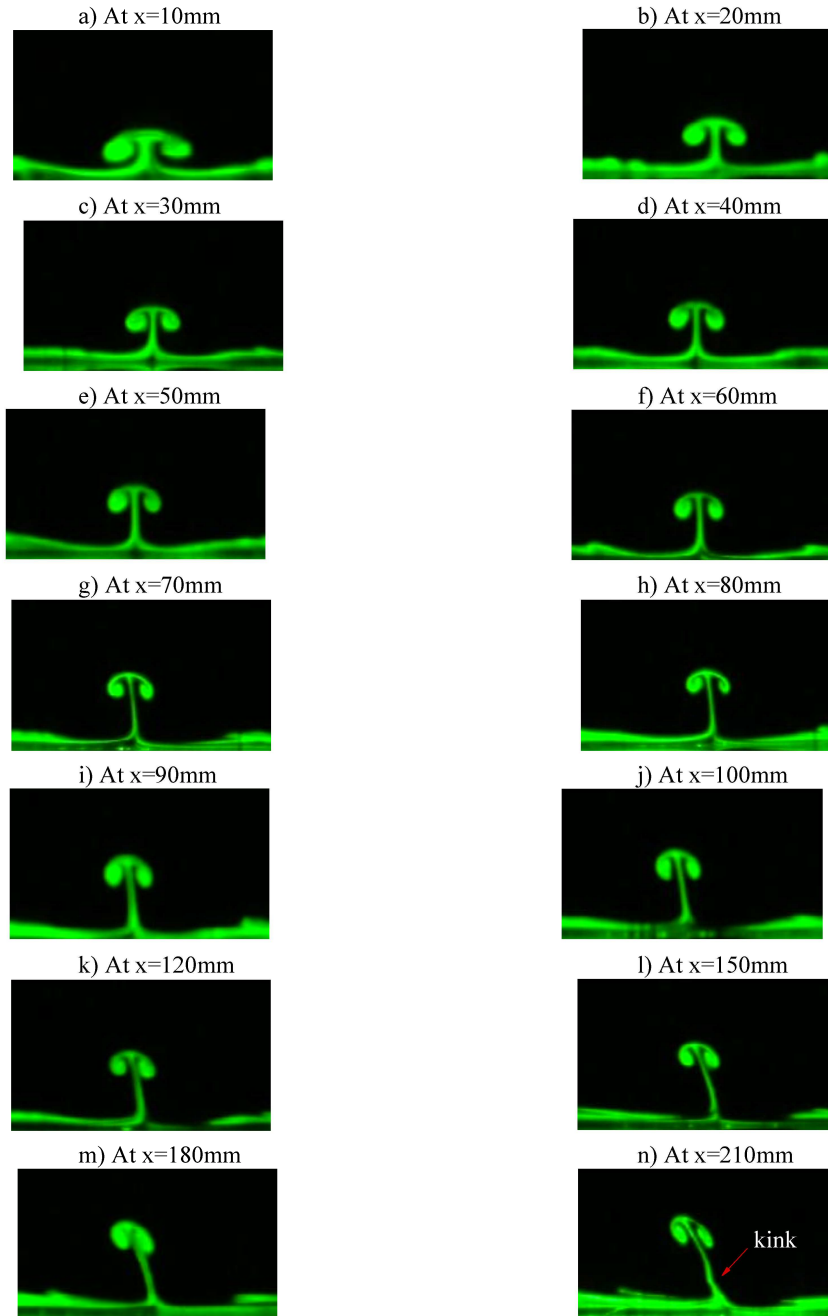


Figure 4.1: End on view of the cross-plane visualization of case $k/\delta_k=0.24$. The flow is out of page. Origin at the trailing vertex of the riblet.

be seen from figure 4.1 and 4.2, is a pair of stationary streamwise counter-rotating vortices. In the case of $k/\delta_k=0.24$, the streamwise vortices are found to extend throughout the region of investigation ($x=210$ mm from the trailing edge of the riblet) with a gradual growth. The kink,

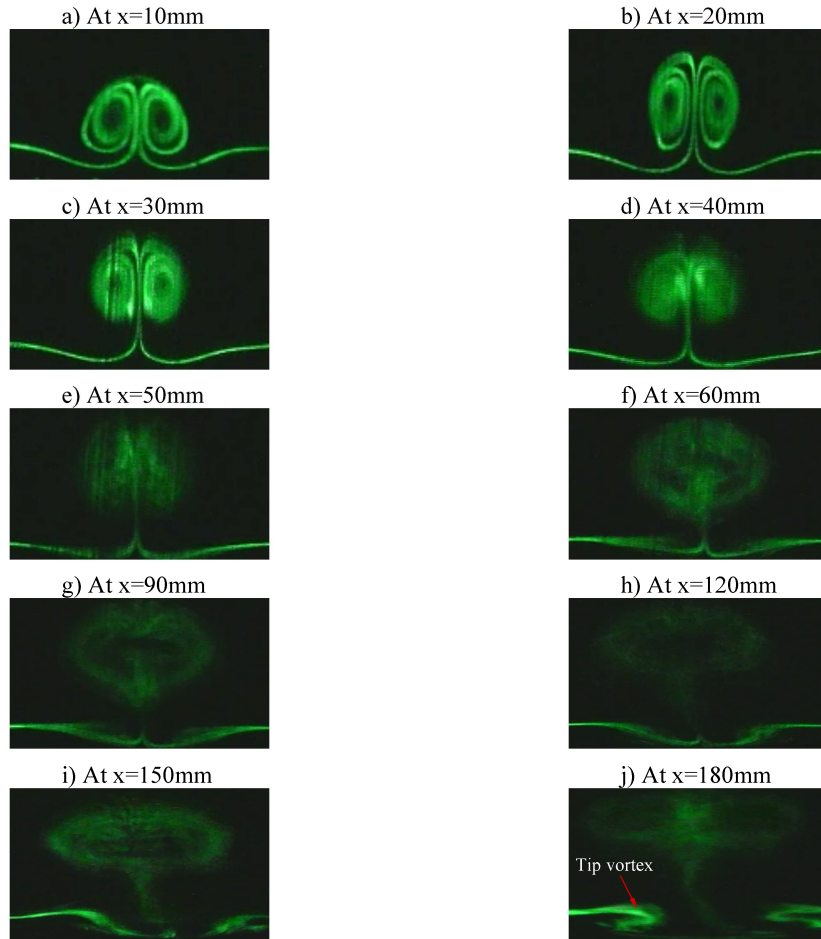


Figure 4.2: End on view of the cross-plane visualization of case $k/\delta_k=0.48$ ($k=3$ mm). The flow is out of page. Origin at the trailing vertex of the riblet.

that is found to occur in the stem of the vortex pair at around $x=210$ mm, is suspected to have occurred due to sinuous instability that sets in along the downstream (further discussed in detail in the forthcoming sections). In the case of $k/\delta_k=0.48$, the vortices diffuse at $x=30$ mm from the downstream of the riblet. Around $x=150$ mm, the tip vortices appear in the field of view of the smoke-wire.

The most important feature that is to be noticed to put forth a conjecture on the initiation of the counter-rotating vortex pair is the occurrence of the tip vortices with the increasing height of the riblet. The conjecture of flow kinematics using vortex line dynamics has been thus devised with the aid of smoke visualization to sustain that the initiation of the vortices behind the riblet is due to the concentration of the vorticity that arises due to the flow separation subjected to the adverse base pressure gradient on the leeward side. The free shear layer emanating from the

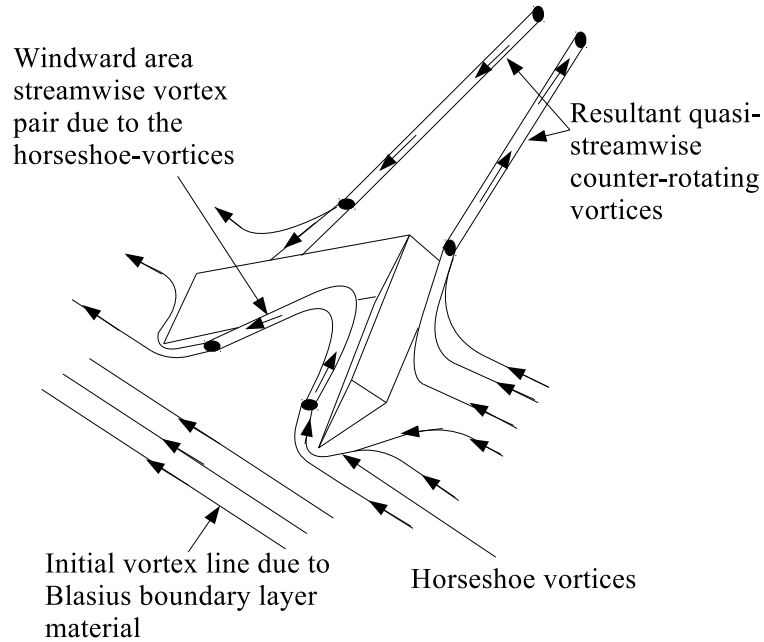


Figure 4.3: Schematic of the conjecture of flow kinematics.

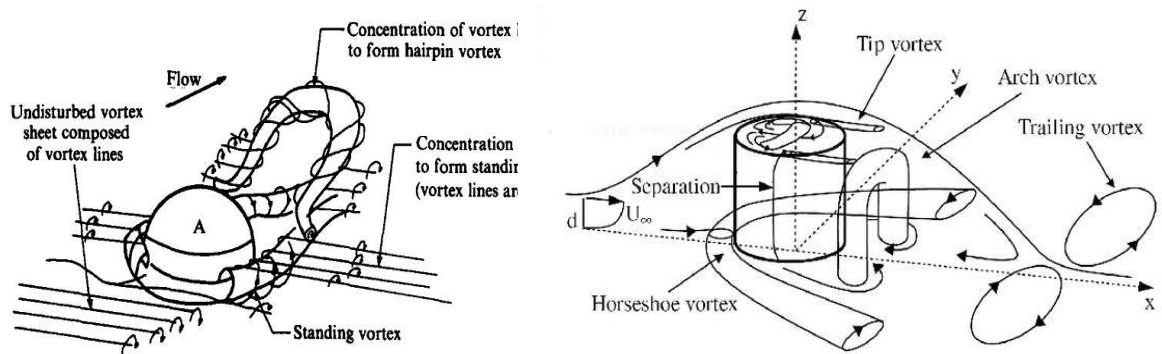


Figure 4.4: Left: Flow kinematics of hemispherical protuberance from Acarlar and Smith (1987). Right: Flow kinematics of cylindrical protuberance from Pattenden et al. (2005)

sharp edge S of the riblet could in this manner concentrate the vorticity that tends the fluid to roll up as vortices with distinct vortex core. The cross-stream pressure gradient imparted by the angle of the convergent riblet convects the vortices along the leeward surface of the riblet and leaves the surface tangentially. The interaction of the vortices (counter-rotating) leaving from the

either arms of the riblet later orient the organization along the downstream direction to result in a stationary quasi-streamwise counter-rotating vortex. As portrayed in figure 4.3 the resultant structure is a pair of vortex tubes of opposite sense convected along the downstream. Inside the boundary layer, these vortices stretch due to the mean shear which enhances the streamwise vorticity. Alongside stretching, the counter-rotating vortex pair - henceforth referred to as main vortices - lifts up along the downstream due to the mutually induced velocity. In addition to the main vortices, the impinging boundary fluid forked by the leading edge of the triangular base (T) can impart horseshoe vortices both on the windward side and lee side due to the skew-induced vorticity that results from the lateral deflection of the streamlines. If such is the case, there should arise a streamwise counter rotating vortices (due to two arms of the riblet) within the windward enclosed area A_w of the riblet. However, the occurrence of the horseshoe vortices depends upon the particular angle with which the flow encounters the riblet and more importantly the ratio of height of the riblet to the boundary layer thickness. Despite the possibility of occurrence of the horseshoe vortices, at the downstream of the riblet, this vortex pair emanating from the windward area should merge with the vortex pair from the leeward side as their sense of rotation is similar and should culminate in just a pair of vortex tubes. The vorticity vectors on the surface of the vortex tubes, thus, could supposedly be imagined to be aligned in $x - y$ plane as shown in figure 4.3. On the basis of hot wire measurements, we will show that the horseshoe vortices are weak and have no contribution to the flow phenomenon for low and moderate Re_k . But at higher Re_k , the occurrence of the horseshoe vortices becomes inevitable. The cross section of the riblet was chosen to be an isosceles triangle in order to hinder the extent of the two-dimensional separation behind the riblet and possibly the shedding of the vortices analogous to Gaussian-like geometries.

The flow kinematics of a convergent riblet is different from that observed in a hemispherical and cylindrical protuberance as shown in figure 4.4. In the former, the horseshoe vortices formed in front of the cylindrical obstruction convect and further evolve into streamwise structures. The interaction of the vortices with the wall lifts up spires of low momentum fluid which later break down to form hairpin vortices (Doligalski et al., 1994). However, in a hemispherical protuberance, alongside horseshoe vortices, the hairpin vortices are ejected from the surface of

the hemisphere due to the imbalance between centrifugal and normal pressure gradient forces (Acarlar and Smith, 1987).

4.2.1 Initial Disturbances

Given the flow kinematics subjected to convergent riblet, one either expects the diffusion of the vorticity in the downstream of the riblet and subsequently the flow relaxing to Blasius flow or expects the vortices to stretch along downstream further incurring secondary instability, either of which is dependent on the parameter circulation. But, in the arena of hot-wire anemometry, the measurement of circulation narrows down to the resolution of the hot-wire probe (Hamilton and Abernathy, 1991). Hence the characteristics of the initial disturbances are here chosen to be described with respect to the concentration of the turbulence intensity (Tu) as shown in figure 4.5.

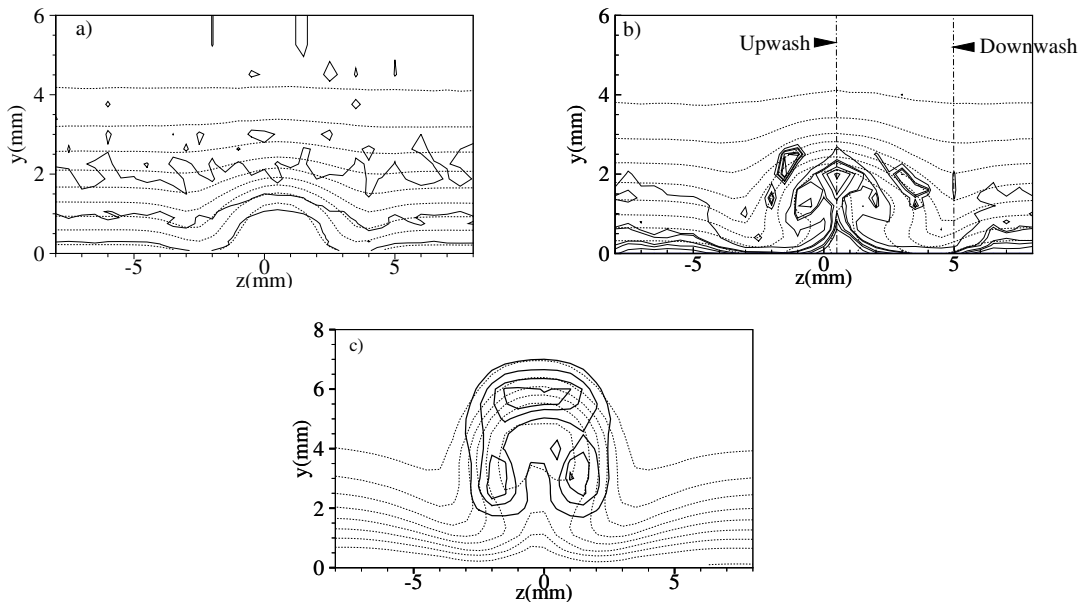


Figure 4.5: Characteristics of initial disturbance; a) $k/\delta_k=0.16$, b) $k/\delta_k=0.24$, c) $k/\delta_k=0.48$. Solid lines -Isolines of turbulence intensity; Dashed lines - Isolines of streamwise component of velocity (u/U_∞).

The location of the initial disturbance was fixed as 10 mm downstream from the trailing vertex (V) of the riblet. Given the Gaussian-like cross section of the convergent riblet, the two-dimensional separation behind the riblet was found to be well within 10 mm for the range of roughness Reynolds numbers considered here. From figure 4.5, for $k/\delta_k=0.16$, the disturbances

are more concentrated close to the wall. The contours of Tu are similar to that of the velocity contours. For $k/\delta_k=0.24$, the velocity and Tu contours are similar to k/δ_k near the wall, however a distinct region of concentration is seen to distributed symmetrically to the upwash. In the case of $k/\delta_k=0.48$, the Tu concentrations shows the manifestation of varicose modes. This is due to the interaction of the uplifted low momentum fluid with the outer high momentum fluid. The initial disturbances in all these cases are considered to be sub-optimal within the framework of transient growth.

The corresponding normal distribution of the amplitude of the spanwise harmonic modes associated with the initial disturbances is shown in figure 4.6. Visual inspection of the velocity contour shows that the velocity profile is spanwise symmetric and hence the harmonic modes contains only the cosine component. Thus the amplitude of the harmonic modes is calculated from the following expression,

$$a_n = \frac{2}{\lambda_m} \int_{-\frac{\lambda_m}{2}}^{\frac{\lambda_m}{2}} u(x_0, y_0, z) \cos(n\alpha z) dz \quad (4.1)$$

where, $\alpha=2\pi/\lambda_m$ is the dimensional wavelength parameter, a_n is the Fourier coefficient which corresponds to amplitude of the disturbance modes, and $n=1,2,..$ is the spanwise harmonic mode. λ_m is the wavelength which is the spanwise distance of the inflected region of the velocity contour.

From figure 4.6, for all heights of surface roughness, it can be seen that the amplitude of the first harmonic mode is found to be the most dominant mode. Considering the other modes, in $k/\delta_k=0.16$, the 2nd mode takes an S-shape, while the 3rd mode starts appearing. The 4th and 5th mode stays dormant. In $k/\delta_k=0.24$, the 2nd mode takes a more pronounced S-shape compared to $k/\delta_k=0.16$, while the 3rd and 4th mode follow a similar trend but out-of-phase and the 5th mode starts appearing. Other than the 4th and 5th modes, $k/\delta_k=0.16$ and $k/\delta_k=0.24$ could be well linked in a way that the amplitudes of $k/\delta_k=0.24$ are multiples of $k/\delta_k=0.16$. However, $k/\delta_k=0.48$ exhibits an entirely different scenario. The 1st harmonic mode has double peak with opposite signs. The S-shaped double peak initiates at 2nd mode, well pronounced at the 3rd and 4th mode and mildly defined in 5th mode. It should be noted that the double peaks of the 3rd and 4th mode shares the same wall-normal position. Also, it could be noticed that, with the increasing

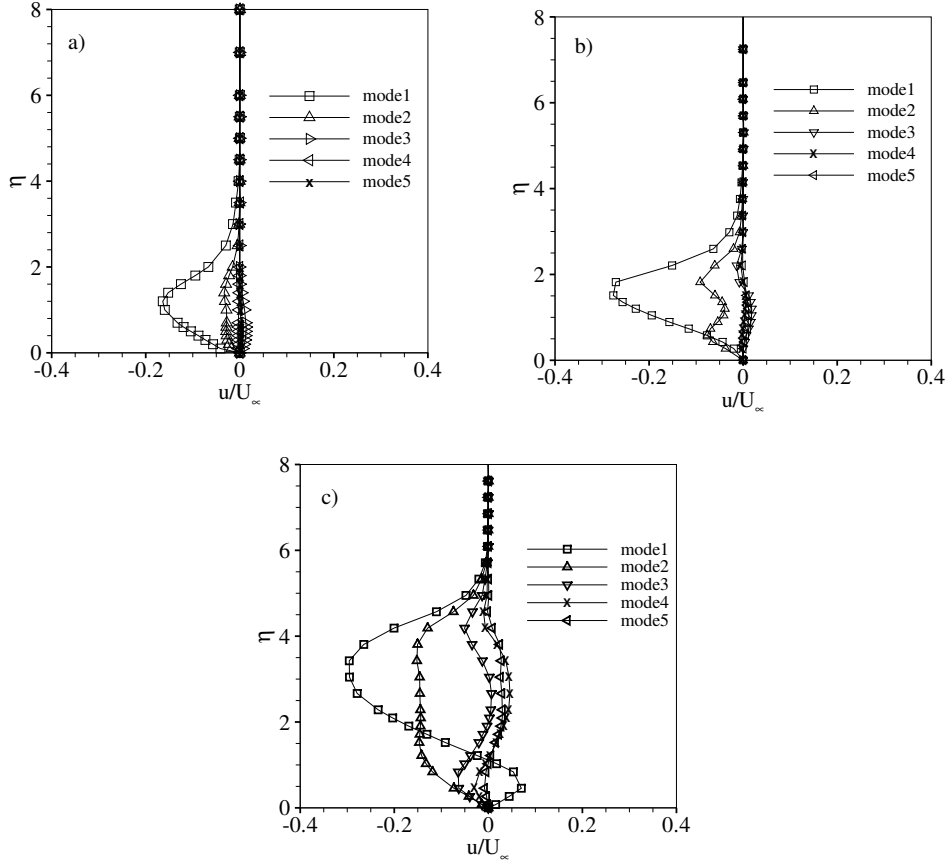


Figure 4.6: Normal distribution of amplitude of spanwise harmonic modes: a) $k/\delta_k=0.16$, b) $k/\delta_k=0.24$, c) $k/\delta_k=0.48$.

height of the surface roughness, alongside the occurrence of inflection, the maximum peak shifts away from the wall. This shows that the increasing height of the surface roughness necessitates the inclusion of higher modes to describe the resultant initial disturbance velocity field rather than a single most dominant mode. The most dominant mode could be related to the occurrence of the maximum disturbance amplitude as shown in figure 4.7. Following Winoto and Crane (1980), Bottaro and Klingmann (2002) the maximum disturbance amplitude, κ is determined as:

$$\kappa = \frac{u_d(\eta) - u_u(\eta)}{2U_\infty} \quad (4.2)$$

where u_d is velocity at downwash and u_u is velocity at upwash.

Clearly the position of the peaks of the amplitudes of the most dominant mode coincides with the amplitude of the maximum disturbance. As a precursor of a faint idea of how these initial

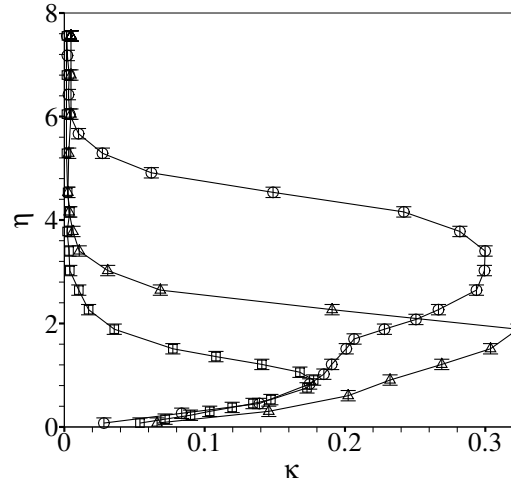


Figure 4.7: Normal distribution of disturbance amplitude. \square - $k/\delta_k=0.16$, \triangle - $k/\delta_k=0.24$, \circ - $k/\delta_k=0.48$.

disturbances might evolve can be related to the velocity profiles of low speed streak at upwash as shown in figure 4.8. In the case of $k/\delta_k=0.16$, the inflectional velocity profile is similar to that of the low speed streaks as considered by Asai et al. (2002)). He considered disturbances initiated by a wire gauze trip which induces a hairpin vortices along the downstream. Such an inflectional velocity profile which is hyperbolic-tangent function of the wall-normal co-ordinates exists to be laminar along the downstream without forcing additional disturbances. In the case of $k/\delta_k=0.24$, the inflection point moves away from the wall. However, the streak half-value width which is 4 mm and 5.5 mm for k/δ_k and $k/\delta_k=0.24$ respectively are in contrast to 6.5 mm in Asai's experiments. In $k/\delta_k=0.48$, the particular characteristic of the inflectional upwash velocity profile wherein the low momentum fluid rides over the high momentum fluid is quite similar to that exhibited by the hairpin vortices in the final stages of transition in Gortler instability (Swearingen and Blackwelder (1987)). However, the concentrations of turbulence intensity in figure 4.5 are not coherent with that of the sinuous modes that occur in the presence of hairpin vortices. One could possibly expect that the vortices induced in case $k/\delta_k=0.48$ is already at the verge of breakdown. The breakdown however in this case should come about by vorticity diffusion rather than a modal growth. It should be mentioned that in all these cases, the initiated disturbances are within the boundary layer.

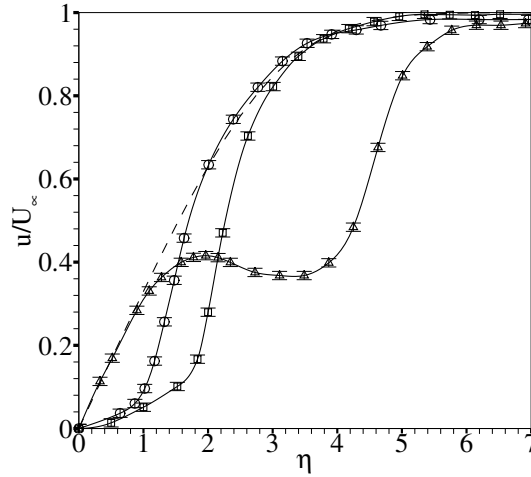


Figure 4.8: Wall-normal distribution of the mean velocity of low speed streak (upwash): - - - Blasius solution, \circ - $k/\delta_k=0.16$, \square - $k/\delta_k=0.24$, \triangle - $k/\delta_k=0.48$.

4.2.2 Evolution of Disturbances

Strictly speaking, given the initial disturbances, their spatial evolution should be brought about by observing the manifestation of spanwise harmonic modes along the downstream direction. However, in the case of an isolated surface roughness where the longitudinal vorticity extends to the ambient Blasius flow, extracting the modes is almost impossible as the spanwise wavelength of the disturbances is not fixed. An alternative way to quantify this is by looking into evolution of U'_{rms} , as shown in figure 4.9, which is the spanwise root-mean-square (rms) of the spanwise spatial disturbance ($U'=u(z)$ - spanwise average of $u(z)$) as defined in White (2002).

In $k/\delta_k=0.16$, the total disturbance is found to increase for a short downstream from $x=10$ mm to $x=15$ mm and then subsides. This simple single peaked distribution is concurrent with the results of White (2002). The maximum disturbance is found to occur at $\eta=1.3$. On the other hand, in $k/\delta_k=0.24$ and $k/\delta_k=0.48$, the disturbances sustain throughout the area of investigation. The viscous decay acts quite fast in the downstream in $k/\delta_k=0.16$.

In the case of $k/\delta_k=0.24$ and $k/\delta_k=0.48$, the movement of the maximum disturbance peak which is regarded to be the function of wavelength (White 2002, White and Reshotko 2002) is supplemented by figure 4.10 that depicts the spanwise wavelength spectra of the corresponding wall location where the maximum disturbance peak occurs. The plots are the envelopes which

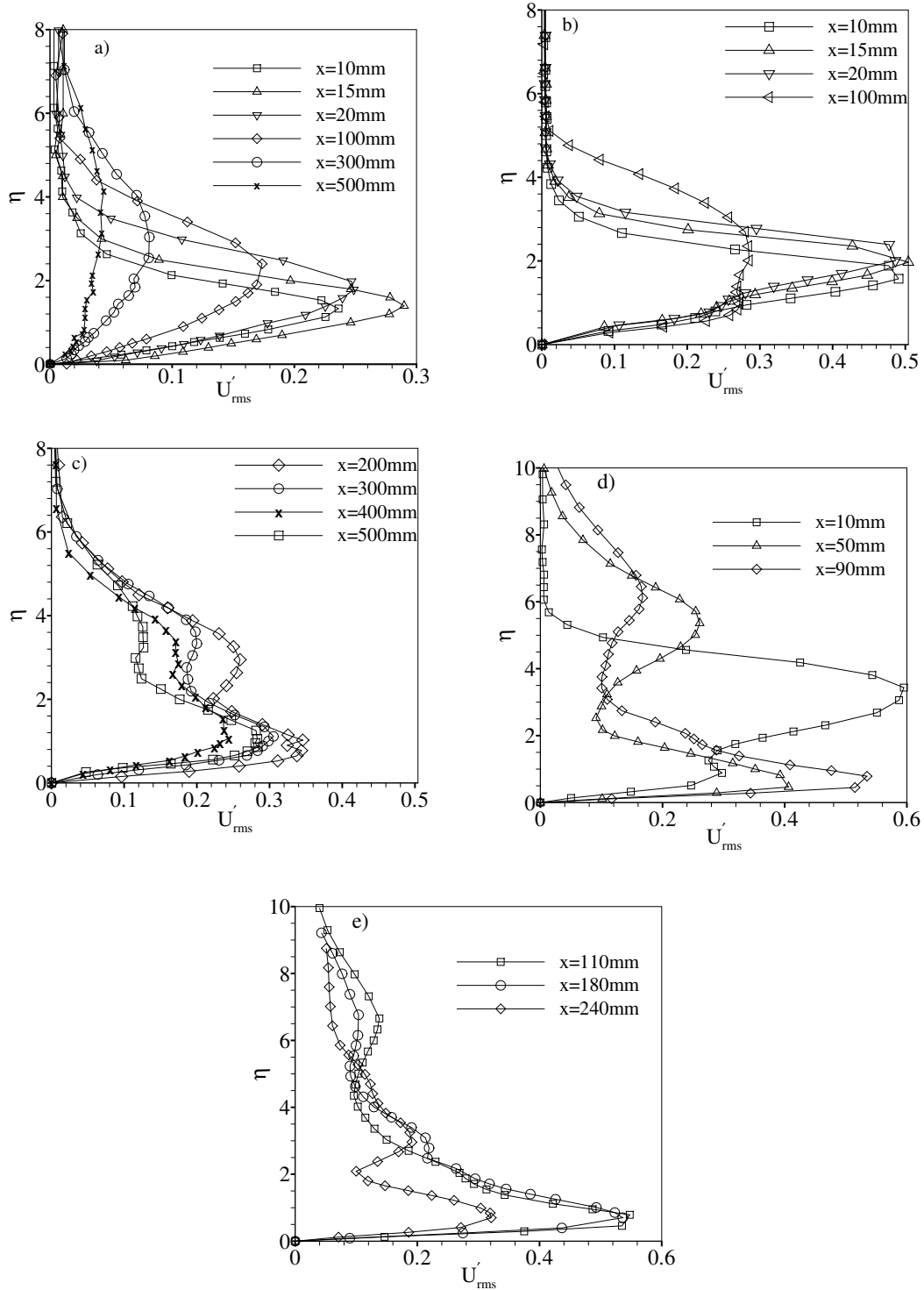


Figure 4.9: Total Disturbance profiles; a) $k/\delta_k=0.16$, b) and c) $k/\delta_k=0.24$, d) and e) $k/\delta_k=0.48$.

are formed by connecting the peaks, using linear interpolation, in the wavelength spectra. By doing so, the area under the curves still complies with the Parseval's identity (White and Ergin,

2003a). In all the three cases, the initial disturbance comprises three wavelengths - 8 mm, 10.6

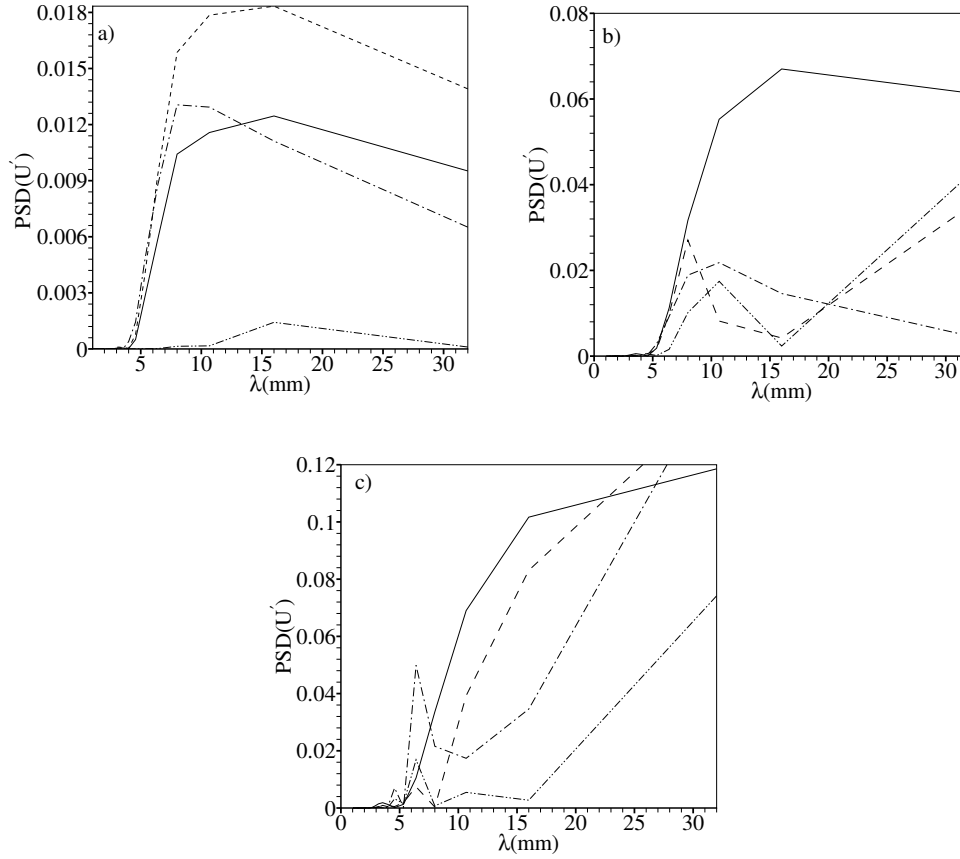


Figure 4.10: Spanwise wavelength power spectral density; a) $k/\delta_k=0.16$: - $x=10$ mm, - - $x=15$ mm, -.- $x=30$ mm, -.-.- $x=500$ mm; b) $k/\delta_k=0.24$: - $x=10$ mm, - - $x=100$ mm, -.- $x=300$ mm, -.-.- $x=500$ mm, c) $k/\delta_k=0.48$: - $x=10$ mm, - - $x=90$ mm, -.- $x=180$ mm, -.-.- $x=240$ mm. Note the variation of the ordinate.

mm and 16 mm. In all the cases, the most dominant wavelength is found to be 16 mm. Evidently, in $k/\delta_k=0.16$, the energy encompassed in wavelength increase at $x=15$ mm. Further downstream, the decay of the wavelengths 8 mm and 10.6 mm along the downstream is quicker than that of the longest wavelength which is in accordance with the results of White (2002). But in $k/\delta_k=0.24$ and $k/\delta_k=0.48$, the wavelength wherein the maximum disturbance energy nests in, shifts towards the shorter wavelength along the downstream. Relating the shifts of the maximum disturbance peaks to the wavelength spectra, it is definitive of the fact that disturbance peaks near the wall (in figure 4.9) corresponds to the maximum energy contained in the shorter wavelength while that away from the wall corresponds to the maximum energy contained in the longer wavelengths.

Also from figure 4.10, it could be noted that, in $k/\delta_k=0.48$, along the downstream, peaks of shorter wavelength appears to get accommodated in the spectra. Deeper insight into the manifestation of the shorter wavelength in the spectra could be obtained by studying the isosurface of $\partial u/\partial z$, as shown in figure 4.11. Considering the streamwise component of velocity to be

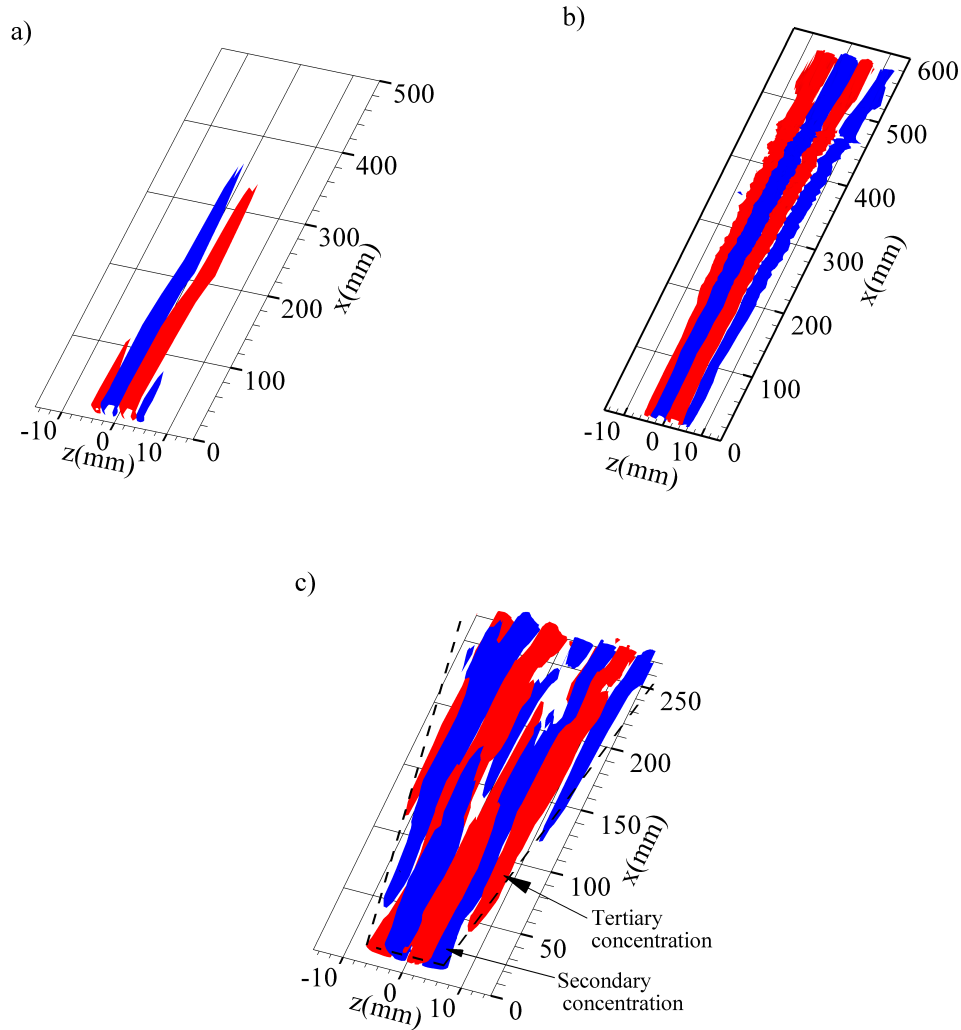


Figure 4.11: Iso-surface of $\partial u/\partial z$ (Red: $0.1 \times 10^{-3} \text{s}^{-1}$, Blue: $-0.1 \times 10^{-3} \text{s}^{-1}$; a) $k/\delta_k=0.16$, b) $k/\delta_k=0.24$ and c) $k/\delta_k=0.48$. Iso-surface volume was formed by interpolation of the data measured at 11 stations for $k/\delta_k=0.16$ and 0.48 , 67 stations for $k/\delta_k=0.24$.

dominant compared to the cross-stream components, $\partial u/\partial z$ could be considered to represent the

evolution of the streamwise vorticity in regards to the following equation.

$$\frac{D\omega_x}{Dt} = \omega_x \frac{\partial u}{\partial x} + \omega_y \frac{\partial u}{\partial y} + \omega_z \frac{\partial u}{\partial z} + \nu \nabla^2 \omega \quad (4.3)$$

where $\omega=(\omega_x,\omega_y,\omega_z)$ is vorticity vector and $\mathbf{u}=(u_x,u_y,u_z)$ is velocity vector. Although, the concentrations of $\partial u/\partial z$ do not necessarily represent vortex roll up. From figure 4.11, it could be seen that the concentration allegedly subsides just downstream of $x=300$ mm in $k/\delta_k=0.16$. In $k/\delta_k=0.24$, the concentrations extend throughout the region of investigation. The presence of wiggles between $x=200$ mm and 570 mm is the region of sinuous instability. In $k/\delta_k=0.48$, a wedge-like growth of the concentrations could be observed. The secondary concentrations in all the three cases arise due to the spanwise velocity gradient between the downwash region and the surrounding Blasius flow, while the tertiary concentrations that appear in $k/\delta_k=0.48$ are due to the tip vortices that arise from the triangular face of the riblet. The interaction of the tip vortices with the wall results in the spires of low momentum fluid that results in tertiary concentrations. This extension in the spanwise inflections of the velocity near the wall results in the increase in disturbance energy. This serves as an explanation as to why the maximum disturbance peak shifts towards the wall from $x=50$ mm to $x=90$ mm for $k/\delta_k=0.48$, and thereafter takes a constant location along the downstream in figure 4.9. Also figure 4.11 reflects the obvious fact that the highly inflected upwash velocity profile in $k/\delta_k=0.48$ leads to the breakdown of the streamwise vortices which occurs ahead of $x=150$ mm. Besides the near wall maximum peak in figure 4.9, a second peak appear around $x=200$ mm at $\eta=3.2$ in $k/\delta_k=0.24$ while it appears at $x=50$ mm, $\eta=5.6$ in $k/\delta_k=0.48$. The occurrence of the second peak though, is subjected to the secondary and tertiary concentrations, where comparatively higher energy in the near-wall-peak is due to the stronger streak amplitude compared to that in the outer boundary layer. Along the downstream, both the peaks in $k/\delta_k=0.24$ and $k/\delta_k=0.48$, subside. This could only collectively suggest that, with the increase in the height of the surface roughness the flow phenomenon disappears from the radar of transient growth. The evolution of the corresponding maximum streak amplitude (calculated using eqn. 4.2) is shown in figure 4.12. The trend of transient growth phenomenon for $k/\delta_k=0.16$ complies with an increase in the streak amplitude followed by its decay. In $k/\delta_k=0.24$, the streak amplitude experiences transient growth in the near downstream of the riblet and thereafter ex-

perience a gradual decay. This slow decay of the streak amplitude is a combinatorial effect of viscous diffusion in the boundary layer, interaction between the convecting vortex pair and the boundary layer and diffusion of vorticity of the vortex pair to the surrounding fluid. In $k/\delta_k=0.48$, the breakdown of the main vortices due to viscous diffusion is well reflected by a steep decrease in the maximum streak amplitude. Also, no transient growth regime is observed in the case of $k/\delta_k=0.48$.

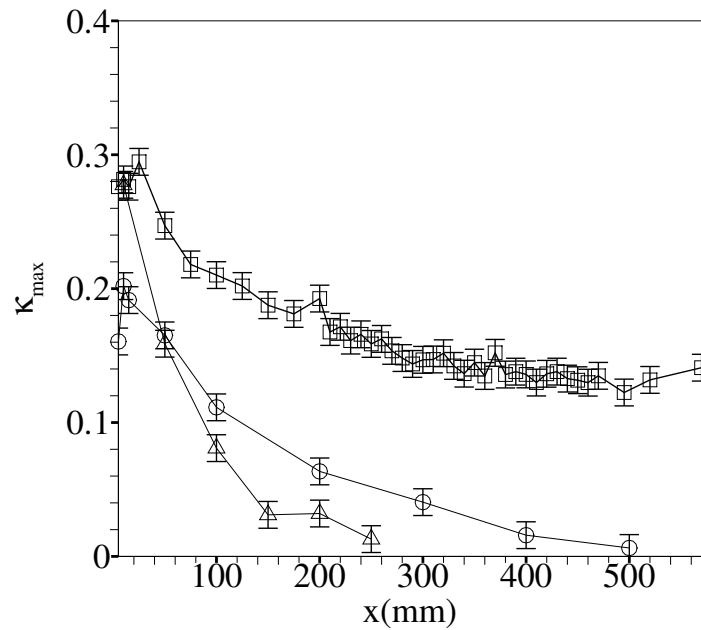


Figure 4.12: Evolution of maximum streak amplitude; \circ - $k/\delta_k=0.16$, \square - $k/\delta_k=0.24$, \triangle - $k/\delta_k=0.48$.

4.2.3 Streak Characteristics

Figure 4.13 shows the manifestation of the low-speed streaks for $k/\delta_k=0.16$. It is clearly seen that the vortex pair is embedded inside the Blasius boundary layer throughout the region of investigation due to the weak mutually-induced interaction. The vortex pair lifts at $x=15$ mm where the corresponding disturbance peaks in figure 4.9 takes the maximum value. This could be noticed from a less flat contours at $x=15$ mm compared to that at $x=10$ mm. These maximum disturbance contours tend to sustain few tens of millimeters downstream as could be seen at $x=30$ mm and later dies down along the downstream. For the case of vortex pair inside the boundary layer, the mean shear stretches the vortices along the downstream adding up to the

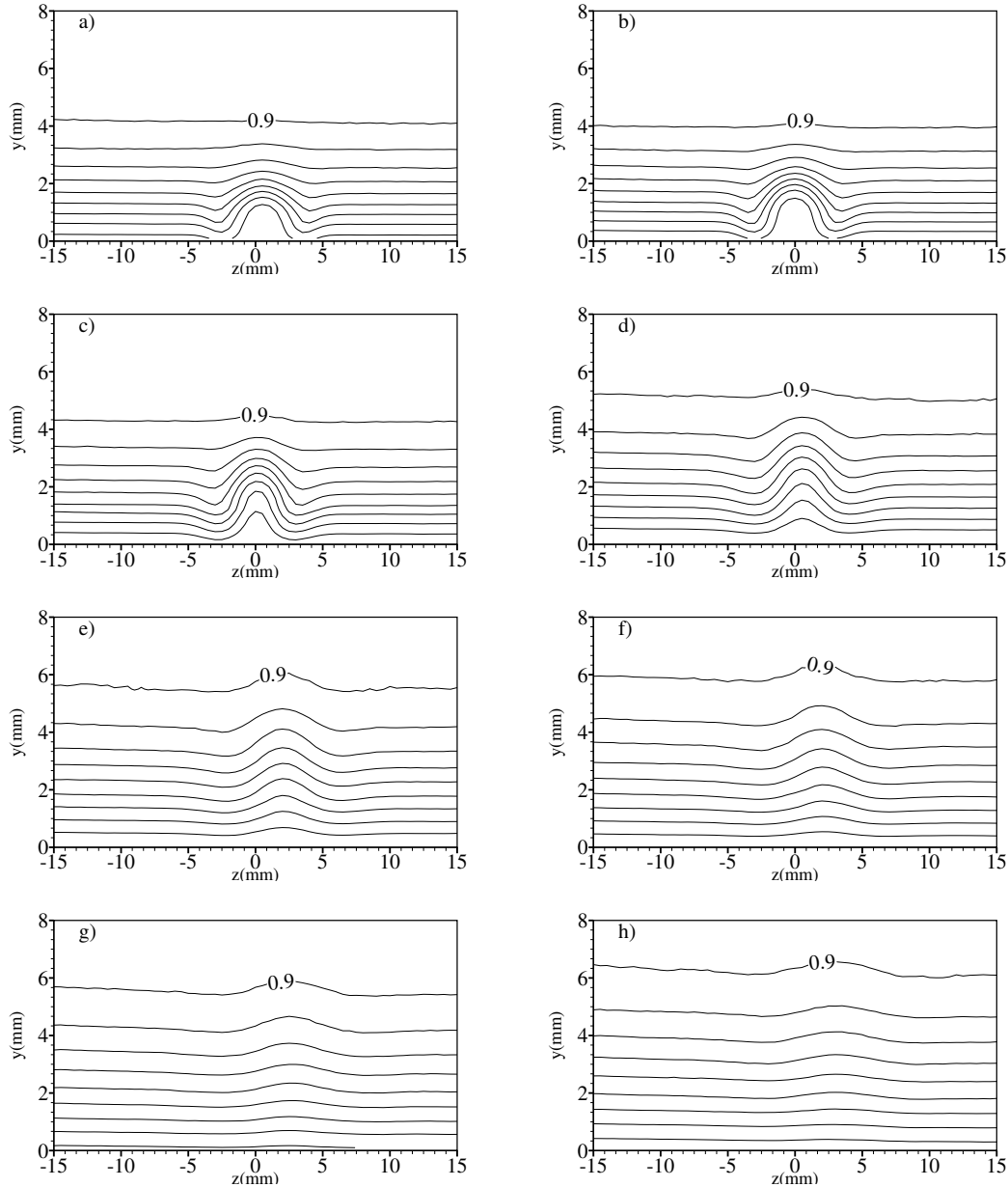


Figure 4.13: Iso- u/U_∞ contour at different cross-stream stations for $k/\delta_k=0.16$; a) $x=10$ mm, b) $x=15$ mm, c) $x=30$ mm, d) $x=100$ mm, e) $x=200$ mm, f) $x=300$ mm, g) $x=400$ mm, h) $x=500$ mm.

vorticity production (the first term of equation 4.3), which is also accompanied by the near wall viscous diffusion. The occurrence of the maximum growth is thus the balance between the vortex stretching and diffusion. Subsequently, it can be argued that with the increasing height of the roughness element the station at which the maximum growth occurs should be located further downstream. The inflection of the velocity contours shows no presence of horseshoe vortices

implying that the roughness Reynolds number and the angle of the riblet under consideration are not conducive for the formation of the horseshoe vortices - not only in the case of $k/\delta_k=0.16$ but also in $k/\delta_k=0.24$ (see figure 4.14). Also, from figure 4.13, it can be observed that the streaks gradually shift towards one side (upwash at $z=0$ between $x=10$ mm and $x=100$ mm and at $z=2.5$ mm from $x=200$ mm to $x=500$ mm). The spanwise component of velocity measurements earlier conducted by Tandiono et al. (2013) in the wind tunnel shows that the cross flow non-uniformities in the tunnel is less than 0.1%. Hence this drift is believed to be induced through amplification of minor free-stream or near-wall flow disturbances. Similar streak characteristics were observed in the Gortler instability experiments of Mitsudharmadi et al. (2004).

Similar dislocation of the streaks can be observed in figure 4.14 that shows the streak evolution along the downstream for $k/\delta_k=0.24$. In the case of $k/\delta_k=0.24$, from figure 4.14, it can be seen that the vortex pair, with strength greater than that of $k/\delta_k=0.16$, quickly increases the boundary layer thickness at the upwash along the downstream with corresponding downwash responsible for secondary $\partial u/\partial z$ concentrations. In this case, the mutually induced velocity drives the vortex pair outside the boundary layer which then gets convected by the free stream along the downstream. The faster convecting vortices in the free stream interacts with the boundary layer to lift up the low momentum fluid. The spanwise and wall normal inflections persist throughout the region of investigation. Further, from figure 4.15, it can be noticed that low speed streaks near the wall (around $y=1.6$ mm), that corresponds to the stem of the vortex pair, meanders between $x=200$ and 500 mm. The streak amplitude, $A_s=(u_d - u_u)/U_\infty$, at this wall normal position is found to be 0.4. With respect to the streak amplitude, the characteristics of this low speed streak is different from the streaks induced by hairpin vortices (Cherubini et al., 2013).

The plots of isolines of turbulence intensity (Tu) in figure 4.16 further showcase the development of instability modes. Given the concentration of Tu of initial disturbances at $x=10$ mm, its evolution to a fully developed varicose modes at $x=35$ mm is comprised of two distinct regions I and II. Region I occurs symmetrically on the either side of the upwash of the vortices while the concentrations at region II occurs due to the interaction of the low momentum fluid with the outer high momentum fluid. Along the downstream, between $x=35$ mm and 50 mm, Tu increases rapidly in both the regions I and II. Further downstream, between 50 and 65 mm, decrease in

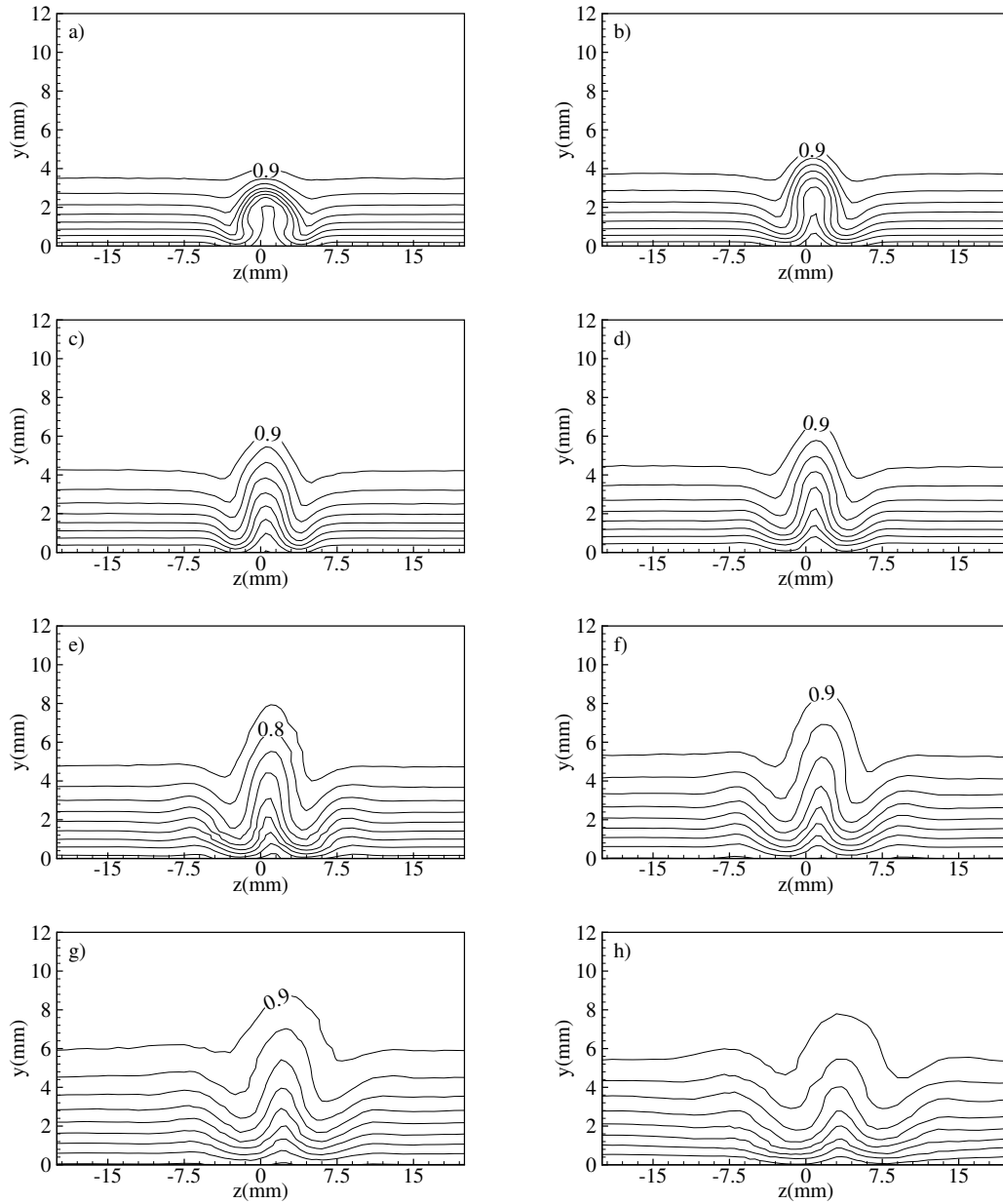


Figure 4.14: Iso- u/U_∞ contours at different cross stations for $k/\delta_k=0.16$; a) $x=10$ mm, b) $x=50$ mm, c) $x=100$ mm, d) $x=150$ mm, e) $x=200$ mm, f) $x=300$ mm, g) $x=400$ mm, h) $x=500$ mm.

Tu can be seen in both the regions. Following the decay of the varicose, between 65 and 200 mm, transition from varicose to sinuous mode can be seen with the complete breakdown of the varicose mode at $x=125$ mm. Thereafter, the sinuous modes leads the transitional boundary layer throughout the area of investigation. The concentrations are found to move towards the wall along the downstream. Basically, the occurrence of these modes is subjected to the wavelength

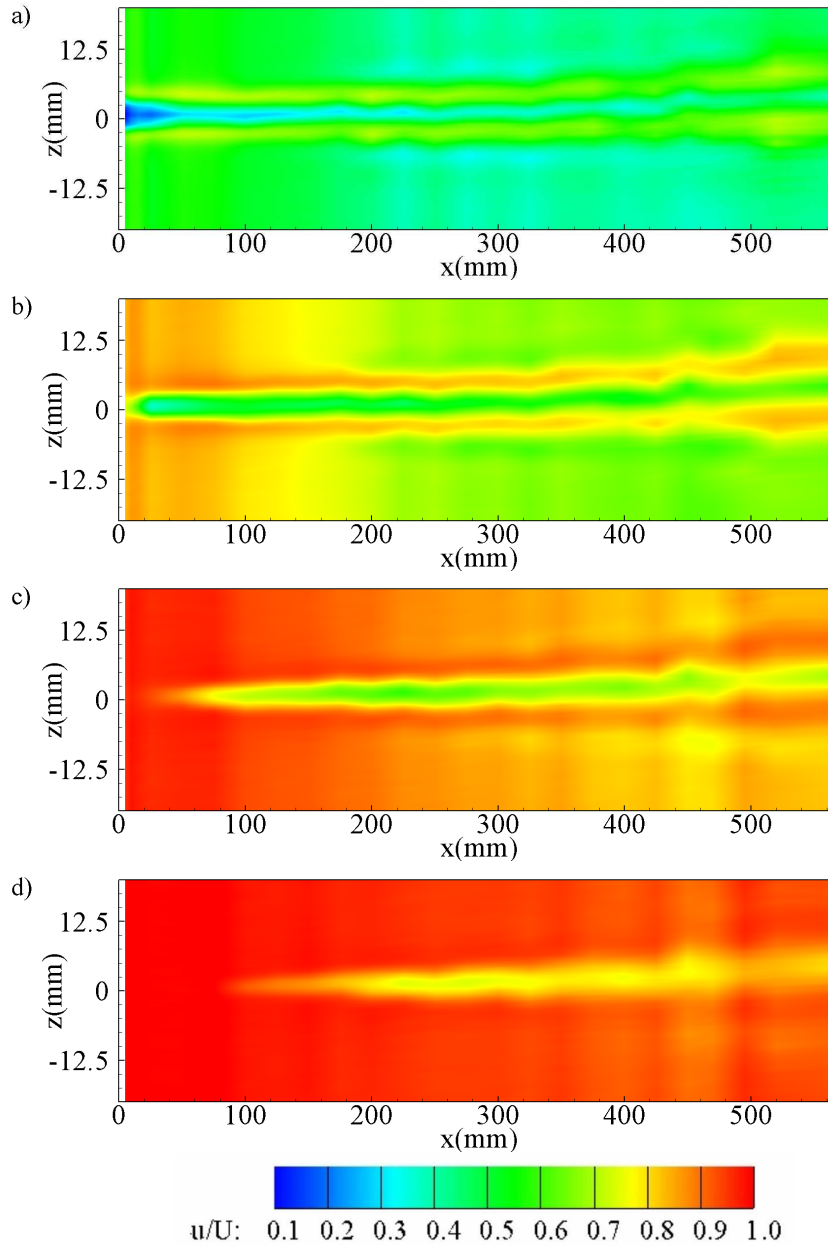


Figure 4.15: Iso- u/U_∞ contour for $k/\delta_k=0.24$ at a) $y/\delta_k=0.25$, b) $y/\delta_k=0.5$, c) $y/\delta_k=0.75$, d) $y/\delta_k=1$. Contours were formed by interpolation of measured data at 67 stations.

of the vortex pair (Chernoray et al., 2006). The streak half-width narrows down from 5.5 mm at $x=10$ mm to 3 mm at $x=200$ mm. The decreasing width is associated to the vortex pair moving out of the boundary layer due to the mutually induced velocity and narrowing down the spanwise inflection around uplifted low speed flow. The corresponding iso- $\partial u/\partial y$ and iso- $\partial u/\partial z$ contours are shown in figure 4.17.

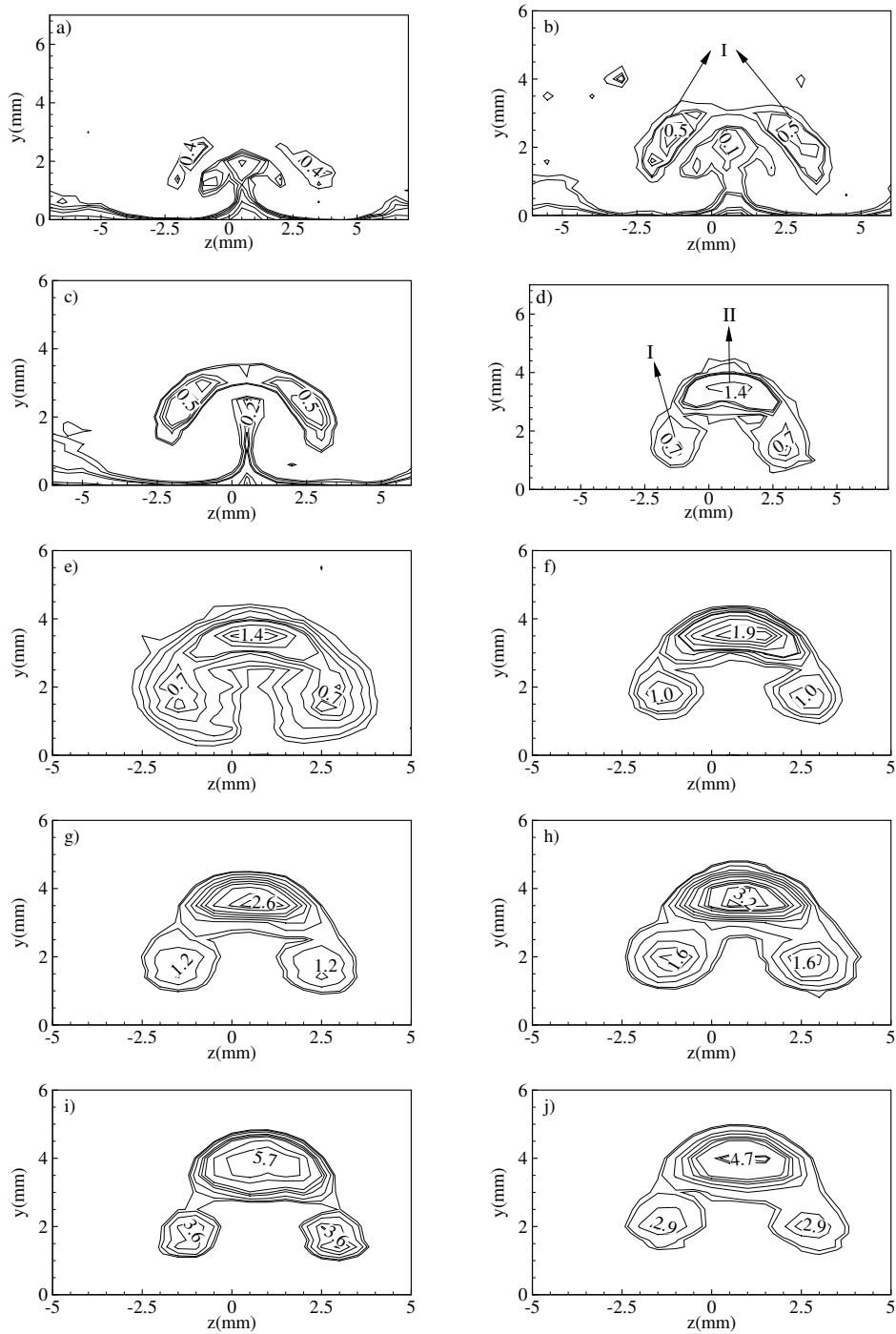


Figure: Caption see following page.

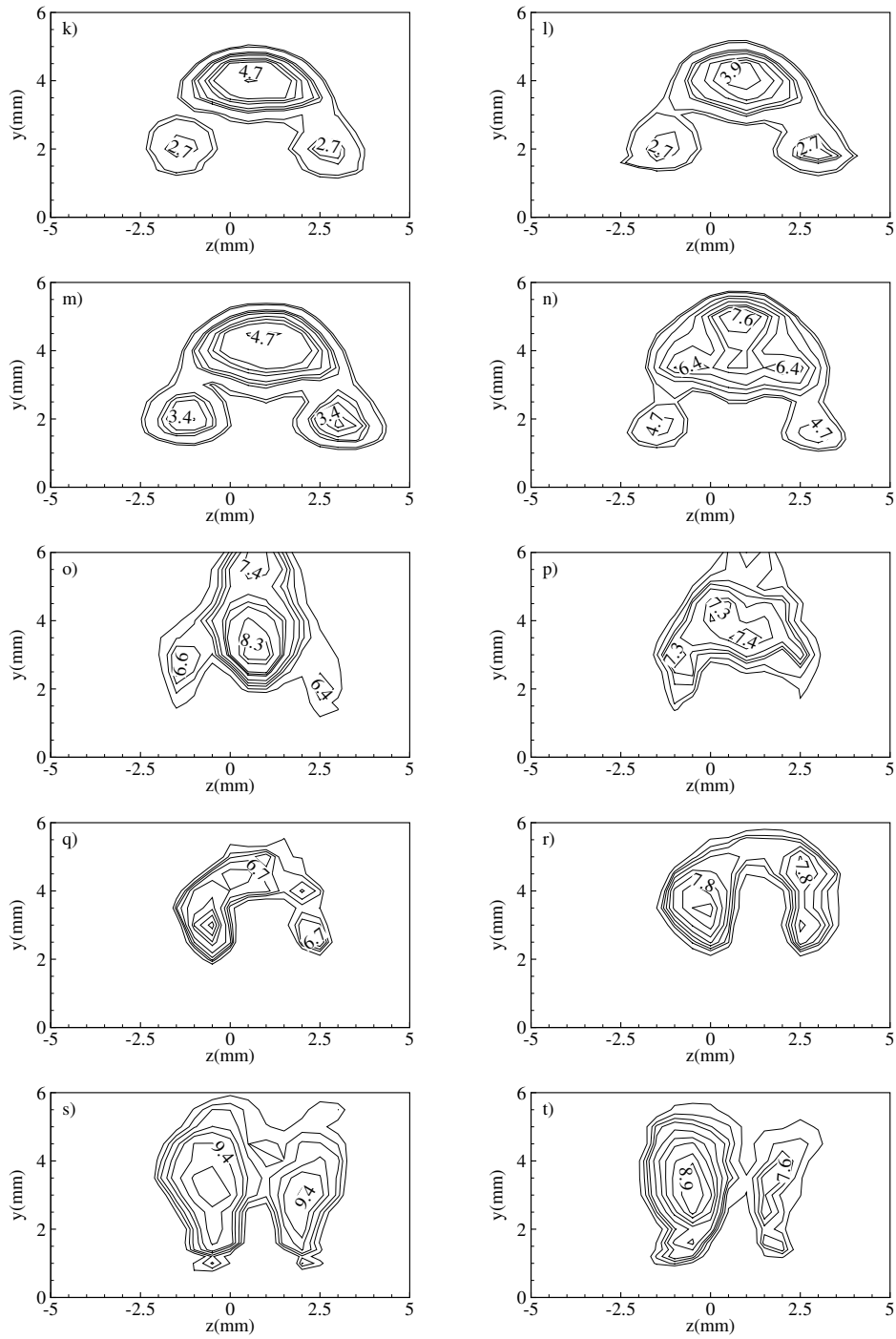


Figure: Caption see following page

The concentration of Tu which is found to be coherent with the $\partial u/\partial y$ contours at $x=50$ mm is a typical characteristic of the occurrence of varicose mode, while at $x=200$ mm where the concentrations of Tu are coherent with $\partial u/\partial z$ contours showcases the dominant sinuous modes.

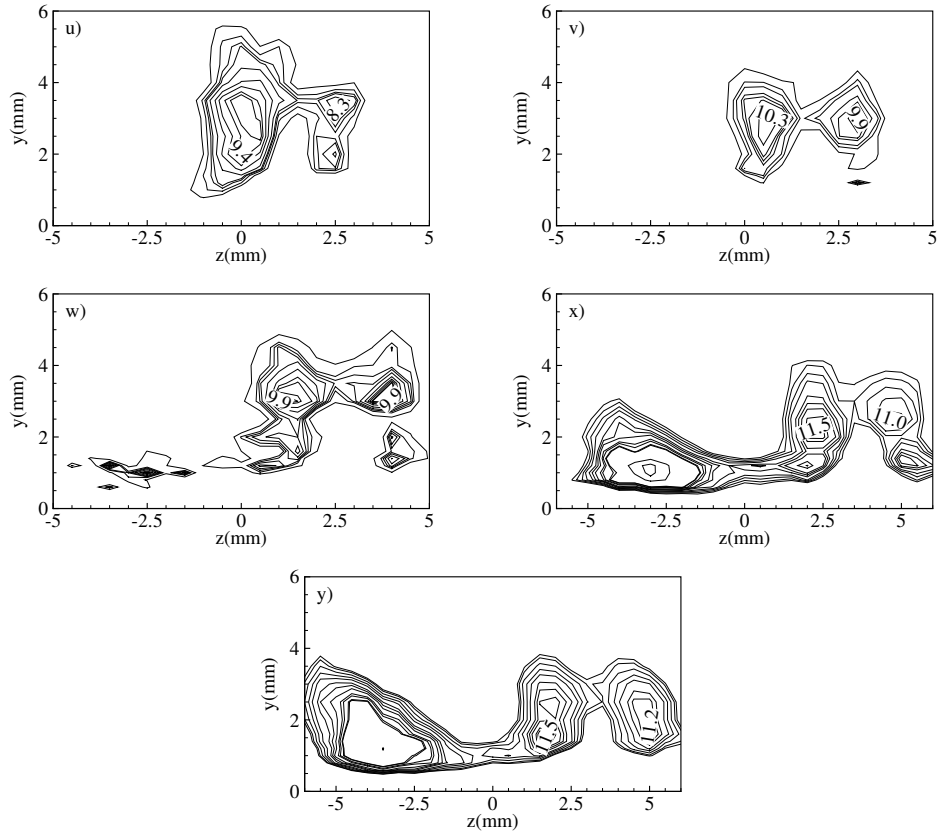


Figure 4.16: Evolution of Turbulence intensity concentrations for $k/\delta_\kappa=0.24$; a)x=10 mm, b)x=15 mm, c)x=20 mm, d)x=25 mm, e) x=30 mm, f)x=35 mm, g)x=40 mm, h)x= 45 mm, i)x=50 mm, j)x=55 mm, k)x=60 mm, l)x=65 mm, m)x=70 mm, n) x=75 mm, o)x=100 mm, p)x=125 mm, q)x=150 mm, r)x=175 mm, s)x=200 mm, t)x=250 mm, u)x=300 mm, v)x=350 mm, w)x=400 mm, x)x=450 mm, y)x=500 mm.

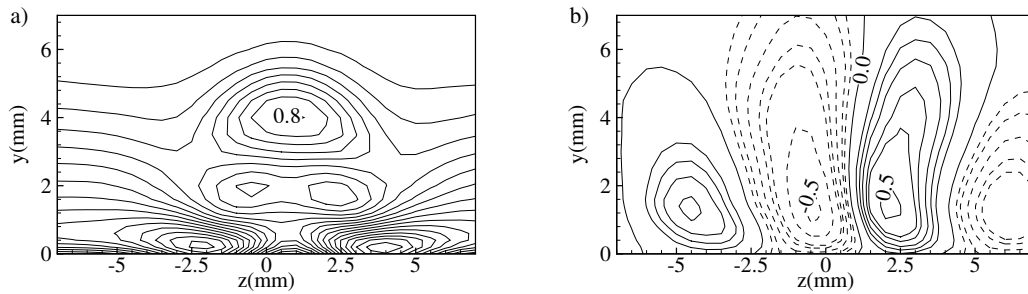


Figure 4.17: The isolines of a) $\partial u/\partial y$ at $x=50$ mm and b) $\partial u/\partial z$ at $x=200$ mm.

Figure 4.18 summarizes the growth and decay of the varicose mode and its transition to sinuous mode in terms of the maximum turbulence intensity (u_{rms}^m).

A deeper insight into the mechanism can be gained by taking a hasty glance at figure 4.19

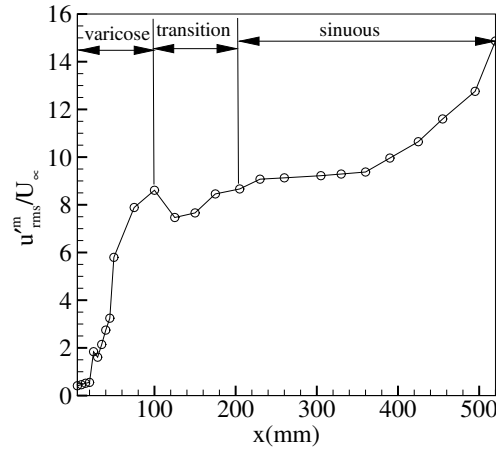


Figure 4.18: Growth of varicose and sinuous modes in terms of maximum turbulence intensity.

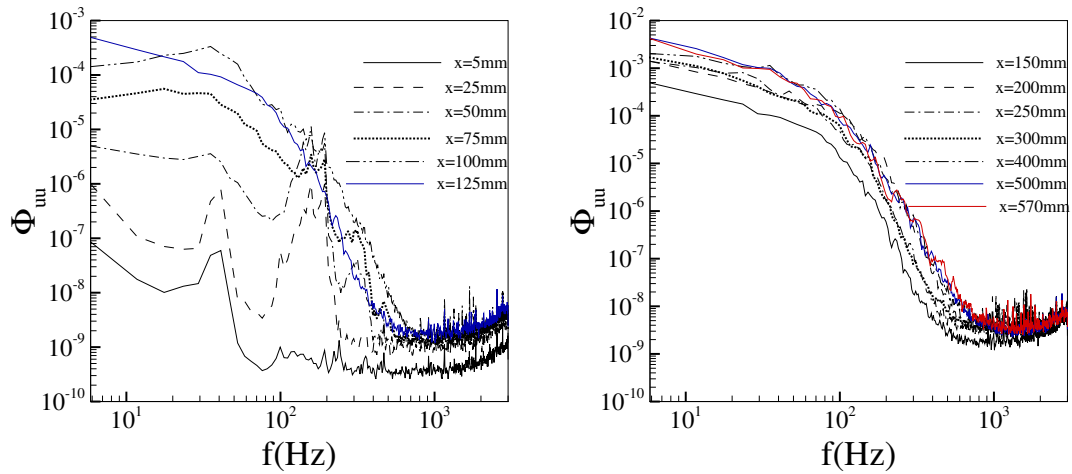


Figure 4.19: Power spectra of streamwise fluctuating velocity component at different streamwise stations.

that plots the power spectral density (ϕ_{uu}) of the streamwise fluctuating velocity at the point of maximum Tu . The power spectra was obtained by using Welch's power spectral estimate. The frequency peaks around 100 Hz at $x=25$ mm to 50 mm corresponds to the instability waves of the varicose modes. Further downstream, these frequencies subside and the total energy of the fluctuating velocity is found to be distributed in the low frequency bandwidth of the spectrum. The energy encompassed in the low frequency spectrum increases all the way downstream. This switch from varicose to sinuous mode is clearly different from that one would expect from the instability that arises from the occurrence of hairpin vortices. The notable scenarios in which

the evolution of the varicose mode culminates in, are: i) The appearance of the hairpin vortices that leads to train of vortices resulting in turbulent spots (Asai et al., 2002) and ii) as in Gortler instability problem, the co-existence of varicose mode and sinuous mode with the sinuous mode being the most dangerous. However, in the present case, the switch from varicose to sinuous mode implies that the diffusing stationary counter-rotating vortex pair hinders the formation of the hairpin vortices and the energy increase in the spectra is solely due to the growth of the sinuous mode that results in meandering. Unlike wake-like instability wherein the internal shear layer resulting from meandering leads to regeneration of the vortices by shear-induced vorticity (Schoppa and Hussain, 2002), the streak instability under investigation does not play any role in vortex regeneration. The argument comes obvious on examining the isosurface of $\partial u/\partial z$ in figure 4.11. Should there have been vortex regeneration, the interaction of the regenerated vortex with the wall would have resulted in tertiary concentrations of $\partial u/\partial z$.

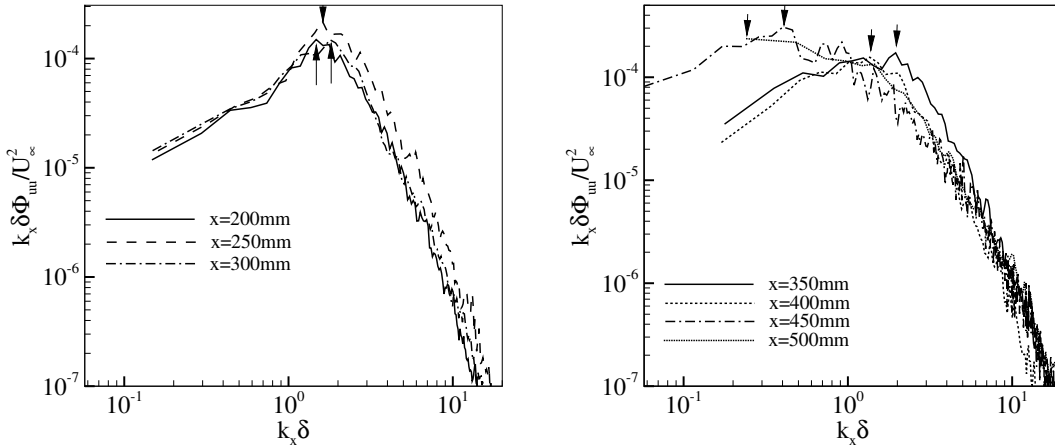


Figure 4.20: Non-dimensionalised premultiplied one-dimensional spectra obtained at the position of maximum Tu . Arrows indicate the peak.

Figure 4.20 plots the premultiplied one-dimensional wavenumber spectra ($k_x \delta \phi_{uu}/U_\infty^2$, where $k_x = 2\pi f/u(y)$ was obtained from Taylor's hypothesis) within the region of sinuous modes (between $x=200$ mm and 500 mm) at different streamwise stations. The arrow mark in the plot points the probable region of maximum energy (as the peak is smeared out due to the power spectral algorithm). The plateau in the wavenumber spectra occurs at around $k_x \delta = 1.5$ between $x=200$ and 350 mm. Downstream of $x=350$ mm, the peak shifts towards low wavenumber region of the

spectrum. A brief shift of the peak to $k_x \delta = 1.8$ can be observed between $x=300$ mm and 350 mm. Given that this variation might occur from the streak not being perfectly sinusoidal (Hutchins and Marusic, 2007), we do not tend to infer that the wavelength increases for a short span of the streamwise distance (between $x=300$ mm and 350 mm). However, figure 4.19 depicts that the energy within the sinuous mode region increases with the increase in streamwise distance. For a streak that is subjected to a single event, namely meandering, the energy increase would have been expected to result from the increased spatial oscillation of the streaks. Figure 4.20 and figure 4.19 combinedly suggests that the streak experiences an increased spatial oscillation with an increasing streamwise wavelength along the downstream.

In $k/\delta_k=0.48$, as shown in figure 4.21, the greater strength of the main vortices compared to $k/\delta_k=0.24$ diffuses faster at around $x=100$ mm. The development of the secondary upwash occurs at $x=50$ mm. Meandering of the secondary low speed streaks that extends throughout the area of investigation can be seen in figure 4.22. The amplitude of the meandering streaks (A_s) was found to be 0.3 at $y/\delta_k=0.25$.

Figure 4.23 shows the concentration of the sinuous modes of the secondary low speed streaks. The distorted concentrations are due to the tilting of the streaks. Considering the interaction of the tip vortices with the wall shear layer wherein the low momentum fluid is spewed out, the breakdown of the spewed low momentum fluid could result in a single cane or hairpin vortices (Bernard, 2012).

Table 4.2: Effect of Roughness Reynolds number. Frequencies measured at station $x=200$ mm in the upwash region of the main vortices at $y/\delta_k=0.25$.

$k(\text{mm})$	k/δ_k	$Re_k(uk/\nu)$	Dominant Frequency(Main vortices)	Harmonics
1	0.16	47	- (Transient growth)	-
1.3	0.2	83	- (Transient growth)	-
1.5	0.24	96	Low frequency oscillations(Instability)	-
1.8	0.28	150	Low frequency oscillations(Instability)	-
2	0.32	184	54.1HZ (Vortex breakdown)	108Hz, 218.1Hz
3	0.48	380	55.6Hz (Vortex breakdown)	111Hz, 222Hz

Table 4.2 summarizes the observed flow phenomenon with respect to Roughness Reynolds number. It is evident that the evolution of disturbances hops from transient growth to instability and later to vortex breakdown phenomenon by viscous diffusion. The comparison is made at

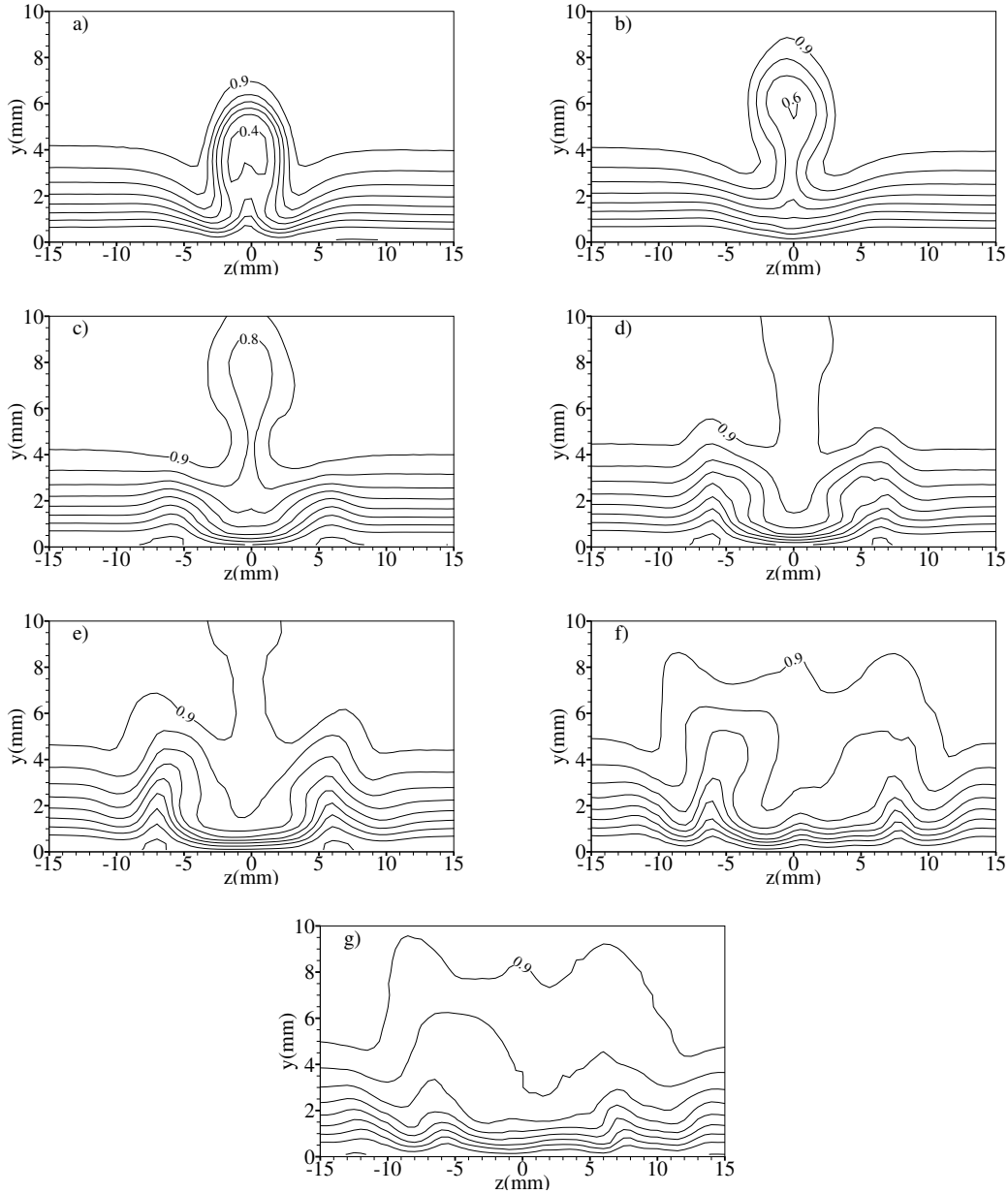


Figure 4.21: Iso- u/U_∞ contours for $k/\delta_k=0.48$; a) $x=10$ mm, b) $x=30$ mm, c) $x=50$ mm, d) $x=100$ mm, e) $x=150$ mm, f) $x=200$ mm, g) $x=250$ mm.

$x=200$ mm where the low frequency oscillations appear for the case $k/\delta_k=0.24$. For the low Reynolds number range (Re_k between 47 and 83) where the power spectrum doesn't exhibit any distinct peak depicts the transient growth phenomenon. The low frequency oscillations occurring between Re_k 90 and 154 denotes the instability zone. At large Re_k (≥ 184), the dominant high frequency and its harmonics appear. At this range, further increase in Reynolds number simply

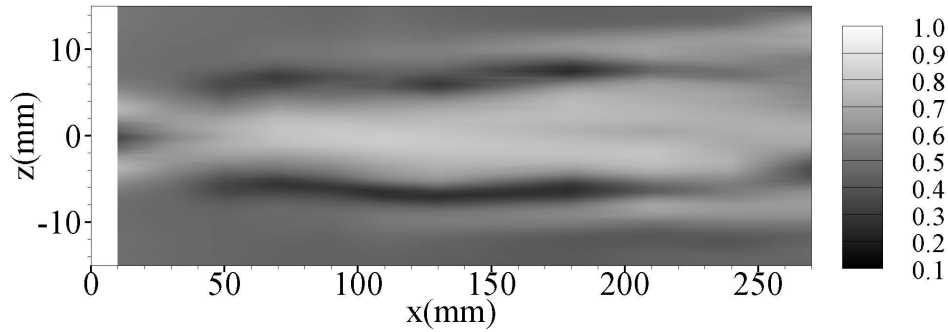


Figure 4.22: Iso- u/U_∞ contour for $k/\delta_k=0.48$ at $y/\delta_k=0.25$. Contour formed by interpolation of measured data at 11 stations.

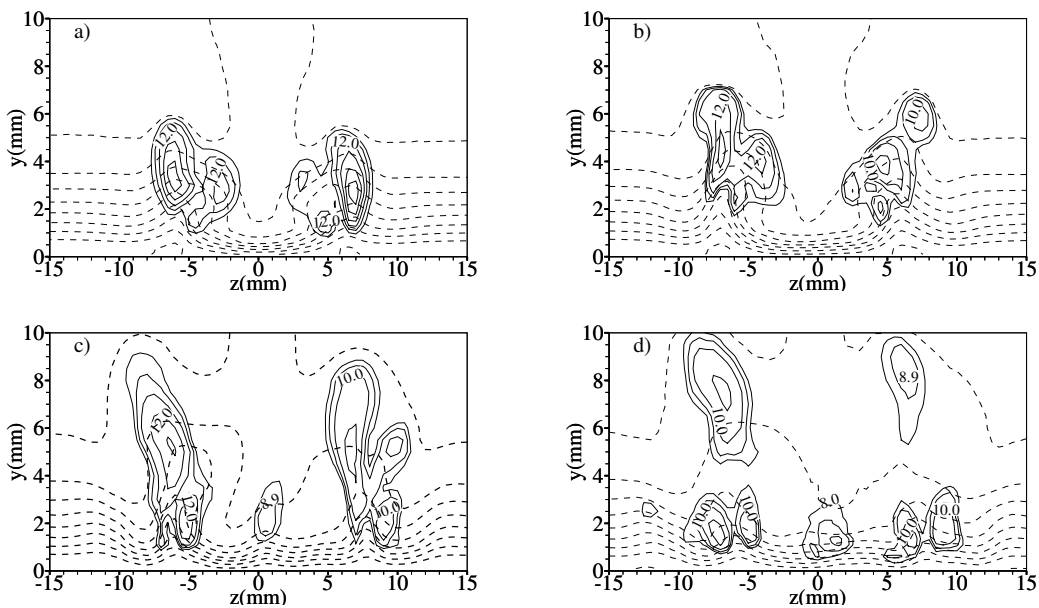


Figure 4.23: Evolution of Tu concentrations of the secondary streaks for $k/\delta_k=0.48$; a) $x=100$ mm, b) $x=150$ mm, c) $x=200$ mm, d) $x=250$ mm.

shifts the vortex breakdown to the upstream.

Table 4.3 compares various induced-disturbances with the present results. The important point to be noted is that the spectral peaks corresponding to the streamwise vortices and hairpin vortices falls on the high frequency spectrum compared to the low frequency oscillations of the present results.

Table 4.3: Comparison of roughness induced disturbances and its instability.

Authors	Method of forcing disturbances	Re_k	wavelength	Spectral Peaks	resultant flow structure
Backchinov et al(1992)	array of square ribs	740	10mm	125, 135, 165	Streamwise vortices incurring instability
Mastubara and Alfredson (2002)	Grid generated turbulence		100 mm		hairpin vortices as secondary instability
Asai et al (2002)	Mesh wire gauze and loudspeakers	480	7.5 and 5.5 mm	100 Hz	hairpin vortices as secondary instability
Cherubini (2013)	hemispherical bump	235 and 300	12 mm		hairpin vortex incurring secondary instability
Present	Convergent riblet	96	9 mm	low frequency oscillations	switch from varicose to sinuous instability

4.3 Concluding remarks

In this chapter, the influence of an isolated directional dependent surface roughness, namely convergent riblet, in Blasius boundary layer has been investigated experimentally using a single probe hot-wire anemometer. The study leaves us with the following takeaway points.

i) The evolution of disturbance initiated by the convergent riblet leads to a pair of streamwise counter-rotating vortices emerging at the wake of the riblet convected along the downstream.

ii) In the low roughness Reynolds number range ($47 < Re_k < 83$), the vortex pair that stay within the boundary layer undergoes transient growth phenomenon subjected to the balance between vortex stretching and vortex diffusion.

iii) In the moderate Roughness Reynolds number range ($90 < Re_k < 154$), the streaks induced by the vortex pair experiences instability. The growth of the instability modes incurs 3 stages - Growth of varicose mode, its decay and transition to sinuous modes. The varicose modes grows faster than the sinuous modes. Within the region of sinuous modes, the energy due to meandering of the streaks is distributed in the low frequency bandwidth. Along the downstream, the energy encompassed in this low frequency bandwidth increases with the increased spatial oscillation of the streaks. The streamwise wavenumber associated with the streak meandering is found to decrease along the downstream. From the inception of the sinuous instability, the meandering of the streaks extends to about 400 mm.

iv) Following the instability, breakdown of the streamwise vortices through viscous diffusion occurs for larger Reynolds number ($Re_k > 154$).

Chapter 5

Instability of forced wavelength disturbances

5.1 Introduction

As concluded in Chapter 4, the interaction of disturbances with its surrounding, which is the Blasius flow in the case of an isolated surface roughness, will affect the production of the Reynolds stresses. The experiments of Asai et al. (2002), Mitsudharmadi et al. (2004), Bakchinov et al. (1995) and Tandiono et al. (2013) were focussed on the instability characteristics of the disturbances subjected to different wavelength. In these experiments, the disturbances were forced either by surface roughness inside the boundary layer or at the leading edge. The two main instability modes - namely varicose and sinuous modes - were found to be strongly affected by the wavelength of the disturbances. Four different modes (harmonic and sub-harmonic varicose modes, harmonic and sub-harmonic sinuous modes) were found to occur by varying the wavelength (e.g. Konishi and Asai (2004)). However, the appearance of these modes are subjected only to the occurrence of the coherent structures in the transitional boundary layer, unlike the disturbances caused by the convergent riblet.

The experiments performed using isolated convergent riblet in the boundary layer (Chapter 4) showed that the route to turbulence encompassed three different phenomena namely transient growth, instability and vortex breakdown by viscous diffusion with the increasing height of the riblet. Laying importance to flow control, this chapter focuses on the instability characteristics

due to interaction of the vortices and the instability modes that manifests with the varying wavelength of the disturbances. More precisely, given the flow kinematics, this chapter focusses on two main questions as follows:

i) How does the manifestation of the instability modes differ from that due to the occurrence of the hairpin vortices and

ii) How are the instability characteristics different from those of isolated convergent riblet.

Tests were performed for three different wavelengths - $\lambda = 10, 12.5$ and 15 mm, following the analysis in chapter 4 has been carried out.

5.2 Mean Velocity

Time-averaged streamwise velocities were obtained across a spanwise distance covering five pairs of vortices. The iso-contours of the mean streamwise velocities were plotted on the $y - z$ and $x - z$ planes by using the commercial software called TECPLOT. (Note no smoothing was performed for the contours).

As shown in figures 5.1, 5.2 and 5.3, the development of the vortices depicts two scenarios - i) Development without the intermediate vortices as in the case of $\lambda=10$ mm and ii) Development of the vortex pairs with the presence of intermediate vortices (indicated by dashed line in the figures 5.2 and 5.3) as in the case of $\lambda=12.5$ mm and $\lambda=15$ mm. These intermediate vortices arises due to the momentum imbalance between the vortex pairs.

In the case of $\lambda=10$ mm, at the location of initial disturbance ($x=5$ mm), the signs of intermediate vortices arise. After the transient growth regime (between $x=10$ mm and 15 mm), the downwash is resilient to viscous diffusion that hurdles the formation of intermediate vortices. This is primarily due to the close proximity of the vortices. The consistent growth of the vortices culminates in the interaction of the vortices at $x=300$ mm and hence its breakdown to turbulence. In the case of $\lambda=12.5$ mm, the growth of the vortices is similar to that of case $\lambda=10$ mm excepting that the resilience to viscous diffusion occurs at $x=450$ mm and that, the vortex pairs exists throughout the region of investigation. While in the case of $\lambda=15$ mm, the intermediate vortices, alongside the vortex pairs, could be seen throughout the region of investigation.

Basically, the growth and hence the occurrence of the intermediate vortices depends on the mutually induced velocity which is affected by the interaction of the vortex pair. This is well

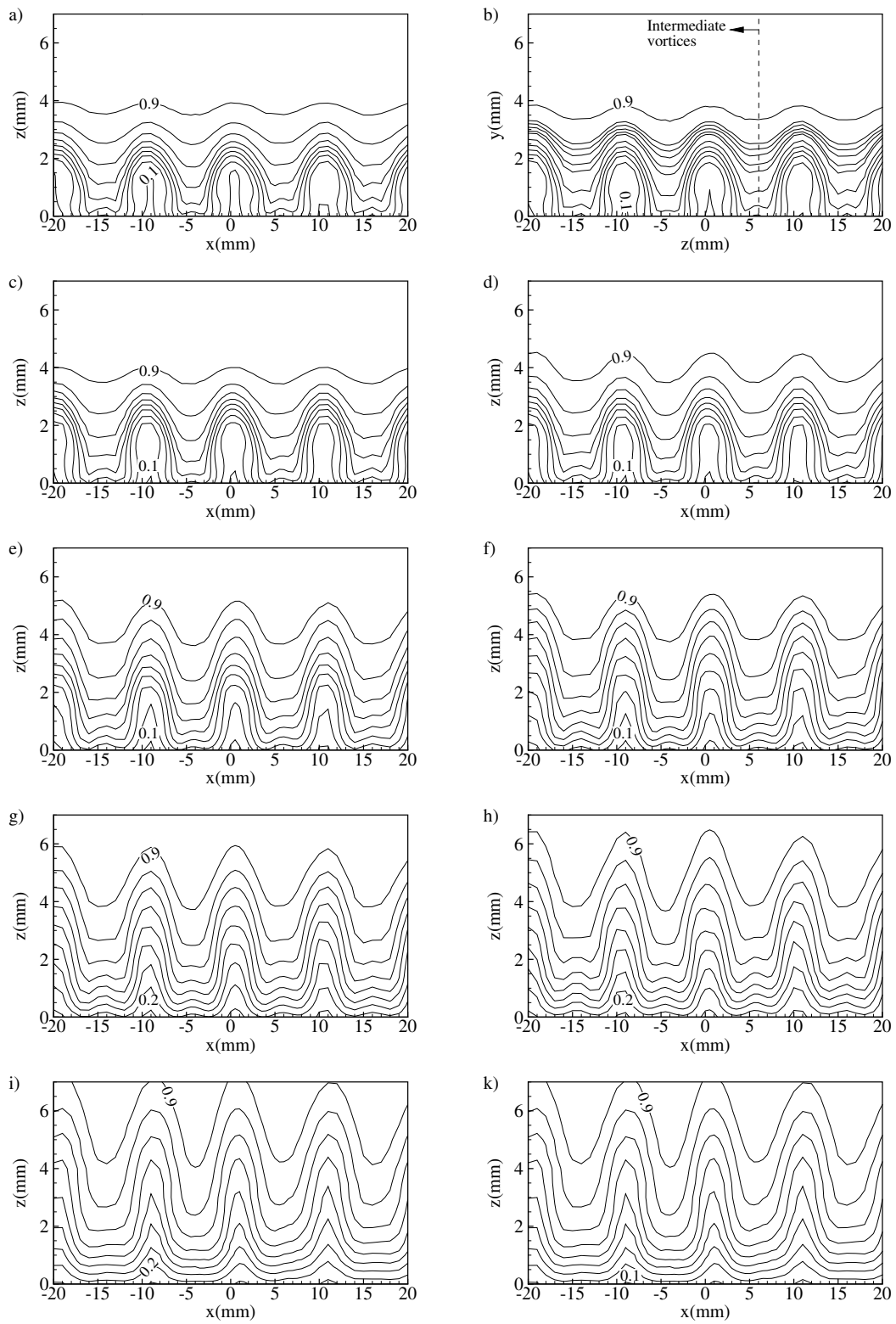


Figure: Caption see following page.

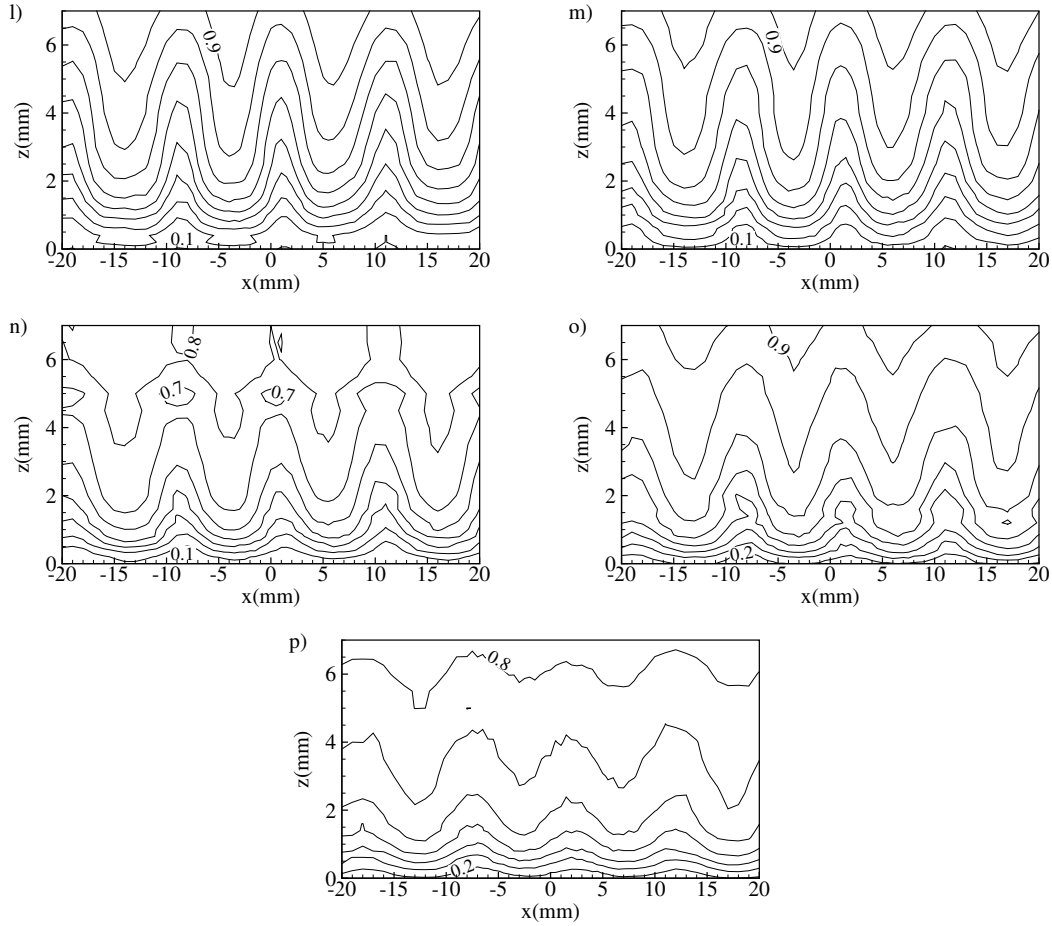


Figure 5.1: Iso- u/U_∞ contour at different cross-stream stations for $\lambda=10$ mm; a) $x=5$ mm, b) $x=10$ mm, c) $x=15$ mm, d) $x=20$ mm, e) $x=50$ mm, f) $x=75$ mm, g) $x=100$ mm h) $x=150$ mm, i) $x=200$ mm, j) $x=250$ mm, k) $x=300$ mm, l) $x=350$ mm, m) $x=400$ mm, n) $x=450$ mm, o) $x=500$ mm.

reflected in the development of the low speed streaks, depicted as contours in $x-z$ planes in figures 5.4, 5.5 and 5.6.

The commonality among these three cases is that the width of the low speed streaks thins down along the downstream. At $y/\delta_k=0.25$, in the case of $\lambda=10$ mm, the thinning down of the streaks occurs downstream of $x=150$ mm, while in the case of $\lambda=12.5$ mm the thinning down occurs upstream of $x=100$ mm and in the case of $\lambda=15$ mm, the thinning down occurs just downstream the transient growth regime ($x=25$ mm). This observation implies that the presence of strong viscous effects is dictated by the mutually induced velocities which in turn depends on the interaction of the vortex pair. In the upwash, the mutually induced velocity away from the wall acts to lift up the vortex pair, while in the downwash, the mutually induced velocity is

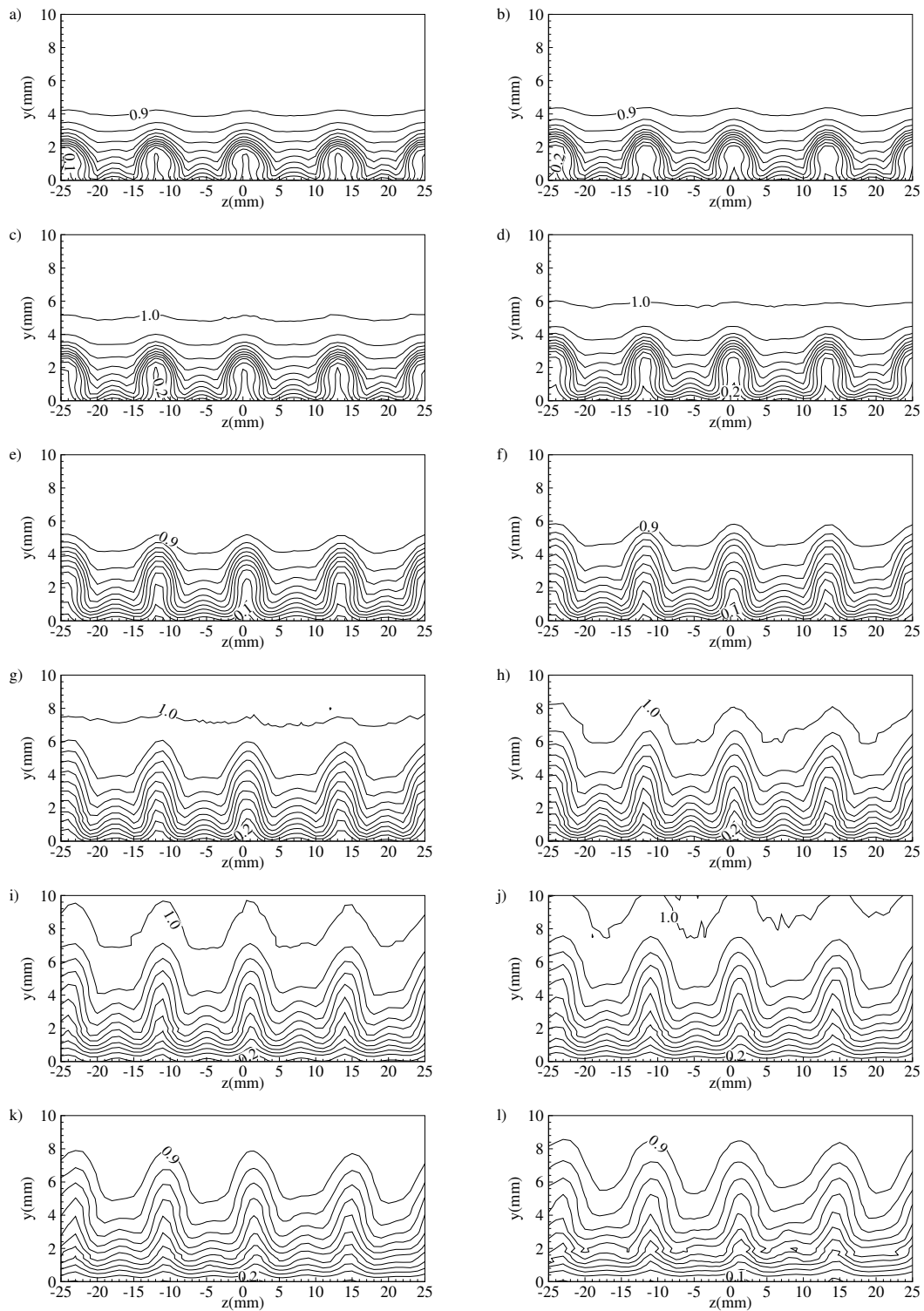


Figure: Caption see following page.

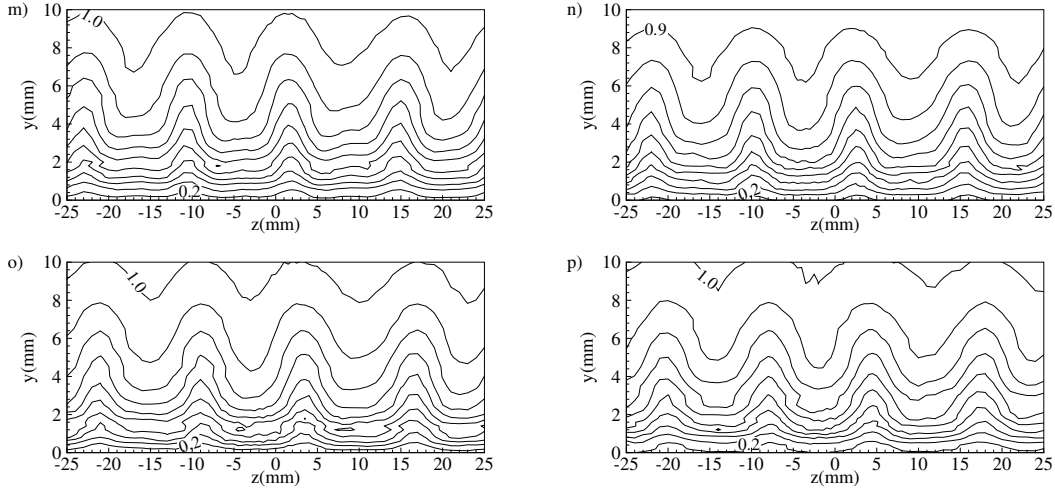


Figure 5.2: Iso- u/U_∞ contour at different cross-stream stations for $\lambda=12.5$ mm; a) $x=5$ mm, b) $x=10$ mm, c) $x=15$ mm, d) $x=25$ mm, e) $x=50$ mm, f) $x=75$ mm, g) $x=100$ mm, h) $x=150$ mm i) $x=200$ mm, j) $x=250$ mm, k) $x=300$ mm, l) $x=350$ mm, m) $x=400$ mm, n) $x=450$ mm, o) $x=500$ mm, p) $x=550$ mm.

towards the wall. It is this balance between the induced velocities that governs the wall-normal position of the vortex pair. In the case of $\lambda=10$ mm, the close proximity of the vortex pair results in stronger downwash compared to $\lambda=12.5$ mm and 15 mm and hence the vortex pair stays closer to the wall. This is well reflected in $x-z$ plane contours corresponding to $y/\delta_k=0.25$ that corresponds to the stem of the vortex pairs. The strong viscous effects extends to $x=150$ mm followed by the thinning down of the streaks in the case of $\lambda=10$ mm compared to the case of $\lambda=12.5$ mm and 15 mm where the viscous effects hardly extend to $x=100$ mm and $x=30$ mm respectively. At $y/\delta_k=0.5$, the width of the low speed streaks are larger than those of $y/\delta_k=0.25$ in all the cases. The low and high speed streaks in the case of $\lambda=10$ mm remain undifferentiated above $x=450$ mm, due to the breakdown of the vortices. In the case of $\lambda=12.5$ mm, the low speed streak from the intermediate vortices, at about $z=\pm 6$, is found to exist till $x=350$ mm, while in the case of $\lambda=15$ mm, the streaks from the intermediate vortices were found to co-exist till the region of investigation. At $y/\delta_k=0.75$ and 1, the low speed streaks, that corresponds to the head of the vortex pair, attain higher velocities than those compared to $y/\delta_k=0.25$ and 0.5.

Figure 5.7 shows the downstream development of streamwise velocity profile across the boundary layer for the three wavelengths. From figures 5.1, 5.2, 5.3, since the development of the vortex pair are symmetrical, the plot presented here corresponds to the center of the upwash of

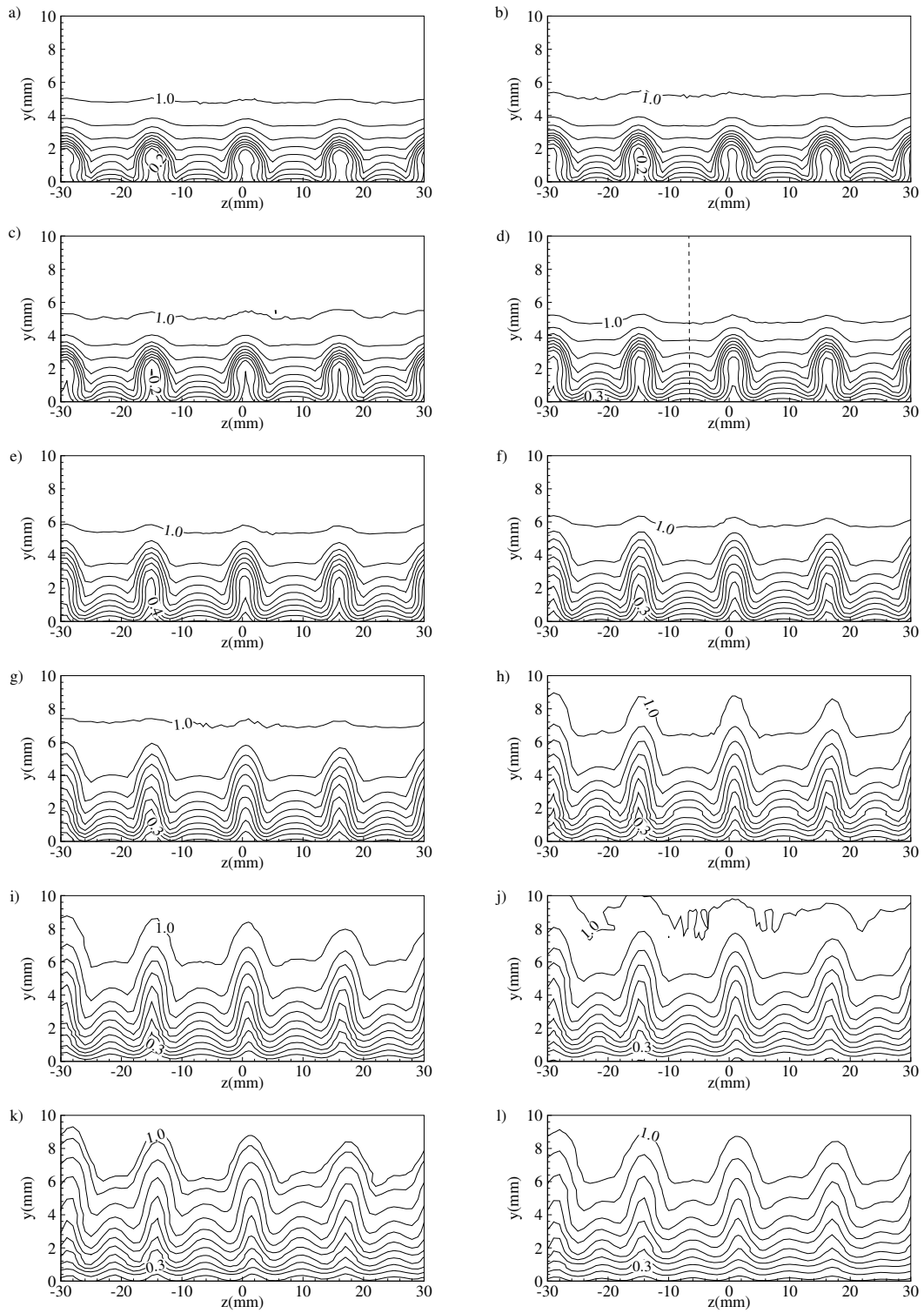


Figure: Caption see following page.

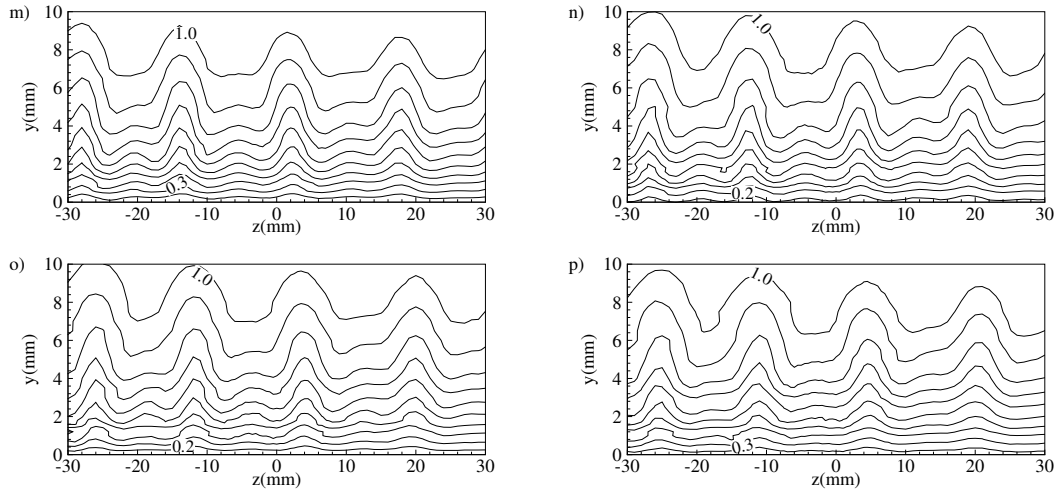


Figure 5.3: Iso- u/U_∞ contour at different cross-stream stations for $\lambda=15$ mm; a) $x=5$ mm, b) $x=10$ mm, c) $x=15$ mm, d) $x=25$ mm, e) $x=50$ mm, f) $x=75$ mm, g) $x=100$ mm h) $x=150$ mm, i) $x=200$ mm, j) $x=250$ mm, k) $x=300$ mm, l) $x=350$ mm, m) $x=400$ mm, n) $x=450$ mm, o) $x=500$ mm, p) $x=550$ mm.

the middle vortex with upwash at $z=0$. In all the three cases, initially at $x=5$ mm, the inflectional velocity profile due to the vortex pair appears. The difference lies in the characteristics of the inflectional points. In the case of $\lambda=10$ mm, the inflectional velocity profile is S-shaped. But, for $\lambda=12.5$ mm, the signature of low momentum fluid riding over high momentum fluid starts to appear while it is well pronounced in $\lambda=15$ mm. The inflection point, in transient growth regime (between $x=5$ mm and 25 mm), moves away from the wall and later disappears with the increasing downstream distance. However, a mild second inflectional point occurs around $\eta=2.5$ at $x=200$ mm in all the three cases. In the case of $\lambda=10$ mm, this is not important as the interaction of the vortices further downstream disburse the vortex pair. But in the case of $\lambda=12.5$ and $\lambda=15$ mm, this might be the effect of the onset of sinuous modes. This can be confirmed from the turbulence intensity profiles as shown in figures 5.14, 5.15 and 5.16. This characteristic is in contrast to the case of hairpin vortices, wherein the inflectional velocity profile is advected away from the wall making the low momentum fluid more susceptible to the outer free stream flow. This susceptibility either results in the formation of the train of hairpin vortices that is seen to be manifested as subharmonic or harmonic varicose mode (Asai et al., 2002) or results in co-existence of varicose and sinuous mode as in the case of Gortler instability mechanism (Mitsudharmadi et al., 2004).

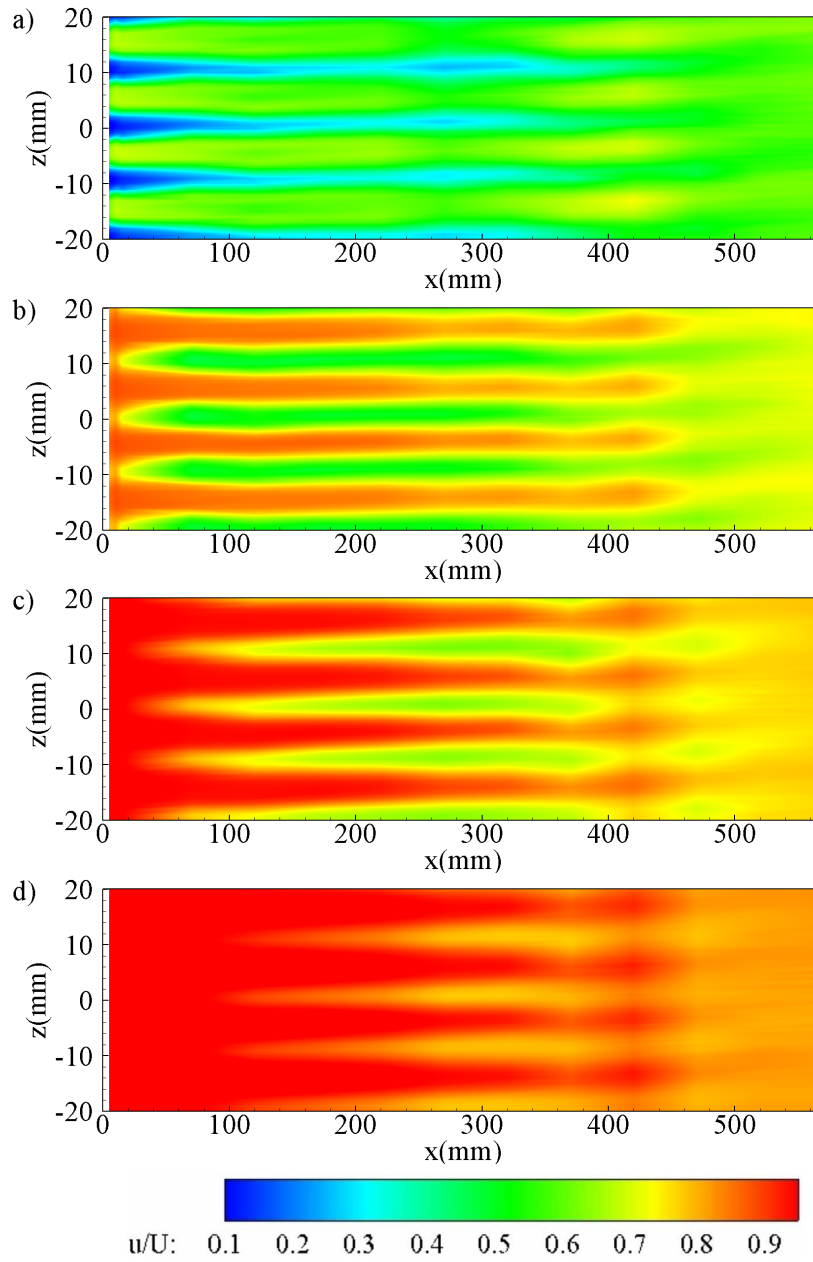


Figure 5.4: Iso- u/U_∞ contours at $x-z$ plane for $\lambda=10$ mm; a) $y/\delta_k=0.25$, b) $y/\delta_k=0.5$, c) $y/\delta_k=0.75$, d) $y/\delta_k=1$.

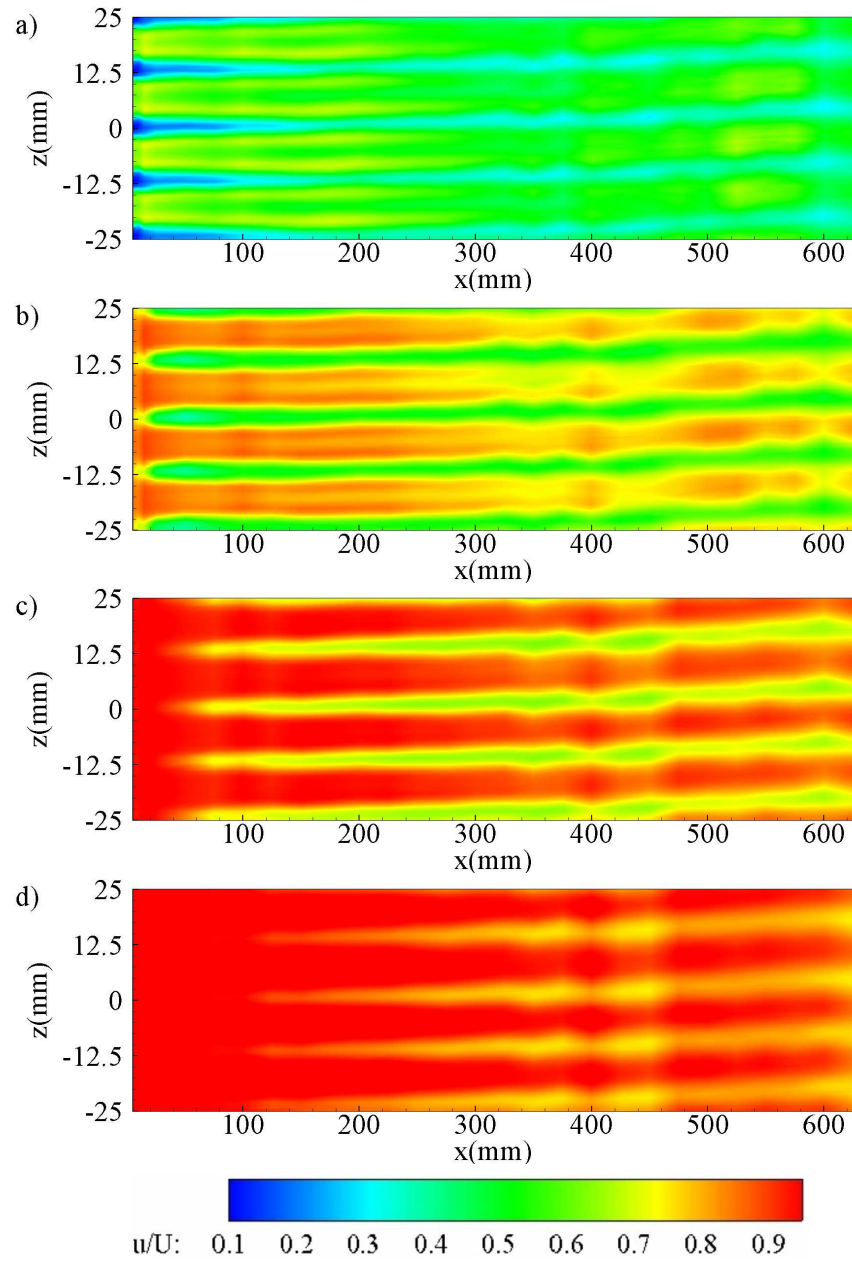


Figure 5.5: Iso- u/U_∞ contour at $x - z$ plane for $\lambda = 12.5$ mm; a) $y/\delta_k = 0.25$, b) $y/\delta_k = 0.5$, c) $y/\delta_k = 0.75$, d) $y/\delta_k = 1$.

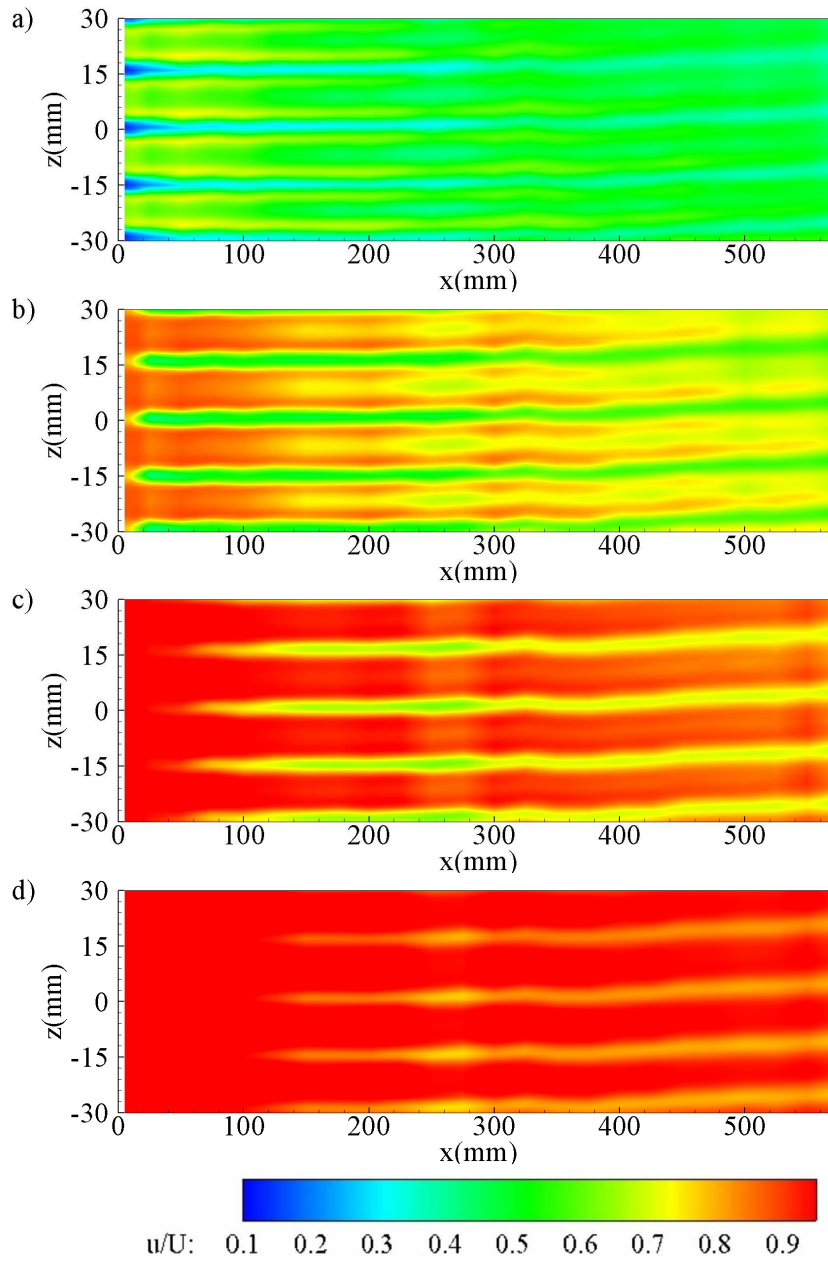


Figure 5.6: Iso- u/U_∞ contour at $x-z$ plane for $\lambda=15$ mm; a) $y/\delta_k=0.25$, b) $y/\delta_k=0.5$, c) $y/\delta_k=0.75$, d) $y/\delta_k=1$.

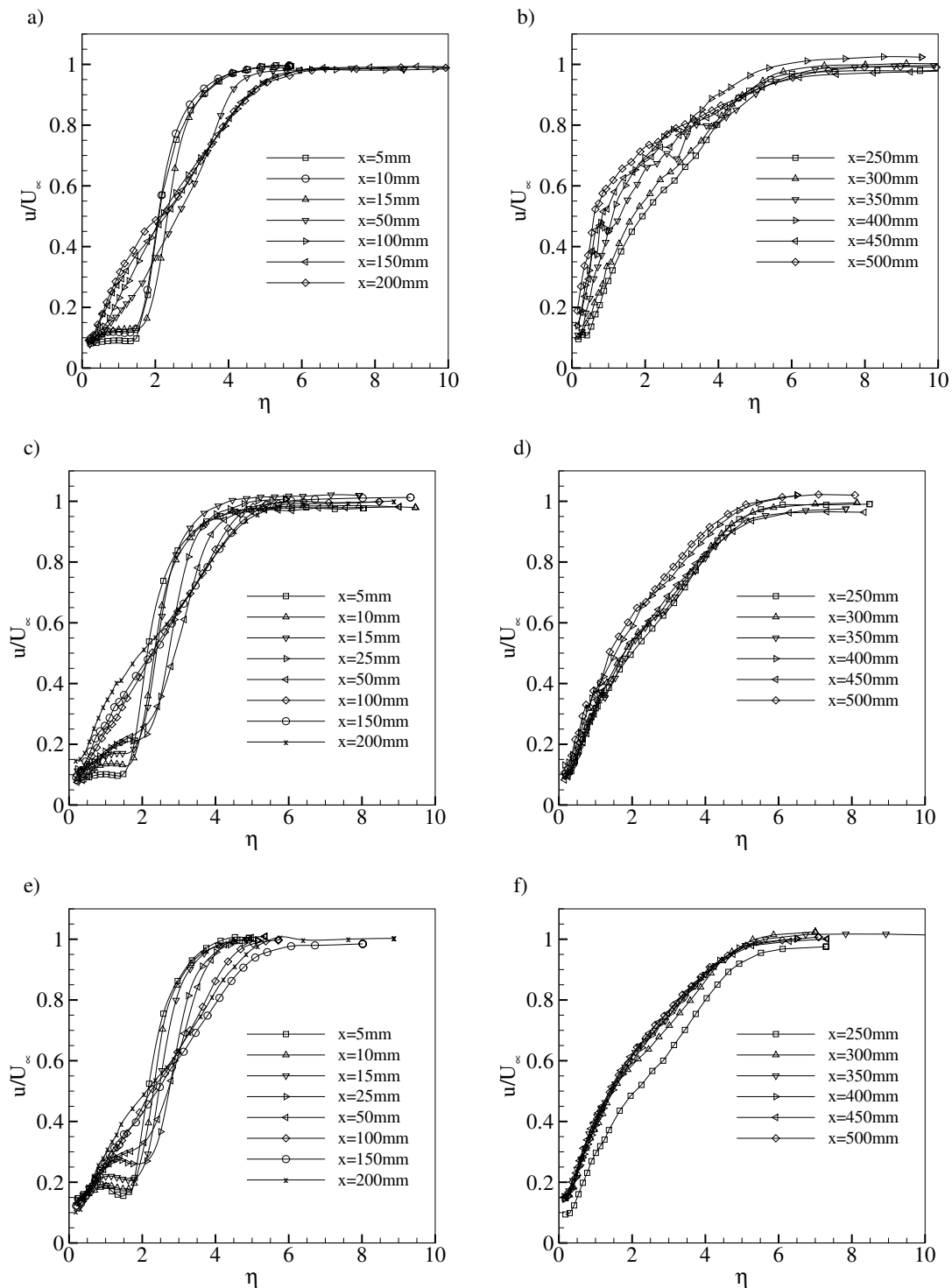


Figure 5.7: Downstream development of upwash streamwise velocity profiles across the boundary layer for a) and b) $\lambda=10$ mm, c) and d) $\lambda=12.5$ mm, e) and f) $\lambda=15$ mm.

5.3 Shear stress

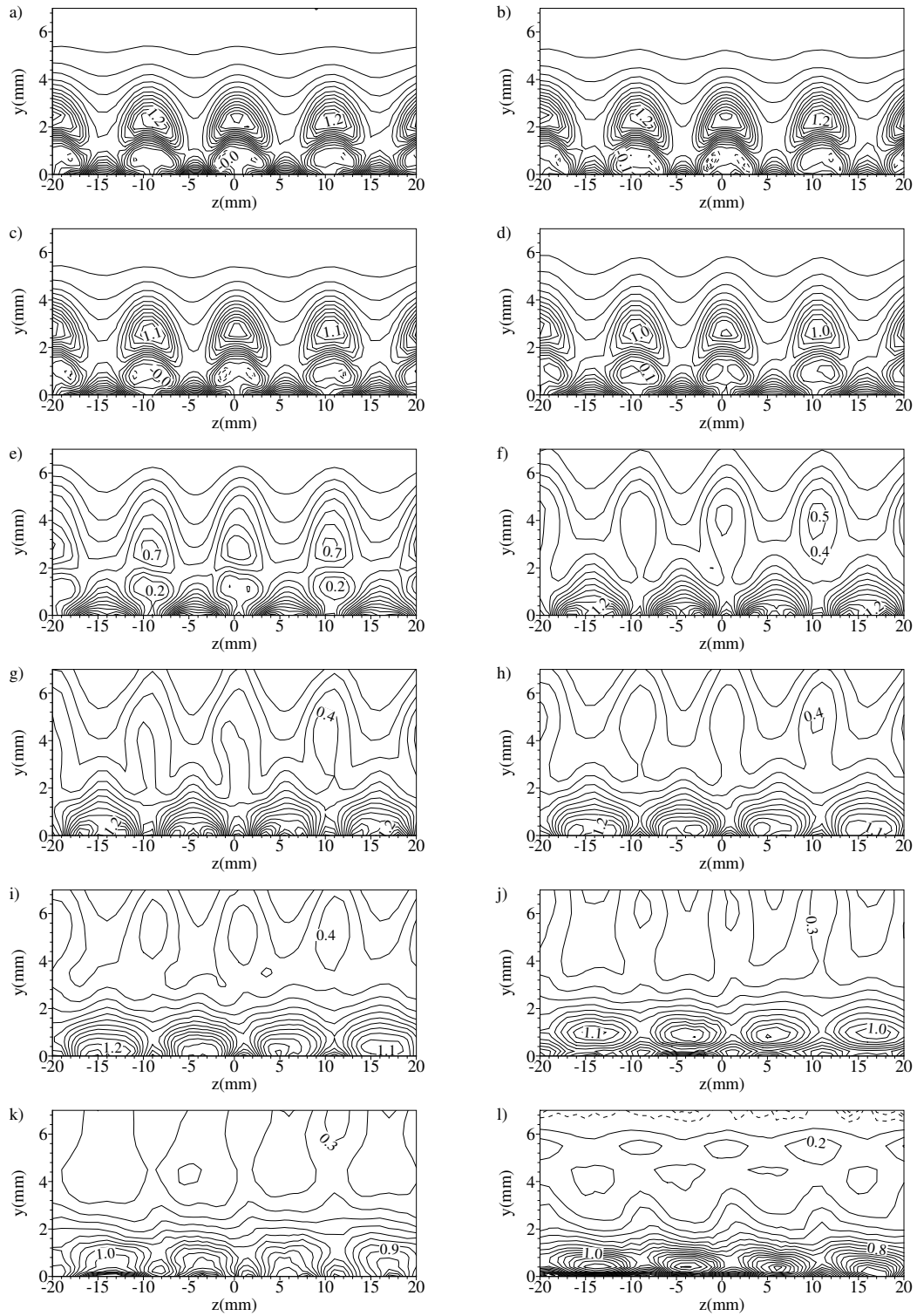


Figure: Caption see following page.

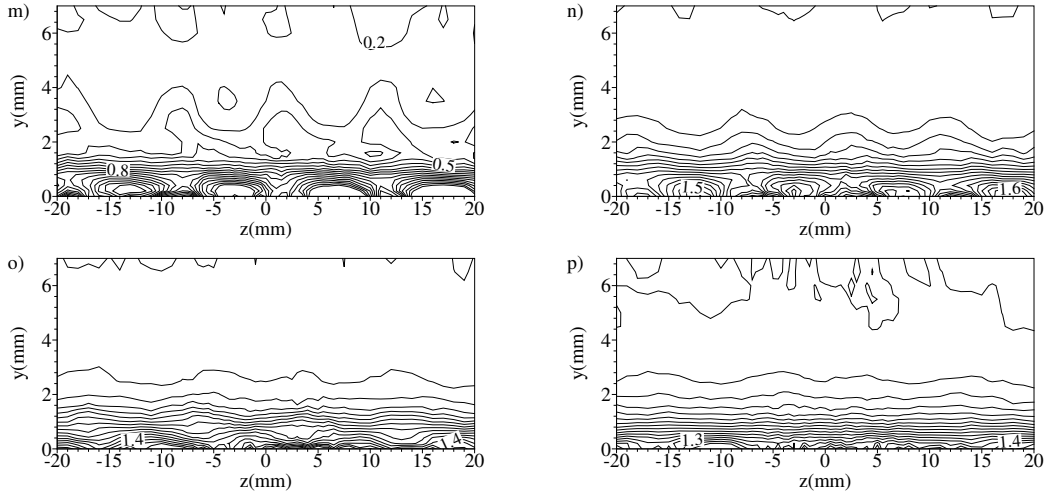


Figure 5.8: Iso-shear($\partial u/\partial y$) contour at different cross-stream stations for $\lambda=10$ mm; a) $x=5$ mm, b) $x=10$ mm, c) $x=15$ mm, d) $x=25$ mm, e) $x=50$ mm, f) $x=100$ mm g) $x=150$ mm, h) $x=200$ mm, i) $x=250$ mm, j) $x=300$ mm, k) $x=350$ mm, l) $x=400$ mm, m) $x=450$ mm, n) $x=500$ mm, o) $x=550$ mm, p) $x=600$ mm.

Figures 5.8, 5.9 and 5.10 shows the $\partial u/\partial y$ iso-shear contours at several streamwise locations for $\lambda=10$ mm, 12.5mm and 15mm respectively. In all the cases, besides the strong shear due to the wall, there are regions of strong positive shear in the boundary layer edge at the upwash. The high shear regions rapidly moves outward at $x=50$ mm in the case of $\lambda=12.5$ mm and 15mm compared to $\lambda=10$ mm where the movement of the high shear regions is hindered due to the interaction of the vortex pairs at close proximities. These strong positive shear regions are due to the interaction between the uplifted low momentum fluid and outer high momentum fluid. In addition to positive shear regions, regions of negative shear are seen in the cases of $\lambda=12.5$ mm and 15mm in the near downstream of the riblet (between $x=5$ mm and 25mm). This is in concurrent to the upwash velocity profiles (as shown in figures 5.2 and 5.3). Excluding the strong shear regions near the wall, three maxima are found in shear contours in the transient growth regime: one positive peak at the head of the vortex pair, and two relatively weak negative shear regions distributed symmetrically to the stem of the vortex pair. In addition to the inflection points in the wall-normal direction, the velocity profile is also inflected in the spanwise direction as depicted by the high positive and negative $\partial u/\partial z$ regions that are distributed symmetrically to the low-speed streaks, as shown in figures 5.11, 5.12 and 5.13. These higher positive and negative regions which are concentrated near the wall at $x=5$ mm spread across the boundary layer with

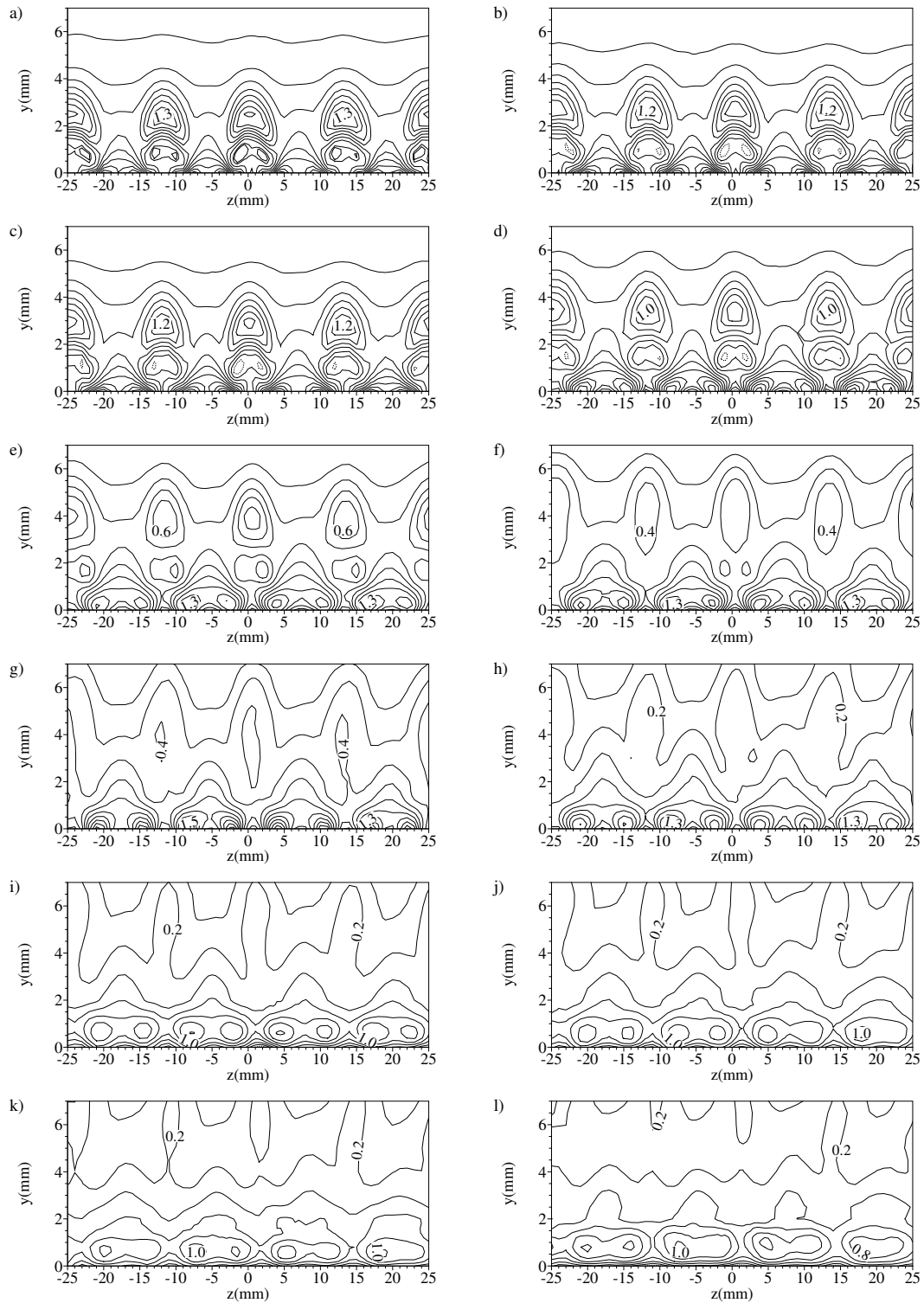


Figure: Caption see following page.

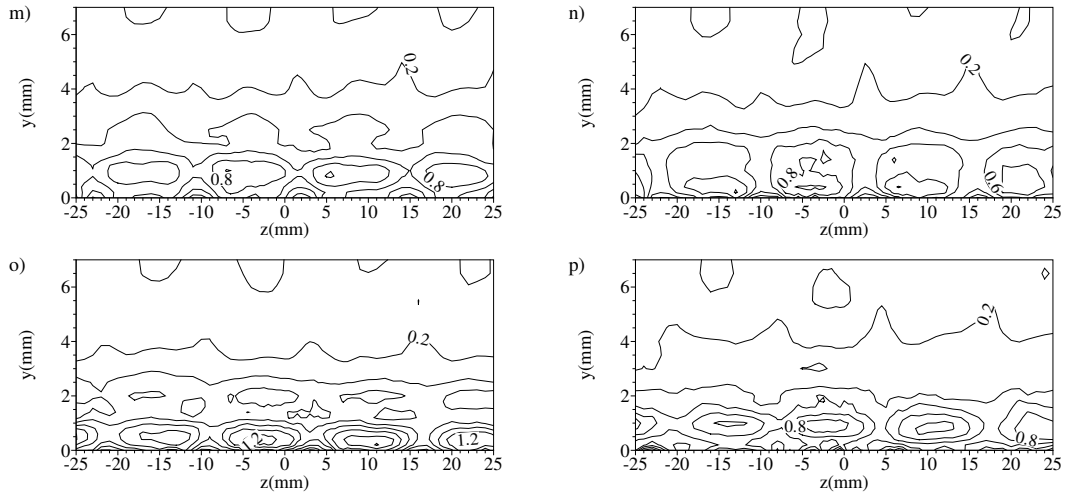


Figure 5.9: Iso-shear($\partial u/\partial y$) contour at different cross-stream stations for $\lambda=12.5$ mm; a) $x=5$ mm, b) $x=10$ mm, c) $x=15$ mm, d) $x=25$ mm, e) $x=50$ mm, f) $x=75$ mm, g) $x=100$ mm, h) $x=150$ mm, i) $x=200$ mm, j) $x=250$ mm, k) $x=300$ mm, l) $x=350$ mm, m) $x=400$ mm, n) $x=450$ mm, o) $x=500$ mm, p) $x=550$ mm.

the increasing streamwise distance. In the case of $\lambda=10$ mm, the high shear regions collapse due to the breakdown of vortices, while in the case of $\lambda=12.5$ mm and 15 mm, the shear regions, although decaying, are found to exist throughout the region of investigation. Furthermore, in the case of $\lambda=15$ mm the shear regions due to the intermediate vortices are found to co-exist until $x=350$ mm. In the case of coherent structures embedded in the transitional boundary layer, four high regions tend to occur- two high shear regions distributed symmetrically about the low momentum fluid lifted by the leg of the hairpin vortices and two high shear regions due to the head of the hairpin vortices.

Evidently, the peaks corresponding to $\partial u/\partial y$ and $\partial u/\partial z$ are concurrent with the intense regions of fluctuations as depicted in turbulence intensity profiles (figures 5.14, 5.15 and 5.16). Clearly the instability motions of varicose modes are due to $\partial u/\partial y$ and that due to sinuous motions are due to $\partial u/\partial z$.

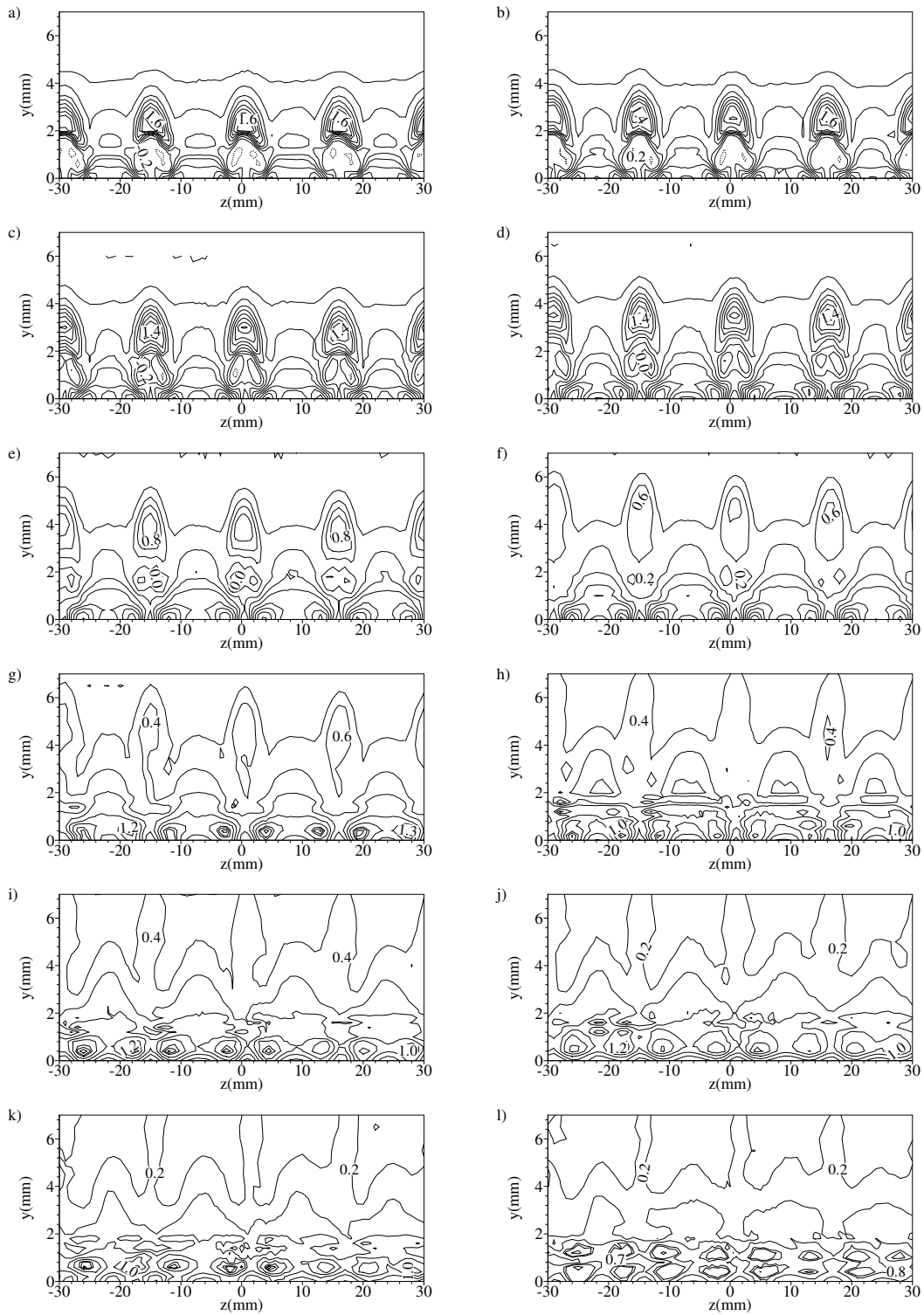


Figure: Caption see following page.

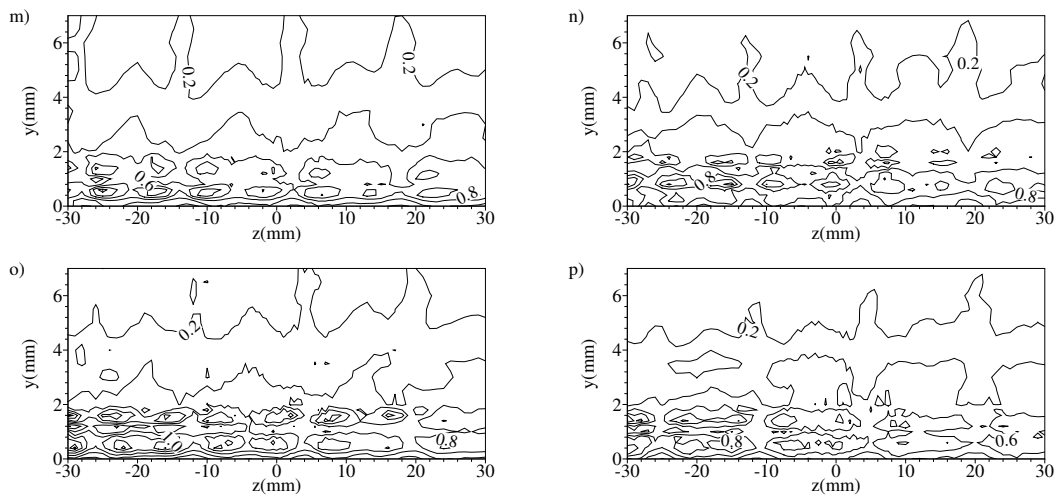


Figure 5.10: Iso-shear($\partial u/\partial y$) contour at different cross-stream stations for $\lambda=15$ mm; a) $x=5$ mm, b) $x=10$ mm, c) $x=15$ mm, d) $x=25$ mm, e) $x=50$ mm, f) $x=75$ mm, g) $x=100$ mm h) $x=150$ mm, i) $x=200$ mm, j) $x=250$ mm, k) $x=300$ mm, l) $x=350$ mm, m) $x=400$ mm, n) $x=450$ mm, o) $x=500$ mm, p) $x=550$ mm.

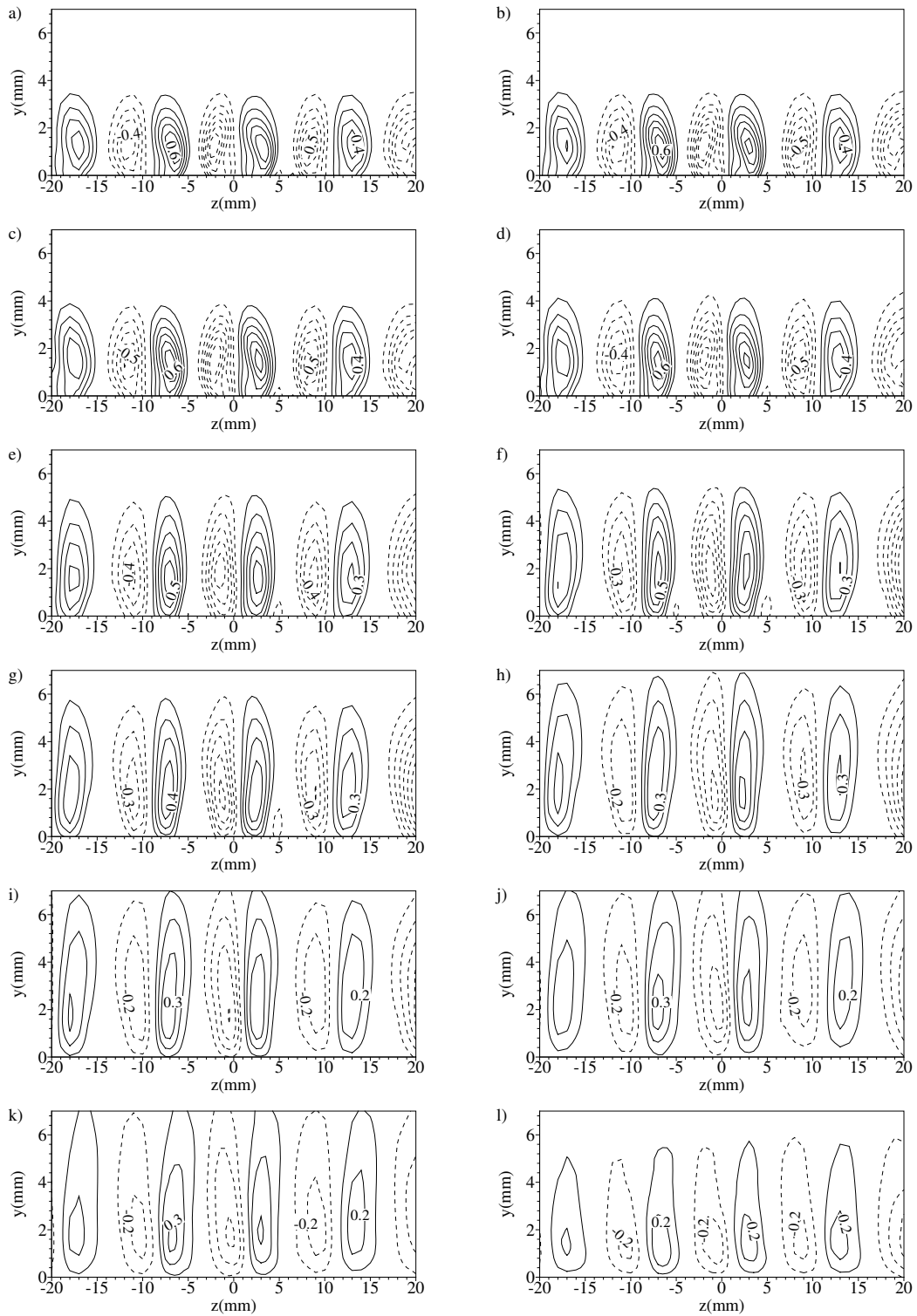


Figure: Caption see following page.

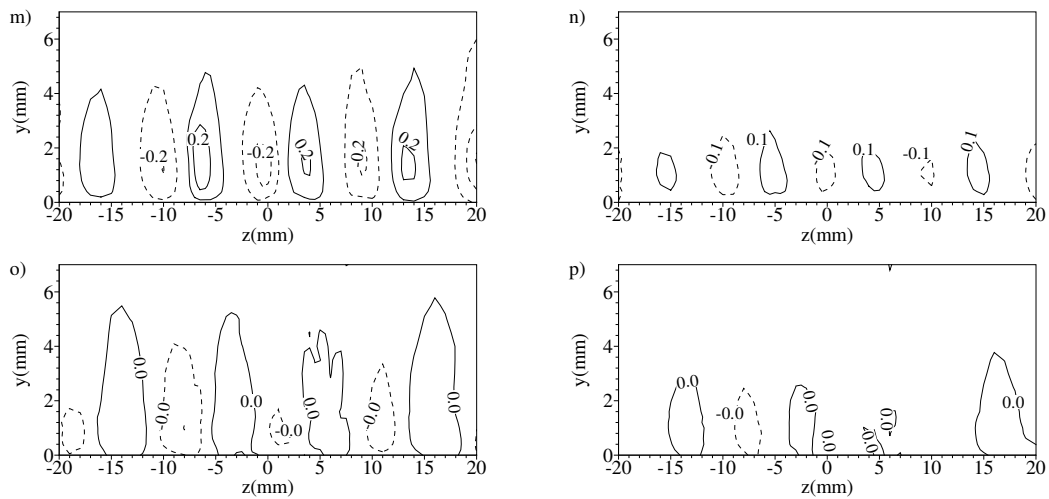


Figure 5.11: Iso-shear($\partial u/\partial z$) contour at different cross-stream stations for $\lambda=10$ mm; a) $x=5$ mm, b) $x=10$ mm, c) $x=15$ mm, d) $x=25$ mm, e) $x=50$ mm, f) $x=75$ mm, g) $x=100$ mm, h) $x=150$ mm, i) $x=200$ mm, j) $x=250$ mm, k) $x=300$ mm, l) $x=350$ mm, m) $x=400$ mm, n) $x=450$ mm, o) $x=500$ mm, p) $x=550$ mm.

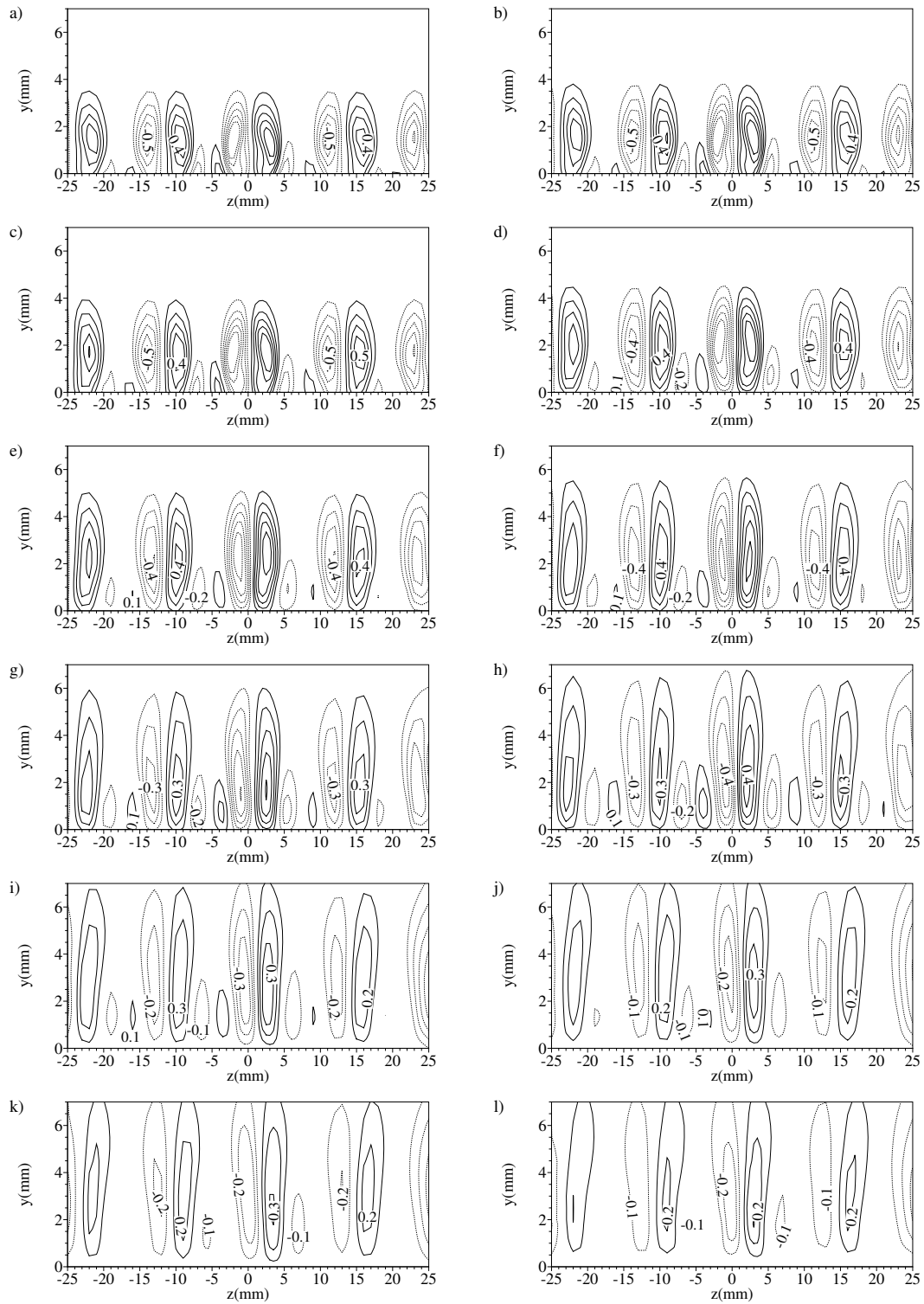


Figure: Caption see following page.

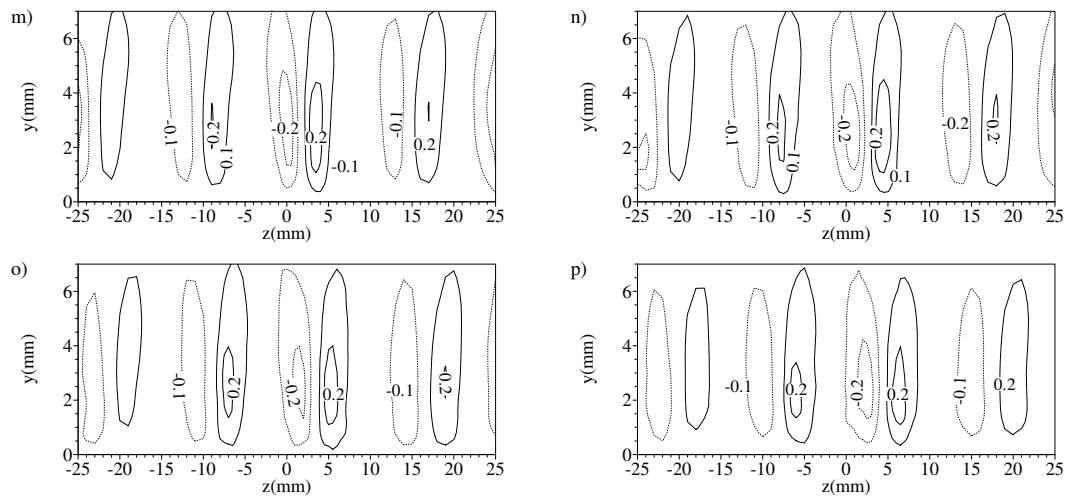


Figure 5.12: Iso-shear($\partial u/\partial z$) contour at different cross-stream stations for $\lambda=12.5$ mm; a) $x=5$ mm, b) $x=10$ mm, c) $x=15$ mm, d) $x=25$ mm, e) $x=50$ mm, f) $x=75$ mm, g) $x=100$ mm h) $x=150$ mm, i) $x=200$ mm, j) $x=250$ mm, k) $x=300$ mm, l) $x=350$ mm, m) $x=400$ mm, n) $x=450$ mm, o) $x=500$ mm, p) $x=550$ mm.

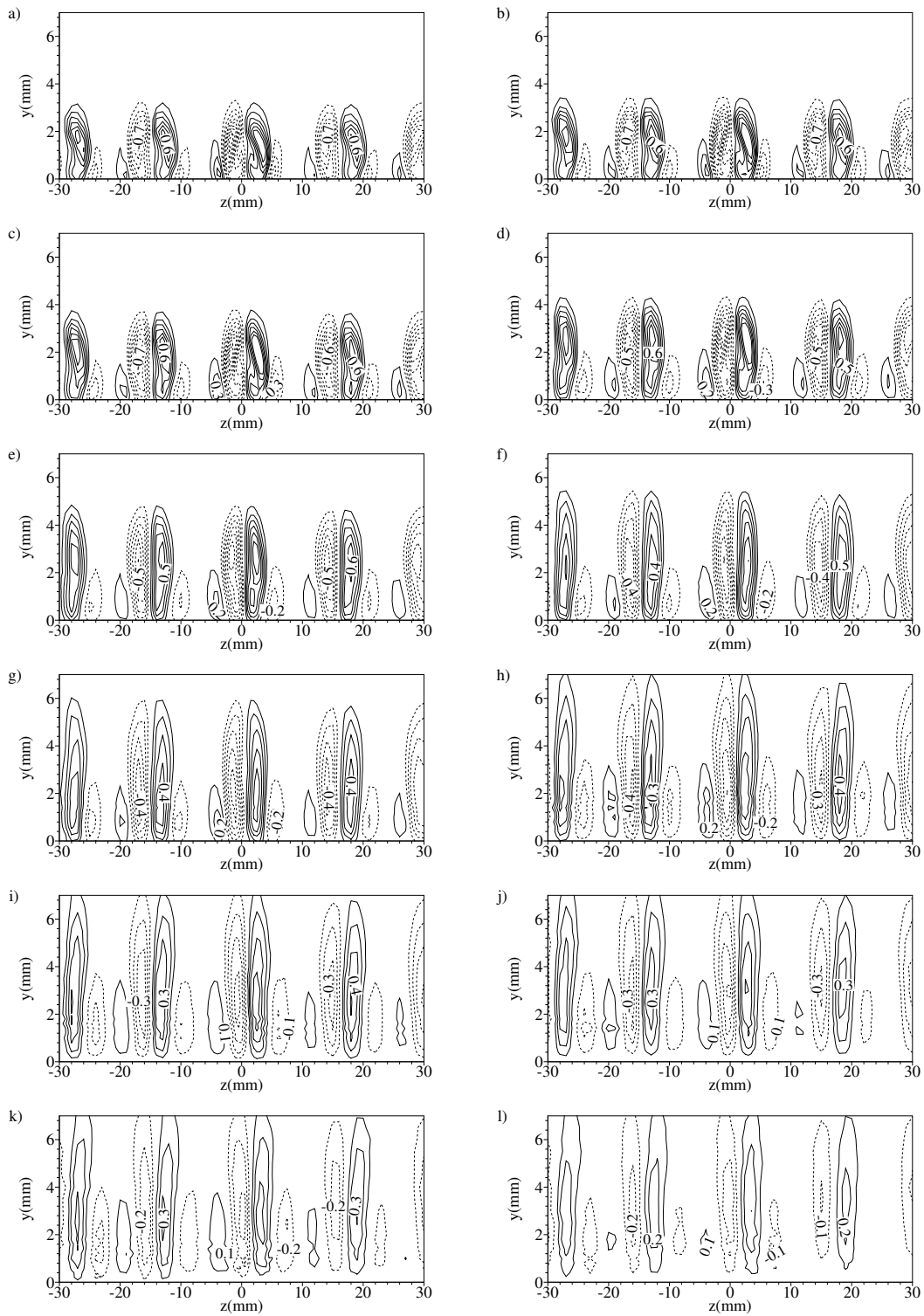


Figure: Caption see following page.

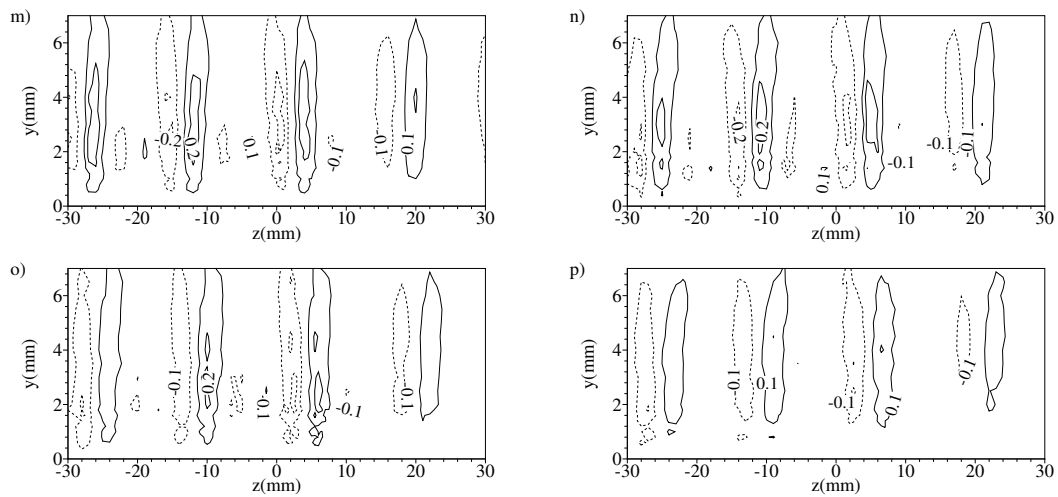


Figure 5.13: Iso-shear($\partial u/\partial z$) contour at different cross-stream stations for $\lambda=15$ mm; a) $x=5$ mm, b) $x=10$ mm, c) $x=15$ mm, d) $x=25$ mm, e) $x=50$ mm, f) $x=75$ mm, g) $x=100$ mm, h) $x=150$ mm, i) $x=200$ mm, j) $x=250$ mm, k) $x=300$ mm, l) $x=350$ mm, m) $x=400$ mm, n) $x=450$ mm, o) $x=500$ mm, p) $x=550$ mm.

5.4 Fluctuating Velocity

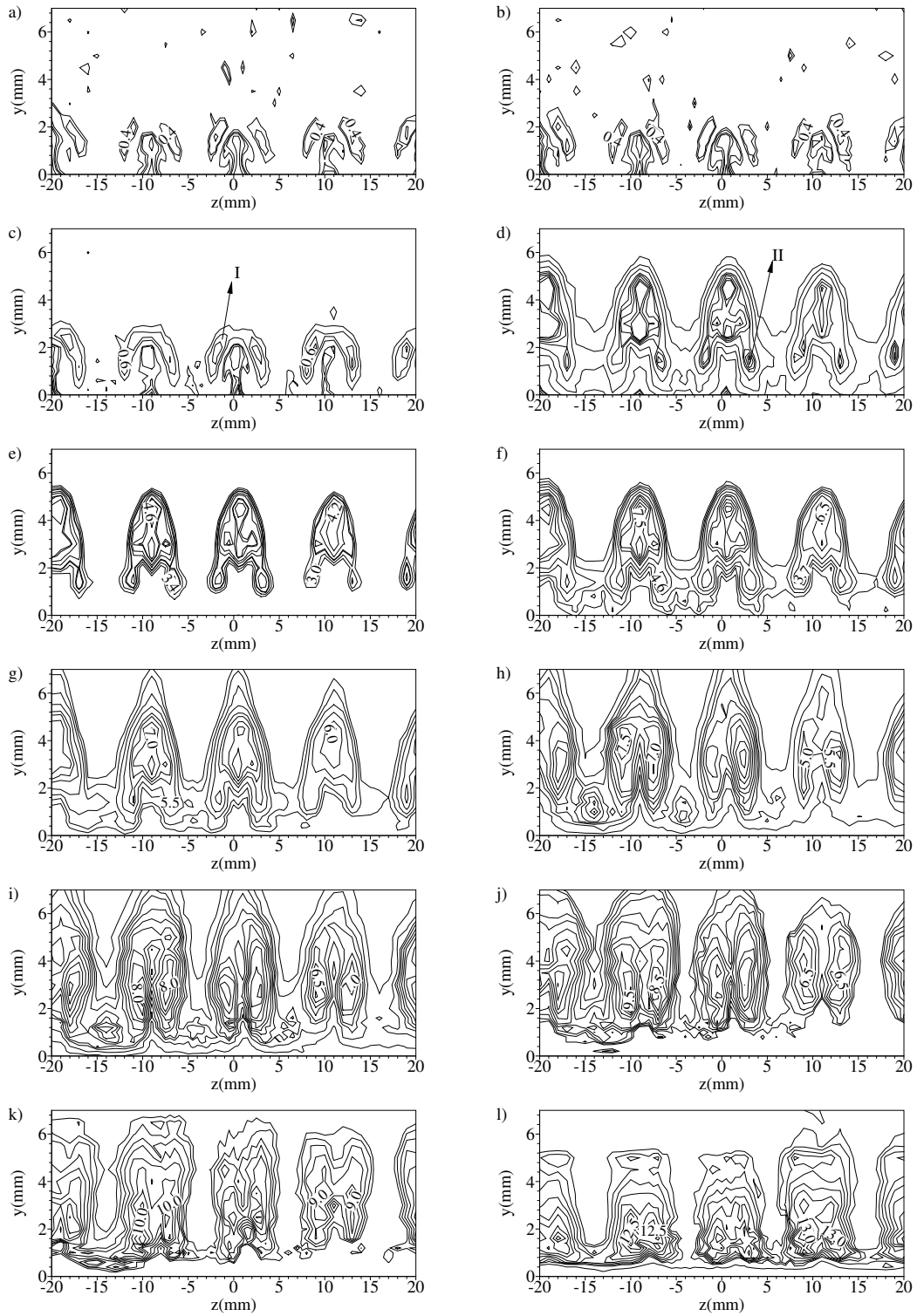


Figure: Caption see following page.

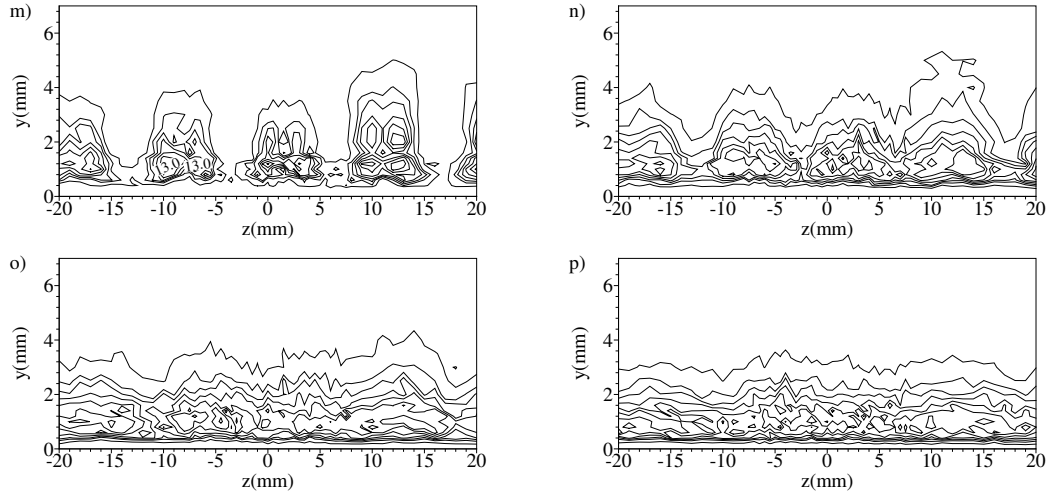


Figure 5.14: Iso-Tu contour at different cross-stream stations for $\lambda=10$ mm; a) $x=5$ mm, b) $x=10$ mm, c) $x=15$ mm, d) $x=25$ mm, e) $x=50$ mm, f) $x=75$ mm, g) $x=100$ mm h) $x=150$ mm, i) $x=200$ mm, j) $x=250$ mm, k) $x=300$ mm, l) $x=350$ mm, m) $x=400$ mm, n) $x=450$ mm, o) $x=500$ mm, p) $x=550$ mm.

The fluctuating component of streamwise velocity (u') is presented in terms of turbulence intensity (Tu) of the middle vortex pair at several streamwise distance for all the three cases. Initially, as can be seen in figures 5.14, 5.15 and 5.16, the intense region of Tu is distributed symmetrically to the upwash. Later along the downstream, at $x=25$ mm, these concentrations develop into a fully developed varicose mode with regions I and II. Region I corresponds to the interaction of the uplifted low momentum fluid with the outer high momentum fluid while region II corresponds to the high shear regions of $\partial u/\partial y$ on either side of the stem of the vortex pair. Further downstream, in all these cases, the varicose mode is found to decay and transition to sinuous mode takes place at $x=200$ mm. Downstream of $x=200$ mm, the Tu concentrations are coherent with those of $\partial u/\partial z$ contours. The only difference is that breakdown of the vortex pairs due to its interaction leads to collapse of sinuous modes downstream of $x=400$ mm in the case of $\lambda=10$ mm, while in the case of $\lambda=12.5$ mm and 15 mm, the concentrations of the intermediate vortices co-exist with the concentrations of the vortex pair near the wall, between the streamwise stations $x=400$ mm and 550 mm.

In order to compare the growth of the modes to that of an isolated convergent riblet, the maximum values of Tu were extracted from the experimental data at different streamwise stations and are plotted as shown in figure 5.17. For varicose mode region I exhibits maximum fluctuation in

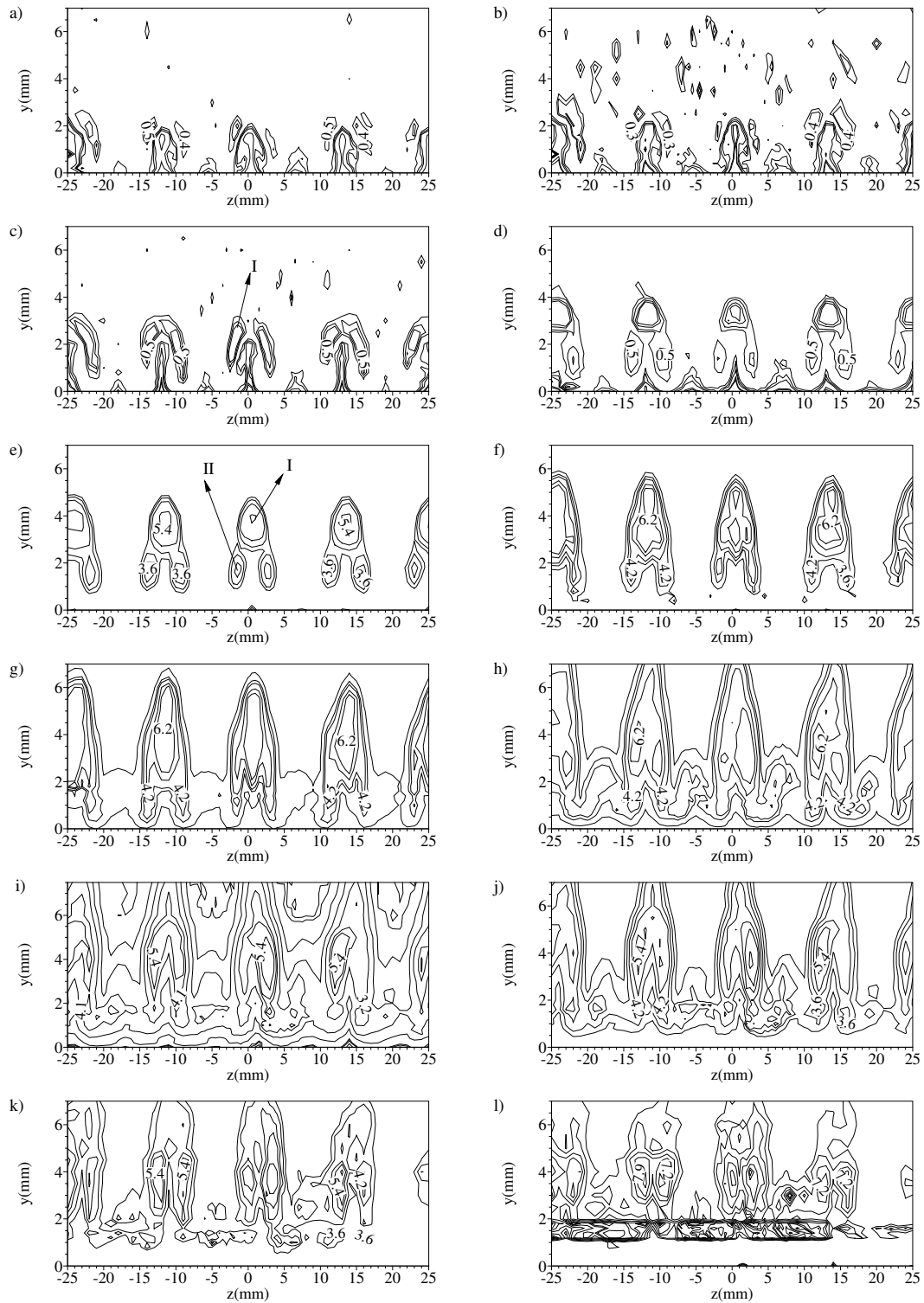


Figure: Caption see following page.

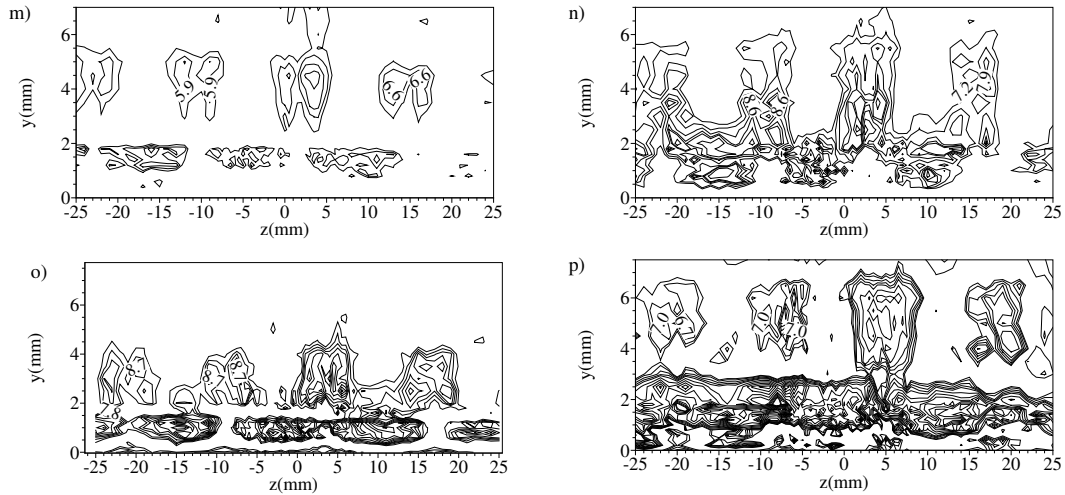


Figure 5.15: Iso-Tu contour at different cross-stream stations for $\lambda=12.5$ mm; a) $x=5$ mm, b) $x=10$ mm, c) $x=15$ mm, d) $x=25$ mm, e) $x=50$ mm, f) $x=75$ mm, g) $x=100$ mm h) $x=150$ mm, i) $x=200$ mm, j) $x=250$ mm, k) $x=300$ mm, l) $x=350$ mm, m) $x=400$ mm, n) $x=450$ mm, o) $x=500$ mm, p) $x=550$ mm.

disturbance velocity and for sinuous modes, the peaks of Tu are symmetrically distributed about the low speed streaks. The solid line arrows in the figure marks the end of the development of varicose mode while the dashed line marks the end of transition and inception of sinuous modes. As evident from the plot, with increasing wavelength, the fluctuations of the streamwise velocity decrease. The steep growth of the varicose mode between $x=5$ mm and 25 mm is coherent with that of the isolated riblet case (figure 4.18). However, the fluctuations of streamwise velocity are higher in the case of isolated riblet. Also, it can be seen that with respect to increasing wavelength, the fluctuations of streamwise velocity decreases leading to a lower Tu values along the downstream. In the case of $\lambda=12.5$ mm and 15 mm, the wall normal position of the peaks of Tu corresponding to sinuous modes differ with respect to the isolated riblet case due to the interaction of the intermediate vortices with the vortex pairs.

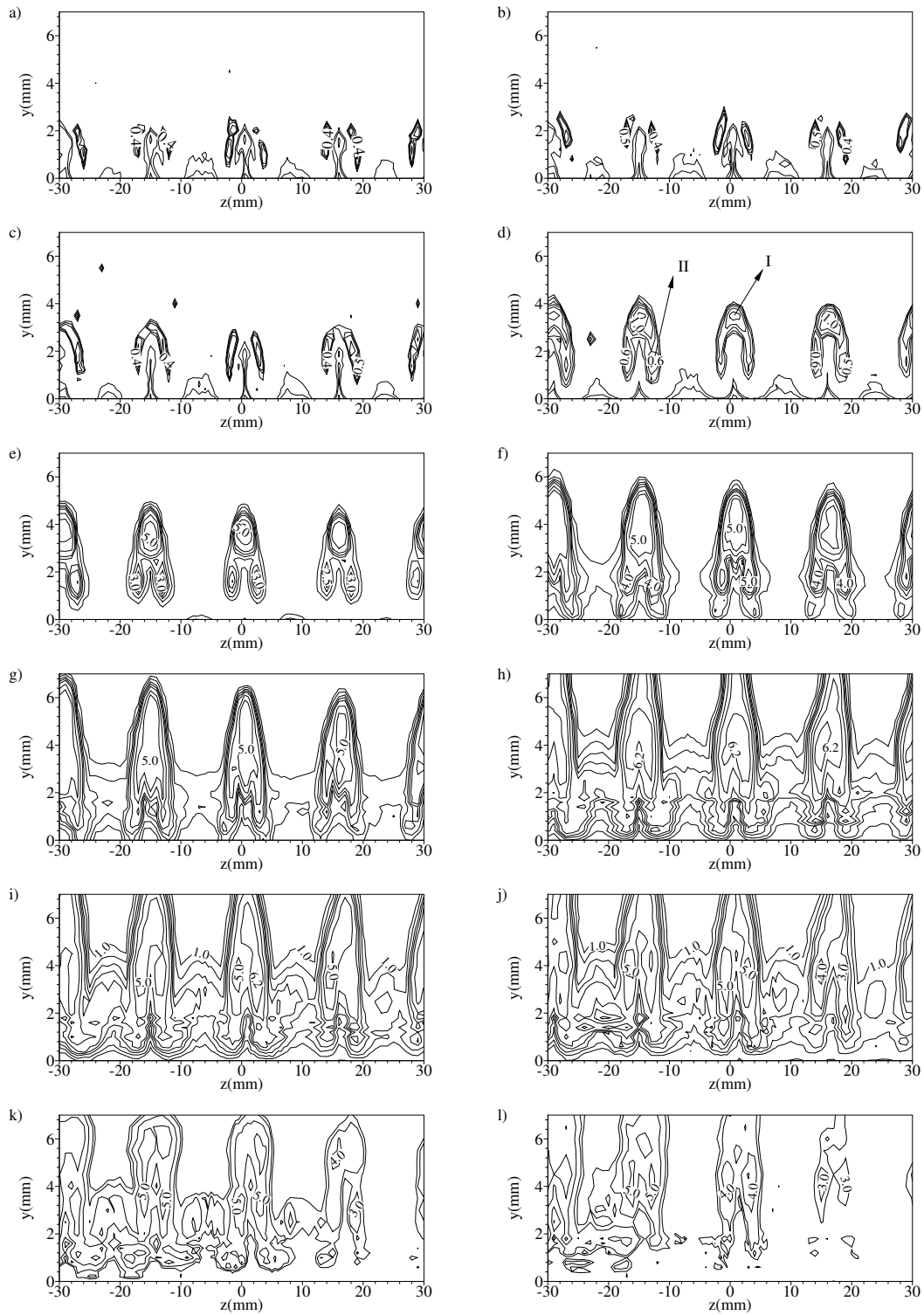


Figure: Caption see following page.

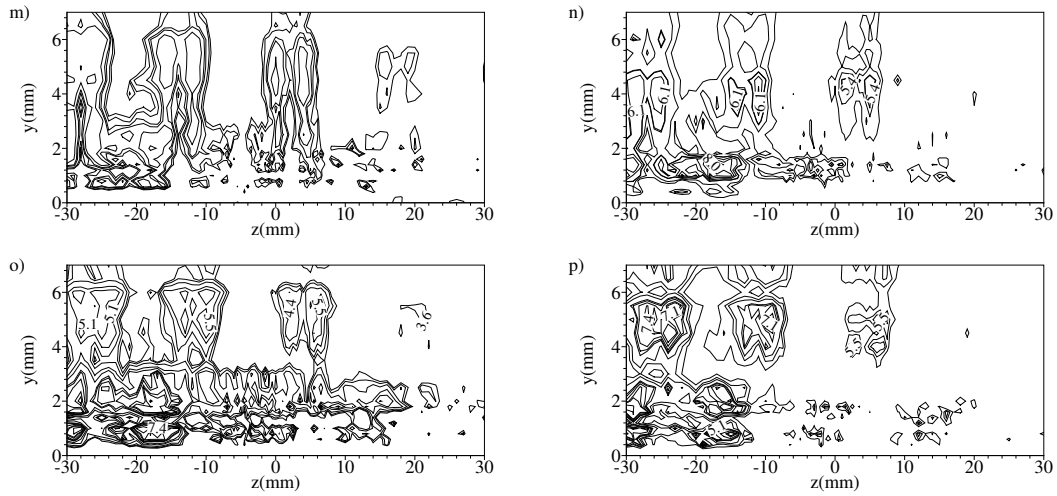


Figure 5.16: Iso-Tu contour at different cross-stream stations for $\lambda=15$ mm; a) $x=5$ mm, b) $x=10$ mm, c) $x=15$ mm, d) $x=25$ mm, e) $x=50$ mm, f) $x=75$ mm, g) $x=100$ mm h) $x=150$ mm, i) $x=200$ mm, j) $x=250$ mm, k) $x=300$ mm, l) $x=350$ mm, m) $x=400$ mm, n) $x=450$ mm, o) $x=500$ mm, p) $x=550$ mm.

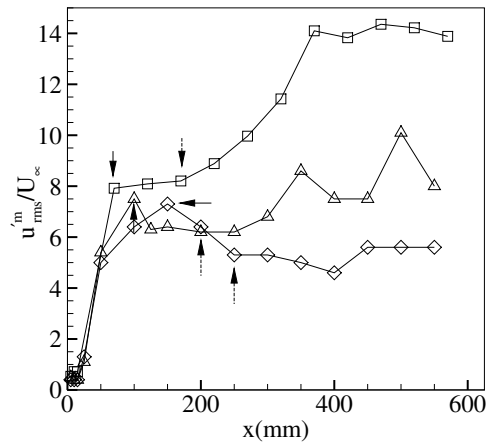


Figure 5.17: Growth of varicose and sinuous modes in terms of maximum Tu corresponding the middle vortex pair: \square - $\lambda=10$ mm, \triangle - $\lambda=12.5$ mm, \diamond = 15 mm.

5.5 Vortex Growth Rate

The disturbance amplitude parameter κ (Eqn. 4.2) as defined in chapter 4 is used to assess the vortex growth rate in terms of mean streamwise velocity component.

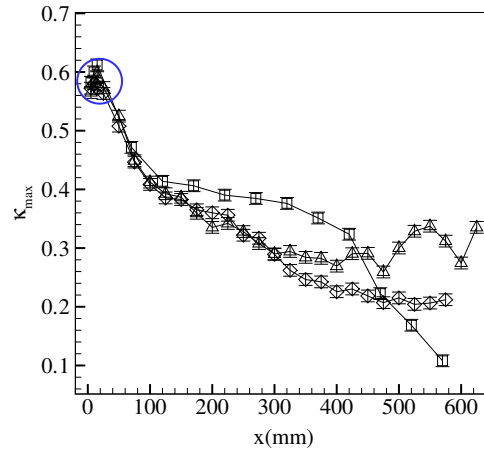


Figure 5.18: Evolution of maximum disturbance amplitude(κ_{max}) corresponding to the middle vortex pair: \square - $\lambda=10$ mm, \triangle - $\lambda=12.5$ mm, \diamond = 15 mm.

The development of κ_{max} in figure 5.18 depicts two regions of disturbance growth. The blue encircled region shows the transient growth regime followed by the region of consistent decay of the disturbance amplitude. In the case of $\lambda=10$ mm, in the region of consistent decay, the maximum amplitude disturbance is greater than that of $\lambda=12.5$ mm and 15 mm. This is because the close proximities of the vortex pair resists the viscous diffusion between the vortex pairs and hence the boundary layer is susceptible to the outer high momentum fluid, thus causing the difference between the upwash and the downwash to be higher than those of $\lambda=12.5$ mm and 15 mm. Downstream of $x=400$ mm, the disturbance amplitude decays rapidly due to the collapse of the vortex pairs due to interaction. Comparing $\lambda=12.5$ mm and 15 mm, the disturbance amplitude curves collapse well till $x=300$ mm. Downstream of $x=300$ mm, the disturbance amplitude increases in the case $\lambda=12.5$ mm as the vortices diffuse leading to the reduction in space between the vortex pair. This close proximities of the vortex pair makes the boundary layer susceptible to the outer high momentum fluid similar to the case of the $\lambda=10$ mm, thus leading to the increased amplitude in the case of $\lambda=12.5$ mm.

5.6 Spectral characteristics

Spectral analysis was carried out to obtain the frequencies of the instability modes. Since the development of the vortex pairs are identical, as evident from the time-averaged streamwise velocity contours (figures 5.1, 5.2 and 5.3), the spectral analysis corresponding to the maximum Tu location was carried for the center vortex pair. The locations were (y, z) co-ordinate that corresponded to the region I of the varicose mode and Tu peak region of the sinuous mode.

Figure 5.19 plots the power spectra of the instability modes of the middle vortex, for all the three cases. Evidently, the spectral characteristics of all the cases are identical. The dominant peak in the transient growth regime (from $x=5$ mm to $x=15$ mm) occurs at 40 Hz in all the three cases. Downstream of the transient regime (between $x=25$ mm and 75 mm), the dominant peak shifts towards higher frequency (150 Hz) thus denoting the well developed varicose mode. At $x=100$ mm, the high frequency peak subsides and the energy encompassed is found to be distributed in the low frequency spectrum. This denotes the decay of the varicose mode and its transition to sinuous mode. Further downstream, as seen in the isolated riblet case (figure 4.19), the energy encompassed in the low frequency continually increases owing to increased spatial oscillation of the streaks. Comparing the power spectra of the forced wavelength disturbances to that of the isolated riblet, hardly any difference could be observed. This leads us to the conclusion that the interaction of the vortices seldom affects the instability unlike in the case of coherent structures where the instability is sensitive to wavelengths (Konishi and Asai, 2004).

5.7 Concluding remarks

Detailed investigation of the development of forced wavelength disturbances initiated by the in-line arrangement of convergent riblets of height $k=1.5$ mm has been carried out using single-sensor hot-wire anemometer measurements for three different wavelengths - $\lambda = 10$ mm, 12.5 mm and 15 mm.

In all the cases, the streamwise vortex pairs exhibit transient growth in the near downstream of the riblet. The close proximities of the vortex pairs in the case of $\lambda=10$ mm shows inconsistency within the context of occurrence of maximum Tu peaks when compared to $\lambda=12.5$ mm and 15 mm. The reason being the balance between the two mutually induced velocities (away and

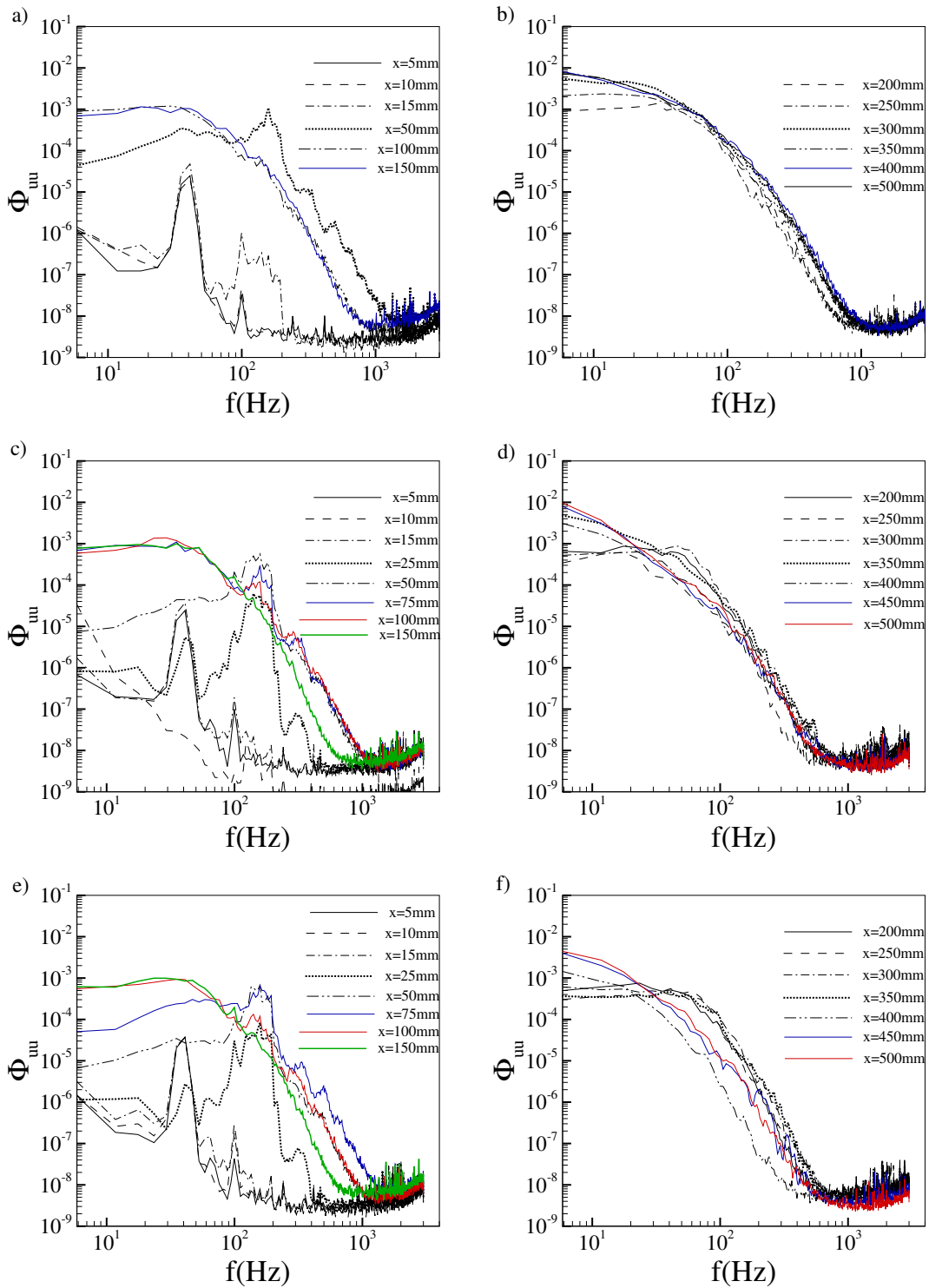


Figure 5.19: Power spectra of streamwise fluctuating velocity component of the middle vortex pair, at several streamwise stations: a) and b) $\lambda=10$ mm, c) and d) $\lambda=12.5$ mm, e) and f) $\lambda=15$ mm.

towards the wall). Furthermore, in the case of $\lambda=10$ mm, the growth of the vortices leads to interaction of the vortex pairs and later breakdown to turbulence. The development of the vortex pairs in the case of $\lambda=12.5$ mm and 15 mm is accompanied by the growth of the intermediate vortices between the vortex pairs.

The concentrations of Tu showcase the growth and decay of the varicose mode followed by the transition to sinuous mode. The difference in wavelength was not found to induce sub-harmonic modes unlike the case of coherent structures in the transitional boundary layer.

The trend of the vortex growth rate was found to be similar to that of an isolated riblet, except that the magnitude of the parameter κ was found to vary due to the presence and absence of intermediate vortices.

On the other hand, it was found that the spectral characteristics of the streamwise vortices were identical for all the three cases and seldom made any difference when compared to those of the isolated riblet. The energy in the most dominant peak ($f=150\text{Hz}$), which corresponded to the varicose mode, was later found to be distributed in the low frequency spectrum along the downstream due to the subsequent manifestation of sinuous modes.

Chapter 6

Conclusions and Recommendations

6.1 Conclusions

The influence of a directionally-dependent surface roughness element, namely convergent riblet, in a flat plate zero-pressure gradient boundary layer has been experimentally studied by means of smoke flow visualization technique and single sensor hot-wire anemometer measurements. Investigation was carried out for two different cases as follows

i) The first case where the Blasius boundary layer was under the influence of an isolated convergent riblet, the initiated disturbances were in interaction with the peninsula of Blasius flow. 6 different sets of experiments concerning 6 different heights of the riblet ($k=1, 1.3, 1.5, 1.8, 2$ and 3 mm) were carried out.

ii) The second case involved the study of instability due to the forced wavelength disturbances wherein the induced vortex pairs were in interaction with their identical ones. The forcing of wavelength was exercised by arranging the riblets of height $k=1.5$ mm in-line with three different spacing -10, 12.5 and 15mm - leading to three different vortex wavelengths(λ).

6.1.1 Isolated Riblet

Resultant flow phenomenon due to the effect of different heights of the riblet $k/\delta_k=0.16, 0.2, 0.24, 0.28, 0.32$ and 0.48 , whose corresponding roughness Reynolds number were $Re_k=47, 83, 96, 150, 184$ and 380 respectively, were analysed.

The smoke flow visualization experiments showed that the initial disturbances were a pair of

streamwise counter-rotating vortices convected by mean flow along the downstream. With the increasing height of the riblet, the tip vortices appeared along the downstream.

Hot-wire measurements exposed the two different characteristics of the upwash velocity velocity profiles - i) For $k/\delta=0.16$ and 0.24 , the inflectional velocity profile was a hyperbolic-tangent of the wall normal co-ordinates and ii) for $k/\delta=0.48$, the upwash velocity profile incurred two inflection points similar to that of the final stage of Gortler instability mechanism.

The development of total disturbance profiles (U'_{rms}) for such manifested initial disturbances showed a narrow region of transient growth in the near downstream of the riblet in the case of $k=1$ mm and $k=1.5$ mm. In addition, the disturbance profiles showed two peaks, a near wall peak and a boundary-layer-edge-peak, along the downstream in the case of $k=1.5$ mm. In the case of $k=3$ mm no transient growth regime was observed. However, the double peaks as in the case of $k=1.5$ mm were observed.

The spanwise wavelength power spectra indicated the shift of the energy peak to higher wavelengths in the transient growth regime as in the case of $k/\delta_k=0.16$, while in the case of $k/\delta_k=0.24$ and $k/\delta_k=0.48$, accommodation of the shorter wavelength peaks in the spectra was observed. This indicated that, with the increasing roughness Reynolds number, the flow phenomena seized to exhibit transient growth.

The streak characteristics justified the departure of the flow phenomena from transient growth. The time-averaged streamwise velocity contours showed that the spanwise inflections subsided in the case of $k/\delta_k=0.16$ due to strong viscous effects. The mutually induced velocity due to the vortex pair in this case wasn't strong enough for the vortices to have them moved out of the boundary layer and hence remained under the influence of viscous dissipation in the boundary layer. For $k/\delta_k=0.24$, meandering of the streaks due to the manifestation of instability modes was observed. With further increasing height of the riblet, the vortex breakdown due to vorticity cancellation and viscous diffusion were observed to be the dominant phenomenon as in the case of $k/\delta_k=0.48$. The effect of tip vortices in the case of $k/\delta_k=0.48$ is reflected by the appearance of two low speed streaks distributed symmetrically to the vortex pair.

The turbulence intensity(Tu) profiles showed that the evolution of the instability incurred 3 stages in the case of $k=1.5$ mm. The first stage involved a steep growth of varicose mode. The

second stage involved the decay of varicose mode and its transition to sinuous mode, while the third stage was the growth of sinuous mode. Subsequently, power spectral analysis in locations pertaining to Tu peaks at different streamwise stations was performed based on Welch method. In the near downstream of the riblet, till $x=50$ mm, the spectra showed that the energy rested in the high frequency ($f=150$ Hz) corresponded to the varicose mode. Further downstream, the decay of the varicose mode and its transition to sinuous was reflected in a way that the energy was distributed in the low frequency spectrum. Above $x=200$ mm, the growth of the sinuous mode was indicated by the increasing energy distribution in the low frequency spectrum. For a streamwise counter-rotating vortex pair that is convected by the mean flow, the spectral characteristics lead to the conclusion that the increase in the low frequency energy spectrum was only due to increased spatial oscillation of the streaks. This was also reflected in the pre-multiplied energy spectra plot wherein the streamwise wavenumber decreased along the downstream.

Putting together the observations, it can be concluded that with respect to increasing roughness Reynolds number, the evolution of the disturbances inadvertently underwent three different phenomena, namely: transient growth, streak instability and vortex breakdown by viscous diffusion. The instability observed in this case is not similar to that exhibited by the hairpin vortices in the transitional boundary layer.

6.1.2 Forced wavelength disturbances

The development of the time-averaged streamwise velocity contours showed three distinct features with respect to three different wavelengths. Firstly, in the case of $\lambda=10$ mm, the growth of the vortex pairs lead to interaction and breakdown of the vortices at $x=400$ mm downstream of the riblet. Secondly, in the case of $\lambda=12.5$ mm, the vortex pairs were accompanied by the intermediate vortices till $x=400$ mm and thereafter the vortex pairs were found to be in close proximities due to its continuous diffusion along the downstream. Finally, in the case of $\lambda=15$ mm, the intermediate vortices were found to accompany the vortex pairs throughout the region of investigation.

The contours of Tu were found to exhibit almost similar trend for all the three wavelengths - the growth of varicose modes, its decay and transition to sinuous mode and finally the growth of sinuous mode. This trend was identical to the isolated riblet case. The balance of the mutually

induced velocities away from and towards the wall only dictated the wall normal position of the peak of T_u .

The shear stress contours were found to be coherent with T_u in a way that the location of the peak of T_u at certain streamwise stations collapsed well with the location of the peak of $\partial u/\partial y$ indicating the varicose mode and for the rest of the areas of investigation the locations of the peak of T_u were in line with those of $\partial u/\partial z$ indicating the manifestation of sinuous modes.

The vortex growth rate measured in terms of maximum streak amplitude κ showed narrow transient growth regime in the near downstream of the riblet, followed by the decay of the streak amplitude. In the case of $\lambda=10$ mm, the steep decay of the streak amplitude was due to the breakdown of the vortex pair. Downstream of $x=300$ mm, the decay was found to be slower in the case of $\lambda=12.5$ mm compared to that of $\lambda=15$ mm, which was due to the close proximity of the vortex pairs in the case of $\lambda=12.5$ mm.

The spectral characteristics, again obtained at the maximum T_u , showed identical behaviour for all the three wavelengths. Also, as identical to the case of isolated riblet, the dominant peak shifted from the high frequency region (150 Hz) to low frequency spectrum indicating all the three stages of development of instability modes.

From these observations, it can be sustained that the effect of wavelength seldom has any effect over instability.

6.2 Recommendations

Further developments based on the present findings can be considered as follows:

1. The success of inducing disturbances in the boundary layer by means of surface roughness has made it possible to control and study the evolution of disturbances, at least within the context of fundamental research. In the present study, a convergent riblet with flow kinematics falling in line with those of wishbone vortex generator and forwards vane vortex generator was put to test within the context of transient growth. Likewise, from the population of vortex generators (Lin, 2002), a certain surface roughness that could be a candidate member of a particular flow kinematics can be considered for a similar study.
2. Considering potential wind tunnel variations in free stream turbulence intensity, which plays a major role in instability, the repeatability of the experiment in different tunnels may be consid-

ered so as to give a clearer picture of the disturbance growth and more importantly of instability modes.

3. The downstream extent to which the measurements has been conducted in the present study comes as an expediency. This did not allow to conclude whether the manifested instability modes drove the boundary layer to turbulence. Conducting the same experiments in a tunnel with higher cross-sectional area might answer the question.

4. The key point in turbulence production mechanism is the manifestation of the Reynolds stresses and their evolution. In this light, numerical or physical experiments concerning the quantification of spanwise velocity component would push the boundaries of the present study.

5. Finally, the most important problem is that the studies concerning any surface roughness is parameter-rich. This calls for an exhaustive research for the generalization of the flow physics for a particular surface roughness that offers specific flow kinematics. The present study dealt with a convergent riblet with isosceles triangle cross section and 30° angle of inclination to the flow. In this light, in order to broaden the scope of the present study, few exploratory studies were undertaken as follows.

1) The effect of angle of inclination of the riblet to the flow: Figure 6.1 shows the initial disturbance due to the riblet of angle 45° and 60° for riblet height $k/\delta_k=0.48$. It can be clearly seen that

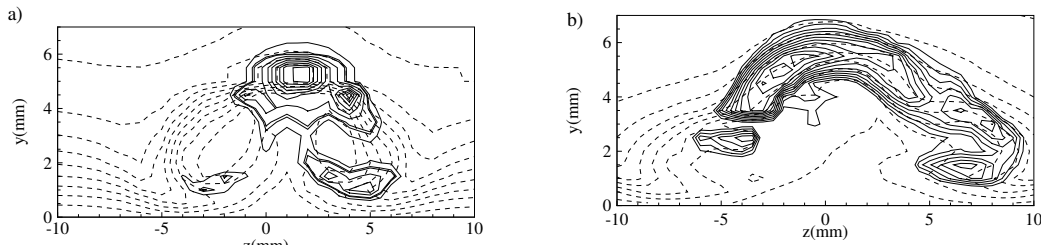


Figure 6.1: Characteristics of initial disturbances for riblet height $k/\delta_k=0.48$; a) riblet aligned at an angle of 45° to the flow and b) riblet aligned at an angle of 60° to the flow. Solid lines- Isolines of Tu ; Dashed lines - Isolines of normalized streamwise component of velocity (u/U_∞).

with the increasing angle of inclination to the flow, the contours are flatter and the concentrations of the turbulence intensity are quite different when compared to figure 4.5 in chapter 4. This is one possibility of looking deeper into the problem.

2) The variation of geometry: The present study was focussed on riblet with isosceles triangle cross-sectional area. Exploratory study on a rectangular cross-sectional riblet was undertaken in

order to take a sneak peak into how the variation of geometry can affect the flow kinematics. Figure 6.2 shows an isolated rectangular convergent riblet. The base b is taken to be equal to that of that of the base of the isosceles triangle.

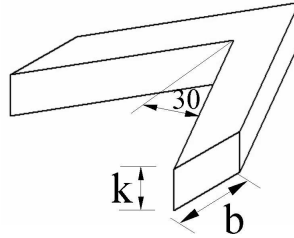


Figure 6.2: An isolated Convergent riblet with rectangular cross-section; k - height, b - base width

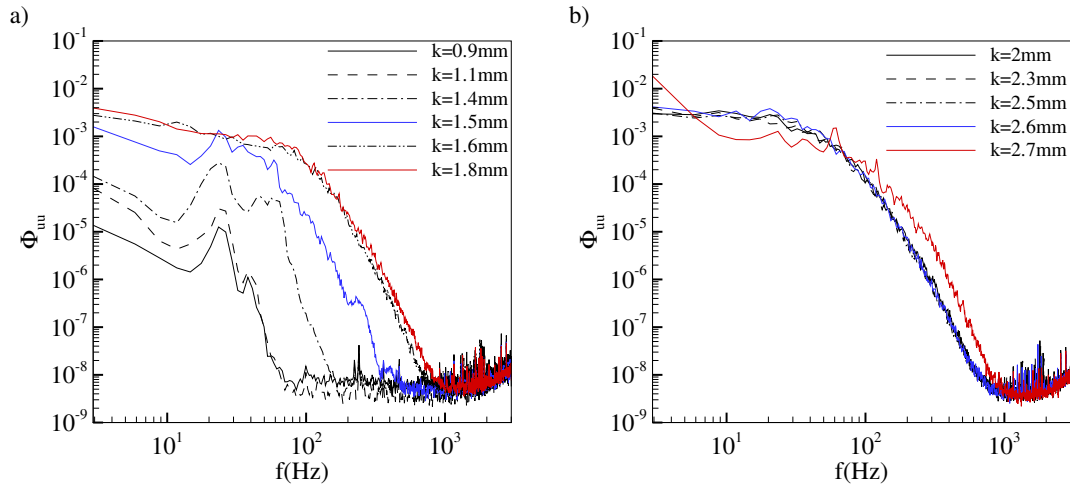


Figure 6.3: Power spectra of the streamwise fluctuating velocity with respect to different riblet heights.

Figure 6.3 plots the power spectral density of maximum Tu at station $x=200$ mm from the trailing edge of the riblet. The station is chosen in such a way that the spectra falls in the region that either corresponds to transition from varicose to sinuous mode or corresponds to the region of fully developed sinuous mode or corresponds to the region the vortices have already broken down. Between the roughness heights of $k=0.9$ mm and 1.5 mm, the most dominant peak is observed at 20 Hz. Between $k=1.6$ and 2.6 mm, the energy distributed in the low frequency spectrum increases showcasing the manifestation of sinuous modes. For height $k=2.7$ mm, two peaks corresponding to 60 Hz and 120 Hz starts appearing as harmonics denoting the breakdown

of the vortices. On comparing the power spectra of the rectangular convergent riblet at $k=1.5$ mm with that of the triangular riblet (figure 4.19), it can be seen that the curves are identical. Though the spectra are identical, experiments can be conducted for other cross-sectional shapes of riblet to generalize of the effect of convergent riblet on transient growth and streak instability.

Bibliography

- Acarlar, M. and Smith, C. (1987). A study of hairpin vortices in a laminar boundary layer. part 1. hairpin vortices generated by a hemisphere protuberance. *Journal of Fluid Mechanics*, 175:1–41.
- Andersson, P., Berggren, M., and Henningson, D. (1999). Optimal disturbances and bypass transition in boundary layers. *Physics of Fluids*, 11:134–150.
- Andersson, P., Brandt, L., Bottaro, A., and Henningson, D. (2001). On the breakdown of boundary layer streaks. *Journal of Fluid Mechanics*, 428:29–60.
- Asai, M., Minagawa, M., and Nishioka, M. (2002). The instability and breakdown of a near-wall low speed streak. *Journal of Fluid Mechanics*, 455:289–314.
- Bakchinov, A., Grek, G., Klingmann, B., and Kozlov, V. (1995). Transition experiments in a boundary layer with embedded streamwise vortices. *Physics of Fluids*, 7(4):820–832.
- Bernard, P. (2012). Vortex dynamics in transitional and turbulent boundary layer. In *50th AIAA Aerospace Sciences Meeting including the New Horizon forum and Aerospace Expedition*, Nashville, Tennessee.
- Boiko, A., Dovgal, A., and Sorokin, A. (2012). Instability of a backward-facing step flow modified by stationary streaky structures. *Physics of Fluids*, 24:104104–1–104104–11.
- Bottaro, A. and Klingmann, B. (2002). On the linear breakdown of gortler vortices. *European Journal of Mechanics B/Fluids*, 15:301–330.
- Brandt, L. (2007). Numerical studies of the instability and breakdown of a boundary-layer low-speed streak. *European Journal of Mechanics B/Fluids*, 26:64–82.

- Brandt, L., Cossu, C., Chomaz, J., Huerre, P., and Henningson, D. (2003). On the convectively unstable nature of optimal streaks in boundary layers. *Journal of Fluid Mechanics*, 485:221–242.
- Brandt, L. and Henningson, D. (2002). Transition of streamwise streaks in zero-pressure-gradient boundary layer. *Journal of Fluid Mechanics*, 472:229–261.
- Butler, K. and Farrell, B. (1992). Three dimensional optimal perturbations in viscous shear flow. *Physics of Fluids*, 4:1637–1650.
- Chernoray, V., Kozlov, V., Lofdahl, L., and Chun, H. (2006). Visualization of sinusoidal and varicose instabilities of streaks in a boundary layer. *Journal of visualization*, 9(4):437–444.
- Cherubini, S., Tullio, M., Palma, P., and Pascazio, G. (2013). Transient growth in the flow past a three-dimensional smooth roughness element. *Journal of Fluid Mechanics*, 724:642–670.
- Cimbala, J., Nagib, H., and Reshotko, A. (1988). Large structure in the far wakes of two dimensional bluff bodies. *Journal of Fluid Mechanics*, 190:265–298.
- Coleman, H. and Steele, W. (1998). *Experimentation and Uncertainty Analysis for Engineers*. Wiley, USA.
- Cossu, C. and Brandt, L. (2002). Stabilization of tollmien-schlichting waves by finite amplitude optimal streaks in the blasius boundary layer. *Physics of Fluids*, 14:L57–L60.
- Denissen, N. and White, E. (2013). Secondary instability of roughness-induced transient growth. *Physics of Fluids*, 25:114108–1–114108–18.
- Denissen, N. A. and White, E. B. (2009). Continuous spectrum analysis of roughness-induced transient growth. *Physics of Fluids*, 21:114105–1–114108–13.
- Doligalski, T., Smith, C., and Walker, J. (1994). Vortex interactions with walls. *Annual Review of Fluid Mechanics*, 26:573–616.
- DownsIII, R., White, E., and Denissen, N. (2008). Transient growth and transition induced by random distributed roughness. *AIAA journal*, 46(2):451–462.

- Ellingsen, T. and Palm, E. (1975). Stability of linear flow. *Physics of fluids*, 18:487–488.
- Ergin, F. and White, E. (2005). Multicomponent and unsteady velocity measurements of transient disturbances. In *43rd AIAA Aerospace Sciences Meeting and Exhibit*, Reno, Nevada.
- Ergin, F. and White, E. (2006). Unsteady and transitional flows behind roughness elements. *AIAA*, 44(11):2504–2514.
- Farrell, B. and Ioannou, P. (1993). Optimal excitation of three dimensional perturbations in viscous constant shear flow. *Physics of Fluids*, 5:1390–1400.
- Fischer, P. and Choudhari, M. (2004). Numerical simulation of roughness-induced transient growth in a laminar boundary layer. *AIAA Paper 2004-2539*.
- Fransson, J., Brandt, L., Talamelli, A., and Cossu, C. (2004). Experimental and theoretical investigation of the no-modal growth of steady streaks in a flat plate boundary layer. *Physics of Fluids*, 16(10):3627–3638.
- Hamilton, J. and Abernathy, F. H. (1991). Streamwise vortices and transition to turbulence. *Journal of Fluid Mechanics*, 264:185–212.
- Henningson, D., Lundbladh, A., and Johansson, A. (1993). A mechanism for bypass transition from localized disturbances in wall-bounded shear flows. *Journal of Fluid Mechanics*, 250:169–207.
- Herbert, T. (1988). Secondary instability of boundary layers. *Annual review of Fluid Mechanics*, 20:487–526.
- Hultgren, L. and Gustavsson, L. (1981). Algebraic growth of disturbances in a laminar boundary layer. *Physics of Fluids*, 24:1000–1004.
- Hutchins, N. and Marusic, I. (2007). Evidence of very long meandering features in the logarithmic region of turbulent boundary layers. *Journal of Fluid Mechanics*, 579:1–28.
- Kendall, J. (1981). Laminar boundary layer velocity distortion by surface roughness: Effect upon stability. *AIAA paper 81-0195*.

- Klebanoff, P., Tidstrom, K., and Sargent, L. (1961). The three-dimensional nature of boundary-layer instability. *Journal of Fluid Mechanics*, 12:1–34.
- Konishi, Y. and Asai, M. (2004). Experimental investigation of the instability of spanwise-periodic low-speed streaks. *Fluid Dynamics Research*, 34:299–315.
- Landahl, M. (1980). A note on an algebraic instability of inviscid parallel shear flows. *Journal of Fluid Mechanics*, 98(2):243–251.
- Lin, J. (2002). Review o research on low-profile vortex generators to control boundary-layer separation. *Progress in Aerospace Sciences*, 38:389–420.
- Luchini, P. (2000). Reynolds-number-independent instability of the boundary layer over a flat surface: optimal perturbations. *Journal of Fluid Mechanics*, 404:289–309.
- Matsubara, M. and Alfredsson, P. (2001). Disturbance growth in boundary layers subjected to free-stream turbulence. *Journal of Fluid Mechanics*, 430:149–168.
- Miklavcic, M. and Williams, M. (1982). Stability of mean flows over an infinite flat plate. *Archive for Rational Mechanics and Analysis*, 80:57–69.
- Mitsudharmadi, H., Winoto, A., and Shah, D. (2004). Development of boundary-layer flow in the presence of forced wavelength gortler vortices. *Physics of Fluids*, 16:3983–3996.
- Morkovin, M., Reshotko, E., and Herbert, T. (1994). Transition in open flow systems - a re-assessment. *Bull. APS*, 39(9):1882.
- Pattenden, R., Turnock, S., and Zhang, X. (2005). Measurements of the flow over a low-aspect ratio cylinder mounted on a ground plate. *Experiments in Fluids*, 39:10–21.
- Reddy, S. and Henningson, D. (1993). Energy growth in viscous channel flows. *Journal of Fluid Mechanics*, 252:209–238.
- Rice, J. (2004). Roughness receptivity and scaling of non-optimal disturbances. Master's thesis, Case Western Reserve University.

- Schlatter, P., Brandt, L., De Lange, H., and Henningson, D. (2008). On streak breakdown in bypass transition. *Physics of Fluids*, 20:101505–1–101505–15.
- Schmid, P. and Henningson, D. (2001). *Stability and Transition in Shear Flows*. Springer, New York.
- Schoppa, W. and Hussain, F. (2002). Coherent structure generation in near-wall turbulence. *Journal of Fluid Mechanics*, 453:57–108.
- Smits, A. and Lim, T. (2000). *Flow visualization: techniques and examples*. Imperial college press, UK.
- Swearingen, J. and Blackwelder, R. (1987). The growth and breakdown of streamwise vortices in the presence of a wall. *Journal of Fluid Mechanics*, 182:255–280.
- Tandiono, Winoto, S., and Shah, D. (2009). Wall shear stress in gortler vortexboundary layer flow. *Physics of Fluids*, 21:084106(1–9).
- Tandiono, T., Winoto, S., and Shah, D. (2013). Spanwise velocity component in nonlinear region of gortler vortices. *Physics of Fluids*, 25:104104–1–104104–14.
- Tumin, A. (2003). Multimode decomposition of spatially growing perturbations in a two-dimensional boundary layer. *Physics of Fluids*, 15:2525–2540.
- Tumin, A. and Reshotko, E. (2001). Spatial theory of optimal disturbances in boundary layers. *Physics of Fluids*, 13(7):2097–2104.
- Westin, K., Boiko, A., Klingmann, B., Kozlov, V., and Alfredsson, P. (1994). Experiments in a boundary layer subjected to free stream turbulence. part 1. boundary layer structure and receptivity. *Journal of Fluid Mechanics*, 281:193–218.
- White, E. (2002). Transient growth of stationary disturbances in a flat plate boundary layer. *Physics of Fluids*, 14:4429–4439.
- White, E. and Ergin, F. (2003a). Receptivity and transient growth of roughness-induced disturbances. *AIAA paper 2003-4243*.

- White, E. and Ergin, F. (2003b). Using laminar-flow velocity profiles to locate the wall behind roughness elements. *Experiments in Fluids*, 36:805–812.
- White, E. and Reshotko, P. (2002). Roughness-induced transient growth in a flat-plate boundary layer. *AIAA paper 2002-0138*.
- White, E., Rice, J., and Ergin, F. (2005). Receptivity of stationary transient disturbances to surface roughness. *Physics of Fluids*, 17(5):0064109–1–064109–12.
- Winoto, S. and Crane, R. (1980). Vortex structure in laminar boundary layers on a concave wall. *International Journal of Heat and Fluid Flow*, 2:221–231.
- Zuccher, S., Bottaro, A., and Luchini, P. (2006). Algebraic growth in a blasius boundary layer: Nonlinear optimal disturbances. *European Journal of Mechanics B/Fluids*, 25:1–17.

Publications

Parts of the present work and few other related works were or to be published in following journals and conference proceedings.

- 1.) T. Nadesan, D. Estruch-Samper, T.S. Lee, H.T. Low, "Influence of convergent riblet in Blasius boundary layer," (Manuscript to be submitted to Physics of Fluids)
- 2.) T. Nadesan, D. Estruch-Samper, T.S. Lee, H.T. Low, "Instability due to forced wavelength disturbances induced by convergent riblet, " (Manuscript in preparation)
- 3.) T. Nadesan, H. Mitsudharmadi, T.S. Lee, S.H. Winoto, "Disturbance initiated by Convergent riblet in flat plate boundary layer," 19th Australasian Fluid Mechanics conference, Melbourne, Australia, December 2014.
- 4.) T. Nadesan, H. Mitsudharmadi, T.S. Lee, S.H. Winoto, "Quasi-streamwise vortices initiated by multiple convergent riblets in a flat plate boundary layer," Journal of Visualization 17(4), 31-325, 2014.
- 5.) T. Nadesan, H. Mitsudharmadi, T.S. Lee, S.H. Winoto, "Effects of converging riblets in flat plate boundary layer," The 12th International Symposium on Fluid Control, Measurement and Visualization, Nara, Japan, November 2013.